

# Exploring Multi-functionality in Spin Crossover Complexes: A Special Emphasis on Synergistic Luminescence and Dielectric Properties

*Bijoy Dey,<sup>†</sup> Debopam Sarkar,<sup>†</sup> Sounak Ghosh,<sup>†</sup> Sakshi Mehta,<sup>†</sup> Krishna Kaushik,<sup>†</sup> Subrata Ghosh<sup>\*†</sup> and Abhishake Mondal<sup>\*†</sup>*

<sup>†</sup>*Solid State and Structural Chemistry Unit, Indian Institute of Science, Sir C V Raman Road, Bangalore 560012, India.*

Corresponding Authors:

Email Addresses: subratat@iisc.ac.in (Subrata Ghosh), mondal@iisc.ac.in (Abhishake Mondal)

## ABSTRACT

Molecules exhibiting multifunctional properties, such as magnetic bistability, luminescence, and dielectric properties have excellent potential for application in magnetic optoelectronic devices. Research into luminescent magnets and switching materials is continuously expanding because, in these cases, spin-state change can be expressed by the fluorescence signal, and this can provide materials with practical application prospects. This review presents the recent progress in multi-functional spin crossover (SCO) systems, particularly emphasizing the need for synergistic luminescence or dielectric response of SCO systems. The present work highlights syntheses, design strategies, crystal structures, magnetic, luminescence, and dielectric response to obtain materials with potential applications in switches, sensors, and other practical domains.

**KEYWORDS:** Multifunctional Spin Crossover Materials, Fluorescence, Dielectric Property, Photomagnetism, Thermosensing.

## Abbreviations:

SCO = Spin Crossover, AIE = Aggregation Induced Emission, CD = Circular Dichroism, VCD = Vibrational Circular Dichroism, McHD = Magneto-chiral Dichroism, LIESST = Light-Induced Excited Spin State Trapping, PCU = Primitive Cubic Unit, DFT = Density Functional Theory, LIR = Luminescence Intensity Ratio, PL = Photoluminescence.

## 1. INTRODUCTION

Over the last few years, multifunctional materials have gained significant attention in a broad area of scientific research, including chemistry, physics, and material sciences, as these materials can importantly be used in a single device due to the presence of two or more physical properties [1]. In this aspect, multifunctional magnetic materials have shown tremendous potential to realize their application in modern-day technologies [2-7]. Magnetic, optical and electrical bistability expressed by spin crossover (SCO) [8-10], single-chain magnets (SCMs) [11-13], single-molecule magnets (SMMs) [14-19], and metal-to-metal electron transfer (MMET) [20-22] systems have received a lot of interest due to their potential application in molecular electronics and spintronics as the bistability of these systems can be controlled and tuned by several external stimuli, *e.g.*, light, electric field, temperature, pressure *etc.* [9,10].

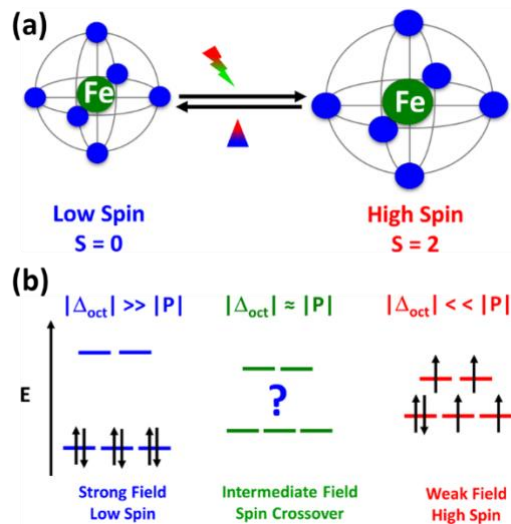


**Fig. 1.** Schematic representation of SCO in an octahedral iron(II) coordination sphere under the application of temperature and light (a) with the d orbital splitting diagram (b).

Materials exhibiting SCO property fall under an important class of molecular bistability that arises from the spin-state switching between two electronic states, so-called low spin (LS) and high spin (HS), under the application of various external stimuli, *e.g.*, pressure, temperature, light

irradiation, magnetic field, presence or absence of guest molecule (Fig. 1a) [8-10,23,24]. Generally, a  $3d$  transition metal center with  $3d^4$ - $3d^7$  electronic configuration in a (distorted) octahedral geometry shows such bistability in a detectable way, where depending on the ligand field strength ( $\Delta$ ) and spin pairing energy ( $P$ ), electrons will occupy different  $t_{2g}$  and  $e_g$  orbitals (Fig. 1b). A comparable magnitude of  $\Delta$  and  $P$ , *i.e.*,  $|\Delta| \approx |P|$  brings the opportunity to switch the spin-state between LS and HS upon applying the external stimuli, which is termed as SCO. SCO is associated with significant changes in structure, *e.g.*, metal-ligand bond distances, unit cell parameters, electronic, optical, and magnetic properties [6, 25-28]. Consequently, a large number of physical methods and techniques, *e.g.*, single-crystal, powder X-ray diffraction analyses, magnetic measurements using modern SQUID magnetometer and PPMS susceptometer, heat-capacity measurements, spectroscopic studies (UV-Vis-NIR, IR, Raman, NMR, Mössbauer, fluorescence, *etc.*), have been employed to fully characterize the SCO systems. Temperature-induced SCO has been represented as the most studied one, where entropy-driven HS state and enthalpy-driven LS state are favored at high and low temperatures respectively following the thermodynamic relationship  $\Delta G = \Delta H - T\Delta S$ . Depending on the presence of various long- and short-range interactions, called cooperativity in SCO material, significantly influences thermo-induced SCO, the nature of SCO has been noticed to be gradual, abrupt, with hysteresis, stepwise, and incomplete as shown in Fig. 2 [23]. Despite the major improvements in SCO systems over the last few decades, iron(II)-based SCO materials have been most extensively studied [29-33] among other  $3d$  metals [34-43] where spin-state switching occurs between the LS ( $t_{2g}^6 e_g^0$ ,  $S = 0$ ,  ${}^1A_1$ ) and the HS ( $t_{2g}^4 e_g^2$ ,  $S = 2$ ,  ${}^5T_2$ ) states. Several excellent works exist on SCO systems in various dimensions (0D – 3D), nanomaterials, hybrids, *etc.* [44-45]. Apart from thermo-induced SCO, spin-state switching between LS state to HS meta stable photo-induced state under light irradiation

at low temperature identified as light-induced excited spin state trapping (LIESST) effect has been well studied particularly in iron(II) and iron(III) systems. The photo-induced HS state relaxes back to the LS ground state at a particular temperature known as  $T_{LIESST}$  after heating the sample in the dark [46]. Many excellent works on the LIESST effect have been reported to which we refer the reader [47-48].

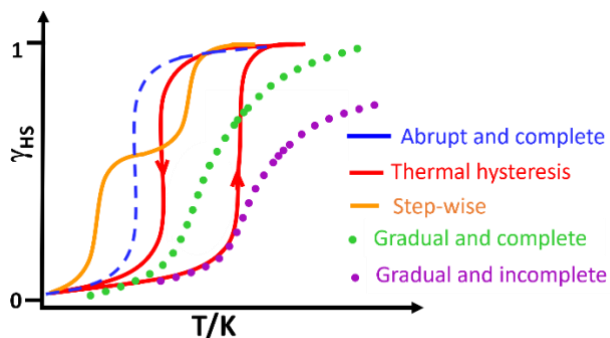


**Fig. 2.** Schematic representations of the different types of SCO events, where the x-axis is the temperature (T) and the y-axis is the fraction of HS ( $\gamma$ ).

Incorporation of one or more physical properties, such as optical, dielectric, and luminescence, with the SCO allows the production of stimuli-responsive multifunctional materials where external perturbation can tune and control both the SCO and associated physical properties in a synergic way [49-52]. Towards multifunctional SCO materials, the simultaneous incorporation of SCO with dielectric and luminescence has been gaining great attention due to their potential application towards the realization of magneto-optical switches or a new regeneration of magneto-electrical devices [49,53,54]. Reading the significant modification of the luminescence signal from luminescent-SCO material during the SCO phenomenon, one can easily signify the spin state switching process and LS/HS state population. Although such a synergic correlation between SCO and luminescence was first described two decades ago [53], it has recently received great attention in material research.

Two major synthetic approaches have been applied so far to integrate SCO and luminescence, where the synergic correlation between these two properties is studied as follows:

1. Extrinsic luminescence approach where a luminophore has been non-covalently grafted or physically doped as a guest within an SCO active materials
2. Intrinsic luminescence approach where a luminescent active ligand is coordinated with SCO center

The latter approach has been recommended as an excellent, however challenging way because direct connectivity between the SCO center and luminescent-active ligand allows to control and tune both properties through a structural-property relationship; on the other hand, finding luminescent ligand with appropriate ligand field strength around SCO metal center is more difficult. The resultant complex often becomes luminescence inactive after coordination between the metal center and luminescent-active ligand [55].

In principle, the synergic correlation mechanism involves a donor-acceptor energy transfer (ET) process where the luminophore and the SCO metal center act as donor and acceptor, respectively [53]. The superposition of the luminophore emission and SCO metal center-based absorption (coming from metal-to-ligand charge transfer and d-d electronic transitions) significantly affect the luminescence signal of the luminophore during spin-state switching. The HS state of the SCO complex features very weak absorption in the near-IR (NIR) region, so the spectral overlap with the donor moiety is less. As a result, the luminescence of the donor doesn't quench (Fig. 3). The LS state of the SCO complex has a high absorption coefficient in the visible region and has more spectral overlap with the ligand than the HS state. Thus, in this case, energy transfer from the donor to the metal center is much facile leading to quenching of the luminescence intensity of the donor moiety [56].

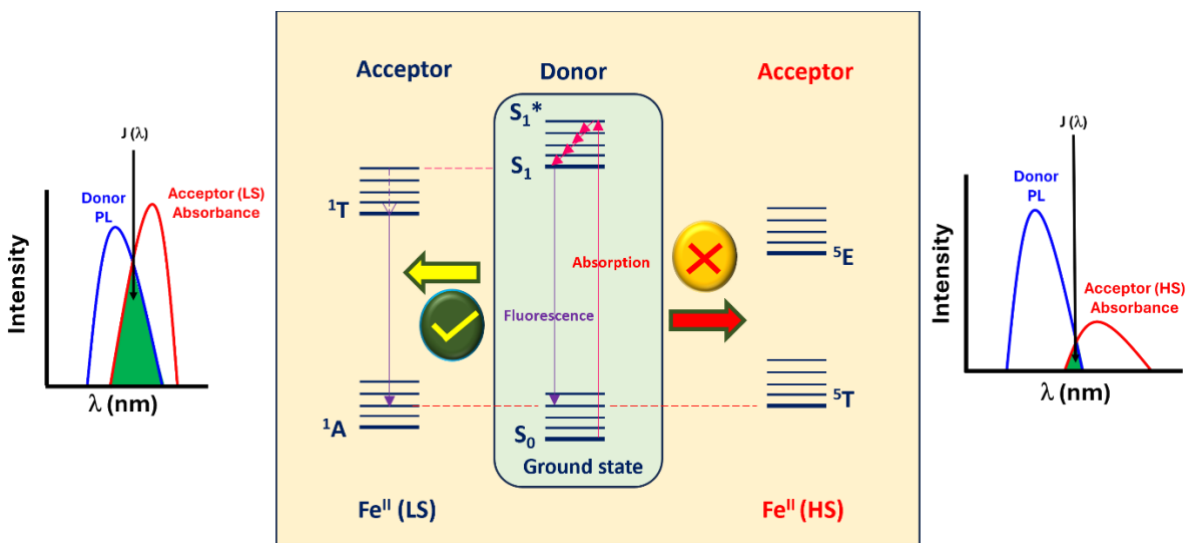
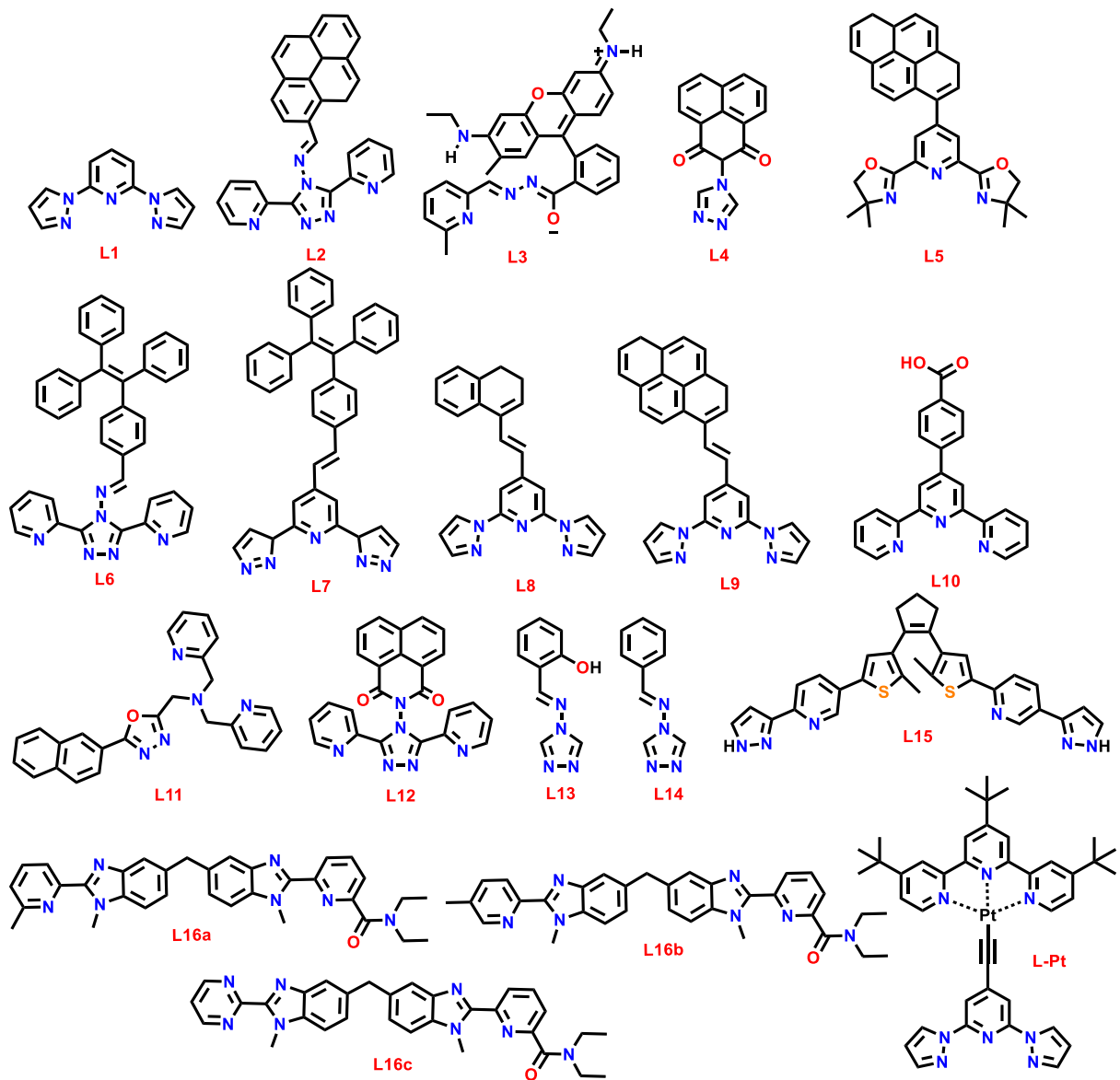
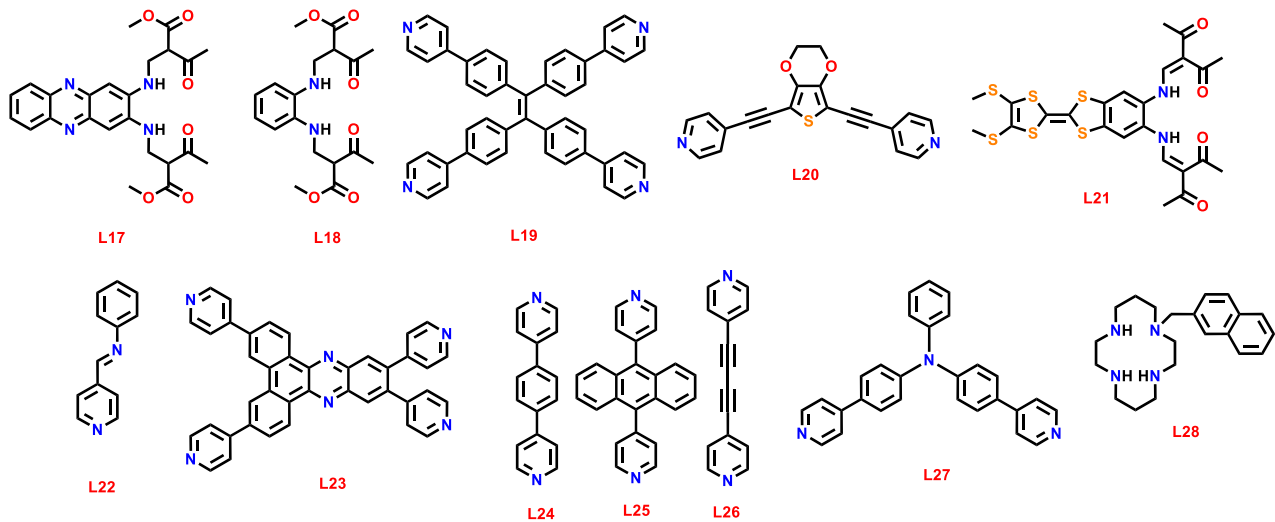


**Fig. 3.** Schematic presentation of synergic coupling of SCO and luminescence. Energy transfer from the excited state of the donor to the HS-SCO complex doesn't occur due to poor spectral overlap and thus the luminescence of the donor is retained (right). For LS-SCO complex spectral overlap is more leading to quenching of luminescence of the donor (left).



**Scheme 1.** Schematic representation of the capping ligands mentioned in this review for the synthesis of 0D SCO-luminescence complexes.



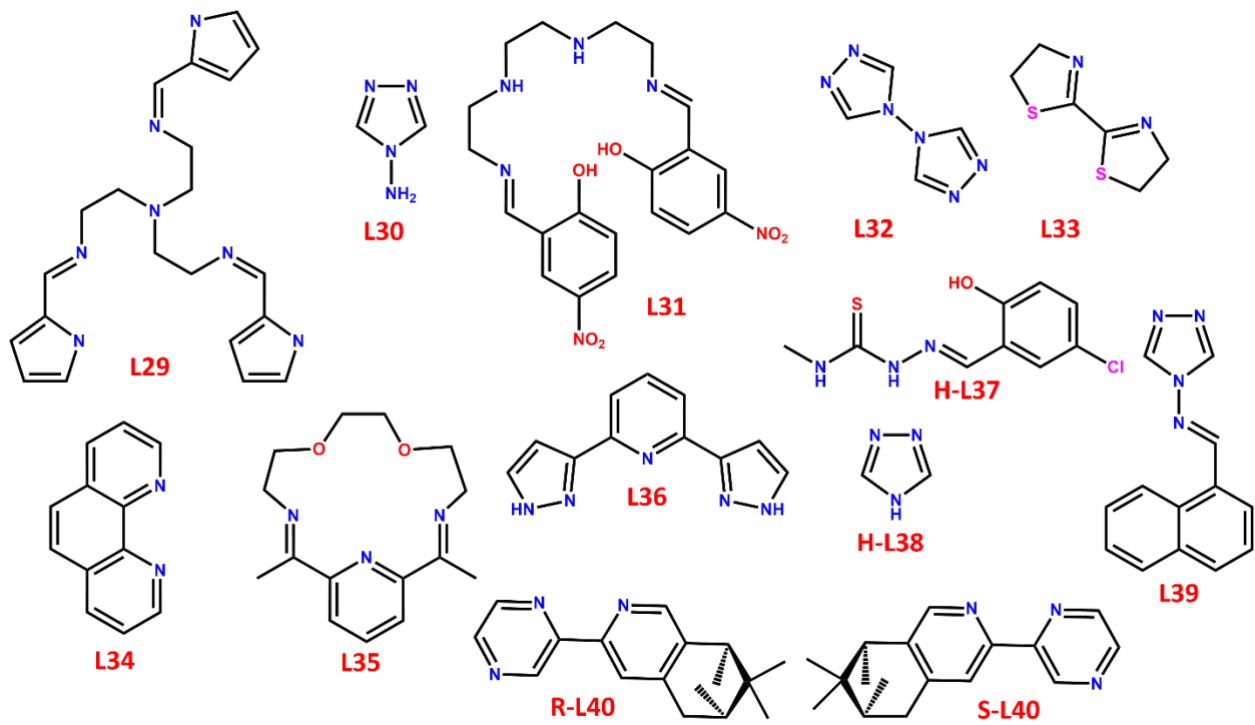
**Scheme 2.** Schematic representation of the bridging ligands mentioned in this review for the synthesis of 1D – 3D SCO-luminescence complexes.

Another exciting physical property associated with spin-state switching is the dielectric property which is the ability of an insulator to store electricity as no free electrons are available to conduct electricity. Although SCO molecules have a paramagnetic metal center, they are surrounded by diamagnetic organic ligands. Thus, overall, molecules are not conducting in nature and behave as insulators. When SCO occurs, the electrons transition from a  $t_{2g}$  set of orbitals to  $e_g$  set of orbitals, and as a result, the bond length increases. During SCO of Fe(II) complexes, Fe-N metal-ligand bond length variation of 5-10% (0.1-0.2 Å) and N-Fe-N angle variation of 0.5-8° are observed [9,23]. This change in bond length and angles leads to a deformation of the local environment around the metal center, and therefore, local electrical dipoles are different in HS and LS states [57]. This change in dielectric property with the spin state of the molecule has been studied with many SCO molecules. As the HS state of the SCO complex is larger in size and has more diffused electron density as compared to the LS state, electronic polarizability should be higher in the HS state than the LS state [57]. Such phenomena were observed in most of the cases, but in some cases

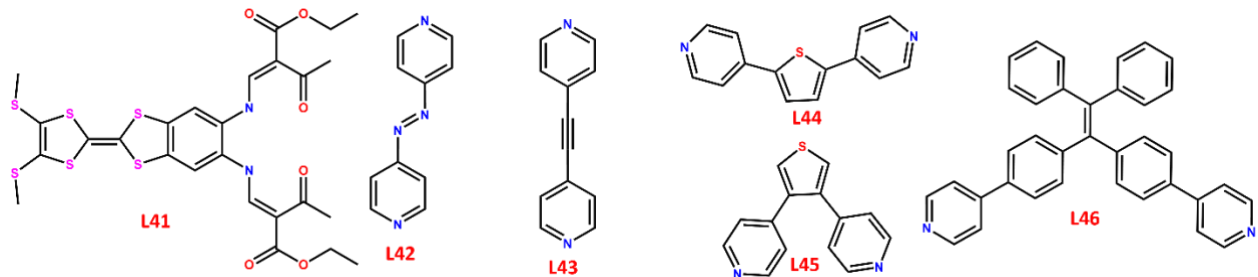
reverse phenomena have also been recorded. All these exciting phenomena will be discussed in the review [52]. The main strategy followed by various research groups for introducing and improving the dielectric property in SCO molecules has been to introduce polar and chiral groups that can have different orientations in different spin states, and thus, it will be reflected in their dielectric properties as well [58]. The complex dielectric permittivity is expressed as  $\epsilon^* = \epsilon' - i\epsilon''$  and is measured in the 10<sup>2</sup>-10<sup>6</sup> Hz frequency range. The real part,  $\epsilon'$  represents the effect of a time-dependent electric field on the displacement of the bounded charges, and dielectric losses are represented by the imaginary part,  $\epsilon''$  [54]. The first reports of synergy between SCO and dielectric properties were published on mononuclear Mn(III) and Fe(II) complexes, and some of them also exhibit thermal hysteresis in both SCO and dielectric profiles with respect to temperature [52, 59]. Later in 2022, cyanide-based 2D and 3D frameworks were also investigated, and they showed much more improved changes in the dielectric profile between the LS and HS states [54]. This is due to the framework structure, all the metal centers are connected, thus, any change affects the whole lattice strongly. Coupling dielectricity with SCO can lead to new bistable systems having multifunctional behavior and can be widely used in designing molecule-based devices. Specially the simultaneous switching of low spin/low-permittivity and high spin/high-permittivity can be of high interest in making sensors, and memory devices as they can be manipulated by various external stimuli [60]. The ligands used for making systems that show both dielectric and SCO behavior are given in schemes 3 and 4.

As a major aim of this review, we will discuss the recent development of (a) SCO-luminescent materials and (b) SCO and dielectric materials having dimensional structure 0D to 3D through syntheses, strategies, crystal structure analyses, magnetic, luminescence, and dielectric properties

with a significant focus on the synergic correlation between SCO with luminescence and dielectric properties.



**Scheme 3.** Schematic representation of the ligands discussed in this review for 0D molecules having both SCO and dielectric behavior.



**Scheme 4.** Schematic representation of the ligands discussed in this review for 1D-3D molecules exhibiting both SCO and dielectric behavior.

## 2. LUMINESCENT SPIN CROSSOVER

### 2.1. Luminescent SCO in 0D molecules

#### Mononuclear:

The synergy between luminescence and SCO has been investigated for less than a decade. In 2017, Guo and co-workers described synergic behavior between Luminescence and SCO in a mononuclear iron(II) complex  $[\text{Fe}(\text{L1})_2](\text{BF}_4)_2$  (**1**) (**L1** = 2,6-bis(pyrazol-1-yl)pyridine; **Scheme 1**) [61], although the structural as well as magnetic properties of **1** were previously reported by Halcrow and co-workers (Fig. 4a) [62]. Yellow crystal of **1** can be obtained from complexation of  $\text{Fe}(\text{BF}_4)_2 \cdot 6\text{H}_2\text{O}$  with ligand **L1** in 1:2 ratio in acetone and successive slow diffusion of diethyl ether into the acetonitrile or nitromethane solution of the complex **1**. Temperature-dependent single-crystal structure analyses were performed at different temperatures such as 290 and 240 K, which showed that upon lowering the temperature, the average Fe–N bond distance decreases by around 0.215 Å, suggesting the conversion between the HS to LS states in the Fe(II) complex. Differential scanning calorimetry (DSC) confirmed the appearance of endothermic/exothermic peaks at 258/262 K showing a 4 K wide hysteresis, demonstrating the occurrence of a SCO assisted first-order phase transition. While no change in the space group ( $P2_1$ ) during crystallographic studies was observed, suggesting a cooperative effect in the hysteretic SCO of **1**. Temperature-dependent magnetic susceptibility measurements were performed to explore the magnetic properties of **1**. A reversible spin-transition between the HS ( $S = 2$ ,  $\chi T = 3.6\text{--}3.7 \text{ cm}^3 \text{ mol}^{-1} \text{ K}$ ) and LS ( $S = 0$ ,  $\chi T \leq 0.3 \text{ cm}^3 \text{ mol}^{-1} \text{ K}$ ) states were observed with  $T_{1/2} = 259 \text{ K}$  with 3 K wide hysteresis loop (Fig. 4b).

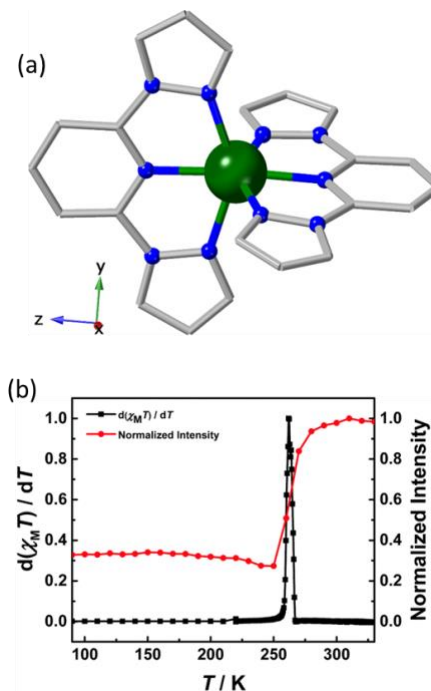


**Fig. 4.** (a) Simplified crystal structure of complex cation in  $[\text{Fe}(\text{L1})_2](\text{BF}_4)_2$  (**1**) at 290 K omitting hydrogen atoms and counteranions for clarity (Fe: green, C: gray, N: blue). (b) Normalized intensity of luminescence at 493 nm and  $d(\chi_T)/dT$  plot of **1** from 90 to 330 K. Adapted with permission from Ref. [61] and [62].

To explore the correlation between luminescence and SCO properties in **1**, the PL measurements were performed between 90 K and 330 K in the solid state for both the **L1** ligand and complex **1**. The PL spectra at room temperature show a narrow emission band centering around 359 nm and a broad structured band between 450 and 565 nm with several maxima for **L1** ligand and **1**, respectively, confirming significantly different PL behavior of both species. Variable temperature PL studies of **1** revealed a weak and stable luminescence of **1** at low-temperature region (90 – 250 K) during increasing temperature, while a sharp increase in the PL intensity ( $I_{493}$  = luminescence intensity of the maximum emission at 493 nm) was observed in the region of 250 to 280 K which remain almost constant upon increasing the temperature further up to 330 K. The abrupt luminescence enhancement at around SCO temperature  $T_{1/2} = 262$  K suggested a synergistic

correlation between the luminescence and SCO properties in **1**. Moreover, a detailed theoretical calculation suggested an LS–HS spin-state switching regulated metal-to-ligand charge transfer (MLCT) based luminescence in **1**. In principle, the luminescence of **1** happened to be too weak to be suitable for practical applications.

Later, in 2018, Liu and co-workers reported the synergic correlation between luminescence and SCO in another iron(II) mononuclear complex [63]. A luminescence active ligand **L2** ((pyrene-1-yl)-N-(3,5-di(pyridin-2-yl)-4H-1,2,4-triazol-4-yl)methanimine; **Scheme 1**) incorporated with highly luminescent motif pyrene was used to prepare mononuclear iron(II) complex  $[\text{Fe}(\mathbf{L2})_2(\text{NCS})_2]$  (**2**) as green crystals from the reaction of  $\text{Fe}(\text{NCS})_2$  with **L2** in DMF. Single crystal X-ray diffraction analyses at temperatures 90 and 277 K revealed that the distorted octahedral surrounding of  $\text{FeN}_6$  was fulfilled by two bidentate **L** ligands and two  $\text{NCS}^-$  ligands in *trans* position (Fig. 5a). The Fe–N bond distances ( $\text{Fe}-\text{N}_{\text{pyridyl}}$ ,  $\text{Fe}-\text{N}_{\text{triazole}}$ , and  $\text{Fe}-\text{N}_{\text{NCS}}$ ) lie in the range of  $2.197(2) - 2.077(3)$  Å at 277 K, while upon lowering the temperature down to 90 K, the bond distances reduce to  $2.014(2) - 1.932(2)$  Å. These Fe–N bond distances at 277 K and 90 K lie in the range expected for the HS and LS state of the Fe(II) center, respectively, suggesting a thermo-induced HS to LS SCO in **2**.

Heat capacity measurements of **2** displayed a first-order phase transition associated with a  $T_{1/2}$  temperature of 265 K associated with HS to LS conversion, which was further investigated by variable temperature IR as well as Raman spectroscopies. The Raman and IR studies focused on the  $\nu_{\text{N}\equiv\text{C}}$  stretching vibration coming from the  $\text{NCS}^-$  ligand, which was detected at  $\sim 2120$  cm<sup>-1</sup> (LS) and  $\sim 2075$  cm<sup>-1</sup> (HS) depending upon the spin state of the Fe(II) center.

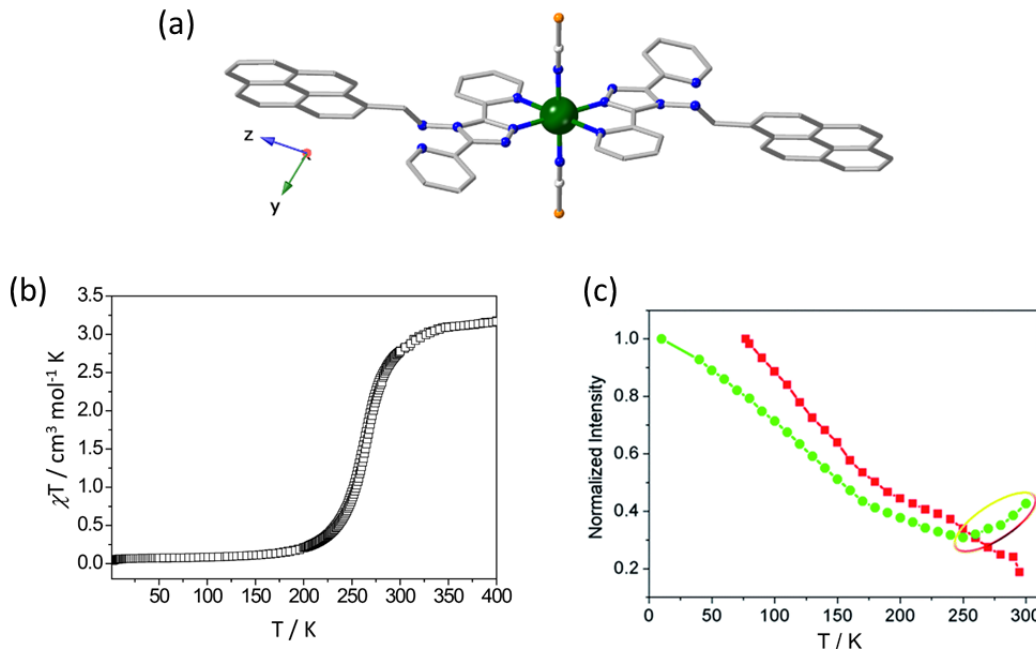


**Fig. 5.** (a) Simplified crystal structure of complex  $[\text{Fe}(\mathbf{L2})_2(\text{NCS})_2]$  (**2**) at 277 K omitting hydrogen atoms for clarity (Fe: green, C: gray, N: blue, S: orange). (b)  $\chi T$  vs T plot for complex **2**. (c) Temperature-dependent behavior of normalized maximum fluorescence emission intensity for the ligand **L2** ( $\lambda_{\text{em}} = 516$  nm) and **2** ( $\lambda_{\text{em}} = 513$  nm at 300–170 K,  $\lambda_{\text{em}} = 498$  nm at 160–10 K). Adapted with permission from Ref. [63].

Temperature-dependent magnetic measurements were performed to further investigate the spin-state switching of **2**. Variable temperature magnetic susceptibility studies showed that the measured  $\chi T$  value decreases abruptly from 2.78 to 0.08  $\text{cm}^3 \text{mol}^{-1} \text{K}$  upon cooling from 300 to 200 K, which on further cooling, reaches a minimum value of 0.08  $\text{cm}^3 \text{mol}^{-1} \text{K}$  at 100 K. These results confirmed a thermo-induced SCO with  $T_{1/2} = 267$  K in **2** (Fig. 5b). Photo-induced SCO between LS and photo-induced metastable HS states were also investigated using laser-light irradiation at 2 K for complex **2**, where the LIESST effect was observed under irradiation with light of 671 nm wavelength with a conversion of 21.3% and  $T_{\text{LIESST}} = 60$  K. Photo-induced HS

state was further characterized by the IR studies by the appearance of  $\nu_{\text{N}\equiv\text{C}}$  stretching vibration at 2080 cm<sup>-1</sup>.

To look for the correlation between luminescence and SCO in **2**, temperature-dependent PL measurements were performed between 10 and 300 K in solid-state for both ligand **L2** and complex **2**. At room temperature, PL spectra displayed an emission band at 516 and 513 nm for **L2** and **2**, respectively under excitation at 380 nm, suggesting retention of the PL properties of the ligand upon coordination with iron(II) center. The variable temperature PL spectra displayed distinct temperature-dependent emission characteristics for **L2** and **2**. Upon cooling, the emission intensity of **L2** increased slowly due to suppression of thermal quenching, while for **2**, the emission intensity initially decreased upon cooling down to the lowest value at 250 K and then gradually increased to reach a maximum at 10 K. The appearance of the abnormal behavior of the emission intensity in the SCO region confirmed the synergic relation between SCO and luminescence in **2**. Additionally, the emission intensity of the HS state compared to the LS state is higher near the SCO region. (Fig. 5c)

Further PL experiments were carried out to explore the luminescence behavior of the photo-induced metastable HS state at 10 K after irradiation over 2 hours, where a significant increase in the emission intensity (19.8%) was noticed, which was consistent with the magnetic response under light irradiation at 10 K. Thermal stability of the photo-induced HS state was further studied by PL measurement, where PL intensity decreased upon increasing the temperature where emission spectrum at 40 K overlapped with the spectrum obtained before irradiation at 10 K. Overall results suggested that PL measurement can be applied to study the photo-induced SCO.

Sato and co-workers reported rhodamine derivatives to explore the synergic relation between SCO and luminescence in mononuclear iron(II) complex [64]. Generally, rhodamine derivatives

exhibit outstanding spectroscopic features, *e.g.*, long-wavelength emission, and high quantum yield with visible-light excitation. Further, rhodamine derivatives containing ring-opened amides as well as spirolactam display ON/OFF luminescence switching depending on the pH or presence of Lewis-base metal ions. The iron(II) mononuclear complex  $[\text{Fe}(\mathbf{L3})_2](\text{ClO}_4)_2 \cdot 3\text{CH}_3\text{OH} \cdot \text{CH}_2\text{Cl}_2 \cdot 0.8\text{H}_2\text{O}$  (**3**) was obtained as reddish-brown single crystals by the reaction of  $\text{Fe}(\text{ClO}_4)_2 \cdot 6\text{H}_2\text{O}$  and two equivalent of the rhodamine incorporated ligand **L3** (**L3** = pyridinecarbaldehyde rhodamine 6G hydrazone; **Scheme 1**) in a 1:1 solvent mixture of MeOH/DCM, and successive diffusion of diethyl ether into the complex solution. An analogous Zn(II) complex  $[\text{Zn}^{\text{II}}(\mathbf{L3})_2](\text{ClO}_4)_2 \cdot 3.78\text{CH}_3\text{OH} \cdot \text{CH}_2\text{Cl}_2$  (**4**) was also synthesized using a similar procedure.

Single-crystal X-ray diffraction studies were performed between 250 and 100 K confirming that complex **3** crystallizes in monoclinic space group  $P2_1/c$ , where iron(II) center in  $\text{N}_4\text{O}_2$  surrounding was coordinated with two tridentate  $\text{N}_2\text{O}$  ligand **L3**. Upon cooling down from 250 to 100 K, no structural phase transition was observed; however, the average Fe–O/N bond distances decreased to 1.964 Å (Fe–O) and 1.989 Å (Fe–N) from 2.072 Å (Fe–O) and 2.164 Å (Fe–N) with a difference ( $\Delta d$ ) of 0.109 Å for Fe–O and 0.175 Å for Fe–N. These values suggested a switch between the HS to LS states in **3**. Moreover, the enolate form of the ligand **L3** was confirmed by the longer C=O bond distance of 1.253(5)–1.282(5) Å in comparison to the free hydrazone ligand (1.23 Å), which was further evidenced by the absence of the  $1714\text{ cm}^{-1}$  band for C=O in IR spectrum of **3**. Moreover, several strong intermolecular  $\pi \cdots \pi$  interactions were present between parallel xanthene units (Fig. 6a).

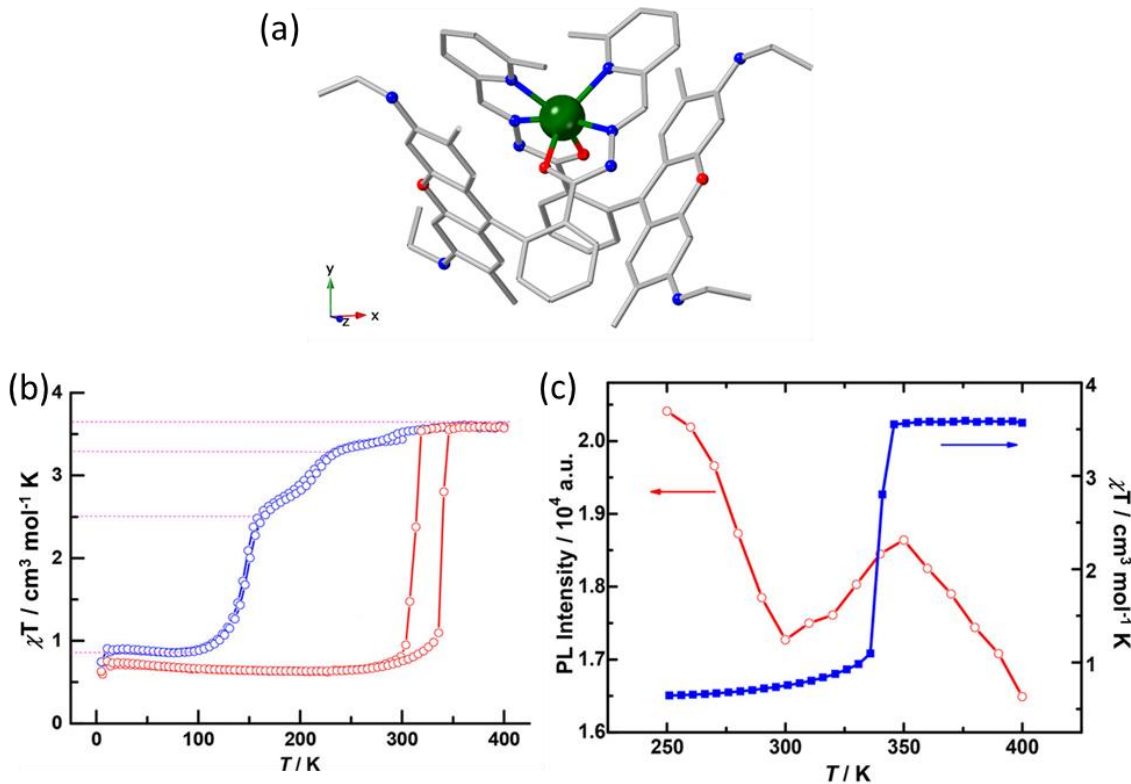


**Fig. 6.** (a) Simplified crystal structure of complex cation in  $[Fe(L3)_2](ClO_4)_2 \cdot 3CH_3OH \cdot CH_2Cl_2 \cdot 0.8H_2O$  (3) at 250 K. For clarity hydrogen atoms and counteranions are omitted (Fe: green, C: gray, N: blue, O: red). (b)  $\chi T$  vs T plot for complex 3 and its desolvated complex 3-d. (c) Plot of  $\chi T$  along with the fluorescence intensity of the maximum emission ( $\lambda_{em}$  = 560 nm) for 3-d. Adapted with permission from Ref. [64].

Temperature-dependent magnetic properties of 3 were performed between 300 – 2 K. The measured  $\chi T$  value at 300 K was  $3.4\text{ cm}^3\text{ mol}^{-1}\text{ K}$ , confirming the HS state of 3 with significant orbital contributions. Upon lowering the temperature, the  $\chi T$  vs. T plot displays a three-step transition with the inflection points of 240, 160, and 100 K corresponding around 93%, 71%, and 25% of the HS Fe(II) in 3, respectively.  $\chi T$  vs. T plot in the heating mode from 2 - 300 K almost overlapped with the cooling mode without any hysteresis loop. Overall results confirmed a reversible three-step SCO in 3. The presence of competing opposite intra- or intermolecular short

interactions and long-range elastic interactions in **3** might be responsible for such a three-step SCO (Fig. 6b).

Upon increasing the temperature to 400 K, the measured  $\chi T$  value increase slightly *i.e.*, 3.6 cm<sup>3</sup> mol<sup>-1</sup> K. Remarkably, upon cooling down, the desolvated sample **3-d** exhibited a significantly different SCO behavior in comparison to the complex **3**. **3-d** showed sharp transitions at 343 K ( $T_{1/2}\uparrow$ ) and 303 K ( $T_{1/2}\downarrow$ ) with a sweep rate-independent (1 – 10 K/min) wide hysteretic loop of 40 K, indicating important role played by the guest solvent molecules through a change in intermolecular interactions upon desolvation. SCO in **3-d** was further supported by DSC and Mössbauer measurements. DSC experiments revealed endothermic/exothermic peaks at 340 K/306 K, confirming the first-order transition with hysteresis, while Mössbauer spectra exhibited quadrupole splitting ( $\Delta E_Q$ ) with isomer shift ( $\delta$ ) in the span 1.85–2.95 and 0.74–1.11 mm s<sup>-1</sup> confirming the HS Fe(II) at 292 K and 1.08–1.093 and 0.27–0.341 mm s<sup>-1</sup> for LS state at 77 K. Moreover, complex **3-d** exhibited the LIESST effect with a 10% photo-conversion from LS state to HS photo-excited state upon irradiation with green light ( $\lambda = 560$  nm) for 7 h at 5 K.

Variable temperature PL studies of **3-d** in between 250 and 400 K showed that upon heating from 250 K, the PL intensity maxima of the  $\lambda_{\text{max}} = 560$  nm typical of rhodamine 6G ( $I_{\text{em}}$ ) decreases to reach a minimum at 300 K for the thermal quenching effect. Further, with an increase in temperature,  $I_{\text{em}}$  showed an increase to attain a maximum value at 350 K, then  $I_{\text{em}}$  decreased upon increasing temperature up to 400 K. In contrast, the analogs Zn(II) complex (**4**) displayed a continuous decrease in emission intensity while increasing temperatures. Moreover, in cooling mode, a similar discontinuous nature in  $I_{\text{em}}$  was observed between 300 and 310 K, consistent with the SCO at 303 K ( $T_{1/2}\downarrow$ ). Overall, all these results concluded that the luminescence emission of **3**-

**d** is affected by the SCO process, where the emission of **3-d** can be quenched by the LS Fe(II) state (Fig. 6c).

In 2019, Boukheddaden and co-workers explored the interplay between luminescence and SCO in a multifunctional iron(II) complex [65]. The iron complex along with an analogous copper(II) complex, namely,  $[M(\mathbf{L4})_6](tcnsme)_2 \cdot 4CH_3CN$  ( $M = Fe^{II}$  (**5**); **L4** = N-(1,2,4-triazol-4-yl)-1,8-naphthalimide (**Scheme 1**);  $(tcnsme)^- = 1,1,3,3$ -tetracyano-2-thiomethylpropenide anion) were prepared by the reaction of  $[M(BF_4)_2] \cdot xH_2O$ , **L4** and K(*tcnsme*) in a 1:6:2 molar ratio under an aerobic and reflux conditions in acetonitrile.

Single crystal X-ray diffraction studies at 296 and 100 K showed the presence of the iron center in the  $FeN_6$  surrounding, coordinated with six nitrogen donor atoms from the monodentate **L4** ligand. At 296 K, the average Fe–N bond distance is 2.189(4) Å, indicating the HS state of Fe(II) in **5**. Upon cooling down to 100 K, the average Fe–N bond distance reduces significantly to 1.995(4) Å, which lies in the expected range for the Fe(II) ion in the LS state. These observations suggest a thermo-induced SCO from HS to LS in **5** (Fig. 7a).

Temperature dependency of the magnetic properties was investigated by measuring  $\chi T$  vs. T in the temperature range of 300 - 2 K. The measured  $\chi T$  value at 300 K was  $3.9 \text{ cm}^3 \text{ mol}^{-1} \text{ K}$  ( $S = 2$ ,  $g \approx 2.28$ ) confirming the HS state of Fe(II) in **5**. Upon cooling down, the  $\chi T$  value decreases gradually to attain a plateau of  $0.45 \text{ cm}^3 \text{ mol}^{-1} \text{ K}$  below *ca.* 70 K, suggesting a gradual SCO with a  $T_{1/2}$  value of 114 K. The photomagnetic studies under green laser (532 nm) irradiation for *ca.* 2 h at 10 K revealed that upon irradiation, the  $\chi T$  value shows a continuous increase to reach a saturation value of  $2.8 \text{ cm}^3 \text{ mol}^{-1} \text{ K}$ , describing a complete photo-conversion from LS state to photo-induced HS state, which shows relaxation back to the LS ground state at 55 K ( $T_{LIESST} = 55$  K) upon heating in dark (Fig. 7b).

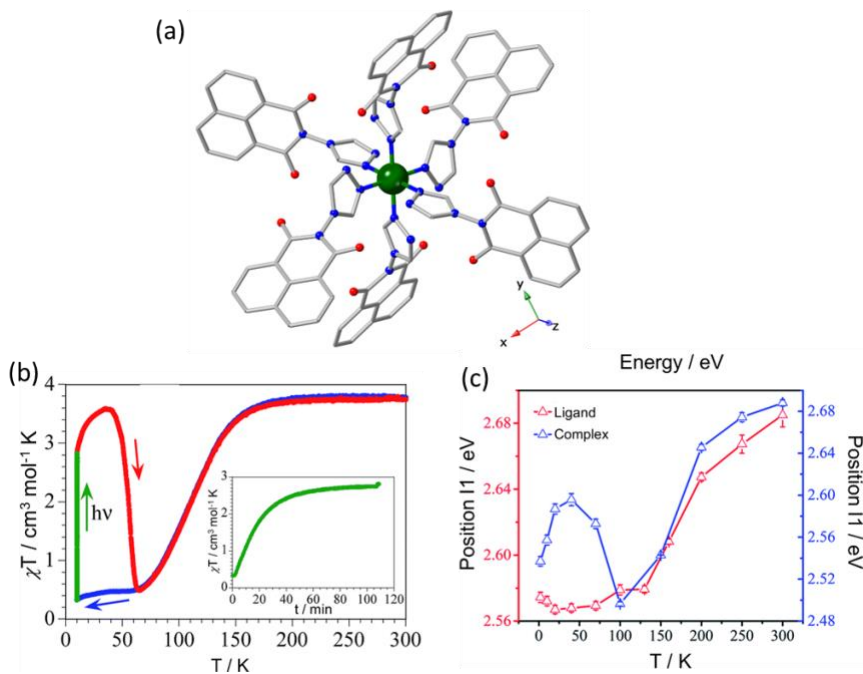


**Fig. 7.** (a) Simplified crystal structure of complex cation in  $[\text{Fe}(\textbf{L4})_6](\text{tcsme})_2 \cdot 4\text{CH}_3\text{CN}$  (**5**) at 296 K omitting hydrogen atoms and counteranions for clarity (Fe: green, C: gray, N: blue, O: red). (b) Plot of  $\chi T$  vs T for complex **5**, blue points indicate the dark cooling, green points indicate irradiation at 10 K, red points indicate heating in dark after the irradiation. (c) Difference in the thermal behavior of the emission of the peaks I1 (486 nm) for the complex **5** and ligand **L4**. Adapted with permission from Ref. [65].

Variable temperature PL studies of the ligand **L4** and complex **5** were performed between 300 and 2 K. The emission spectrum of **L4** showed two PL peaks centered at 412 (I2) and 486 (I1) nm at 2 K. Upon increasing the temperature, the position and the FWHM of 486 nm peak increases monotonously. In contrast, the emission spectrum of **5** at 2 K shows two additional bands at around 600 (I3) and 445 (I4) nm, along with slightly blue-shifted ligand-based peaks I1 and I2. Temperature dependence of the peak I1 shows a monotonous blue shift for the ligand, while a regime change around 100 K was observed for complex **5**. Further, temperature dependency of the I3 peak around 2 eV (600 nm) shows a nice correlation with the temperature dependence of the

HS fraction derived from magnetic measurements in SCO region 70 – 180 K, confirming the existence of a synergic relation between SCO and luminescence in **5** (Fig. 7c).

In 2021, Zhu and co-workers reported a mononuclear magneto-fluorescence bifunctional Fe(II) SCO complex  $[\text{Fe}(\text{L5})_2](\text{ClO}_4)$  (**6**) where, **L5**=(2,2’-(4-(pyren-1-yl)pyridine-2,6-diyl)bis(4,4-dimethyl-4,5-dihydrooxazole)) (**Scheme 1**) [66]. The single crystal x-ray structure analysis shows that complex **6** crystallizes in the  $P2_1/c$  space group and the asymmetric unit contains one crystallographically independent iron center with  $Z=4$  (Fig. 8a). The Fe(II) center sits inside a  $\text{N}_6$  coordination environment with six nitrogen atoms coming from two perpendicularly arranged **L5** ligand. There are several weak interactions present in the system, such as weak C-H $\cdots$ O interactions in between  $[\text{Fe}(\text{L5})_2]^{2+}$  cation and two perchlorate counteranions, and the presence of  $\pi\cdots\pi$  stacking in between the pyrene rings with a distance of 3.76 Å. The average Fe-N bond length of 2.178 Å at 153 K suggests the predominance of the Fe(II) HS state.

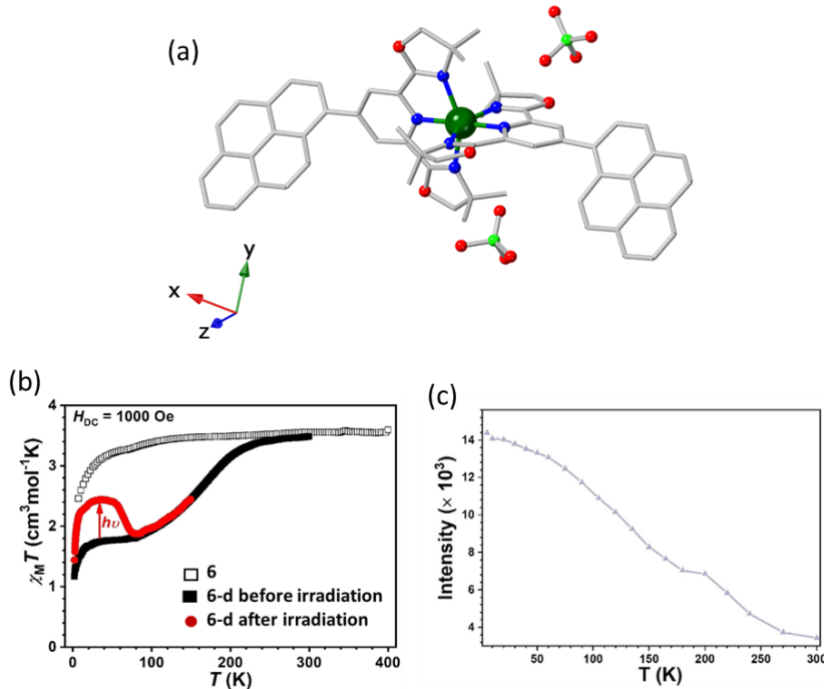


**Fig. 8.** (a) Simplified crystal structure of complex **6** omitting hydrogens atoms for clarity (Fe: green, C: gray, N: blue, O: red, Cl: light green). (b) Solid state magnetic data of fresh crystals of complex **6** (black hollow rectangles), desolvated sample **6-d** (black solid rectangles and red solid circles). (c) Plot of normalized emission intensity vs temperature for complex **6**. Adapted with permission from Ref. [66].

Solid-state magnetic measurements were carried out the fresh crystals to inquire about the SCO properties of complex **6**. At temperatures 293 K and 153 K, the results are in agreement with the Fe(II) system in the HS state (Fig. 8b). For the desolvated sample **6-d**, the  $\chi T$  vs. T plot revealed a SCO behavior. At 300 K, the  $\chi T$  value for **6-d** is  $3.48 \text{ cm}^3 \text{ mol}^{-1} \text{ K}$ , corresponding to Fe(II) HS state. Upon decreasing temperature, the  $\chi T$  value slowly decreases to  $1.78 \text{ cm}^3 \text{ mol}^{-1} \text{ K}$  at 60 K. Overall, complex **6-d** shows a gradual incomplete SCO with a  $T_{1/2}$  of 173 K. From the  $\chi T$  vs. T plot, it was estimated that 50% of the Fe(II) ions show conversion from LS to HS state (Fig. 8b). The complex also indicates 40% LS-to-HS conversion after photoirradiation with green light ( $\lambda = 532 \text{ nm}$ ) at 2 K, reaching a maximum value of  $2.58 \text{ cm}^3 \text{ mol}^{-1} \text{ K}$  at 35 K. Solid-state variable

temperature fluorescence emission spectra were recorded for complex **6** and **6-d** in the temperature range of 80-300 K to study the synergistic correlation of SCO and luminescence. The optimum excitation wavelength came to be 375 nm for **6-d**. Upon excitation, a broad emission band came in the 370 to 700 nm range, with the maximum emission at 420 nm. The band is attributed to the  $\pi-\pi^*$  transition of the pybox moiety from the ligand backbone. The emission intensity continuously increases by lowering the temperature to 5 K due to the restriction of non-radiative transition processes at the low temperature (Fig. 8c).

Although no direct synergy between SCO and luminescence was observed, the variable temperature solid state UV-Vis absorption spectra of **6-d** showed distinct changes as emergence of absorption band in the range of 600 - 760 nm coming from the  ${}^1\text{A}_1 \rightarrow {}^1\text{T}_1$  transition from the Fe(II) LS unit upon cooling from 300 K to 80 K. So, the effective spectral overlap of SCO unit with the fluorophore units appeared to be a key factor for the construction of bifunctional SCO-fluorescent complexes.

In 2022, Liu and co-workers devised a rational strategy to construct multifunctional materials with synergistic luminescence and SCO properties. In this work, a mononuclear complex  $[\text{Fe}(\text{L6})_2(\text{SeCN})_2] \cdot 4\text{DMF}$  (**7**) (**L6**=(4-(1,1,2,2-tetraphenylethene))-N-(3,5-bis(pyridin-2-yl)-4H-1,2,4-triazol-4yl)methanimine) (**Scheme 1**) was prepared that showed thermally induced SCO along with aggregation-induced-emission (AIE) properties [67].

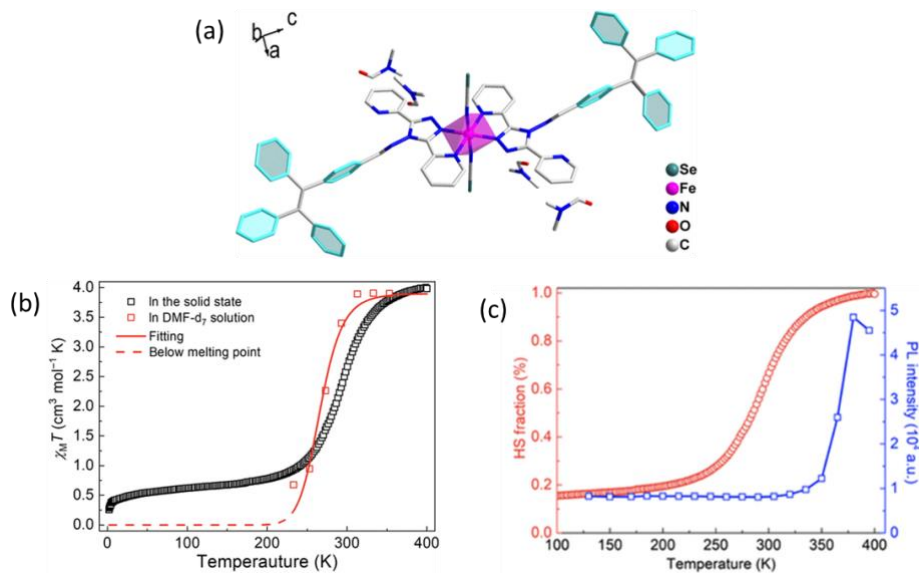


**Fig. 9.** (a) Simplified crystal structure of complex 7 omitting hydrogen atoms for clarity (Fe: Pink, C: gray, N: blue, O: red, Se: green); (b)  $\chi T$  vs T plot for solid samples of complex 7 (black hollow rectangles) along with variable temperature Evans NMR (red hollow rectangles). (c) Plot of HS fraction for complex 7 and normalized PL intensity with temperature showing synergy of SCO and luminescence. Adapted with permission from Ref. [67].

Single crystal x-ray diffraction analysis showed that the complex crystallizes in the triclinic *P*1 space group. The Fe(II) ion sits in a N<sub>6</sub> coordination environment where two axial N atoms come from two isoselenocyanate anions, and four N atoms are from two ligands (Fig. 9a). The average Fe-N bond distances for Fe-N<sub>triazole</sub>, Fe-N<sub>pyridyl</sub> and Fe-N<sub>SeCN</sub> bonds are 1.969(1) Å, 2.015(1) Å and 1.943(1) Å, respectively at 110 K showing a characteristic of Fe(II) LS species. Upon increasing the temperature to 300 K, the bond distances change to 2.133(4) Å, 2.225(4) Å and 2.108(6) Å, respectively for the Fe-N<sub>triazole</sub>, Fe-N<sub>pyridyl</sub> and Fe-N<sub>SeCN</sub> bonds, suggesting the occurrence of the SCO from LS to HS state, also affecting the intermolecular weak interactions between the phenyl rings with other groups to restrict their rotation and movement.

Temperature-dependent solid-state magnetic susceptibility measurement on the complex **7** revealed a gradual spin-state switching in the temperature range of 200 to 400 K (Fig. 9**b**). At 400 K, the  $\chi T$  value of  $3.98 \text{ cm}^3 \text{ mol}^{-1} \text{ K}$  is observed and in good agreement with the typical mononuclear Fe(II) HS species. The  $\chi T$  value drops to  $0.78 \text{ cm}^3 \text{ mol}^{-1} \text{ K}$  at 200 K upon cooling, indicating the thermally induced SCO process. Solution-based magnetic studies were also performed via Evans method NMR in deuterated DMF solvent in the temperature range of 233–353 K, showing a similar gradual profile of the SCO process with  $\chi T$  value varying from 0.68 to  $3.90 \text{ cm}^3 \text{ mol}^{-1} \text{ K}$  from 233 to 353 K (Fig. 9**b**). The  $T_{1/2}$  value for the SCO process was observed at 295 K for the solid state while 265 K in the solution state since dilution in the solution can largely reduce the co-operativity in between the SCO centers.

The luminescence property of the AIEgens (AIE=aggregation induced emission luminogens) depends on the modification of conformational and intermolecular interactions in contrast to the classical organic luminophores. The temperature-dependent emission spectra of **7** was measured with an excitation wavelength of 365 nm. The emission maximum around 483 nm shows a decrease in intensity while heating from 130 K, reaching the minimum at 290 K. Afterwards, the PL intensity starts to increase, and a notable abrupt increase is observed between 330 and 380 K, reaching the maximum at 380 K close to the temperature where SCO is completed (Fig. 9**c**). This shows the synergy between the SCO and luminescent property. To describe the coupling between luminescence and SCO, variable temperature UV-Vis absorption spectra of **7** was measured in the range of 210–400 K, but the small change in the spectral intensity at 500 nm corresponding to the transition from the  ${}^1\text{A}_1 \rightarrow {}^1\text{T}_1$  of the Fe(II) LS ion in the temperature range of 210–380 K couldn't explain the large change in the PL intensity.

To address the issue, single crystal structures of **7** were compared at different temperatures. This revealed exciting changes in the intermolecular short interactions while changing the temperature from 110 K to 300 K with an increase in the average short intermolecular distance. The number of different short-contact interactions drastically reduced from 15 to 5 upon going from 110 K to 300 K, along with an increase in the average intermolecular short-contact distance from 2.793 Å to 2.845 Å. Altogether, the loss of intermolecular interactions and the increase of the distance between tpe (tpe = tetraphenylethylene) units appeared to be the sole reason for reducing the efficiency of energy transfer between tpe units, deactivating the nonradiative decay and giving rise to a remarkable increase in the PL intensity.

Li and co-workers reported two complexes with the same ligand **L6**,  $[\text{Fe}(\text{L6})_2(\text{NCS})_2] \cdot 4\text{MeCN}$  (**8**) and  $[\text{Fe}(\text{L6})_2(\text{NCS})_2] \cdot 2\text{MeCN} \cdot 2\text{CH}_2\text{Cl}_2$  (**9**) [68]. Both the complexes show incomplete SCO. Interestingly, the synergy between the SCO and luminescence property was found not only around the  $T_{1/2}$  values but also in the entire SCO range from 80 K to 300 K, which is rare. The solid-state magnetic susceptibility measurements showed a complete one-step abrupt transition for the complexes **8** and **9** with ~74 K difference in the  $T_{1/2}$  temperature (**8** with  $T_{1/2}$  of 129 K and **9** with a  $T_{1/2}$  of 203 K). The average Fe-N bond distances at 100 K were found to be 1.9821 Å and 1.9756 Å, respectively for complexes **8** and **9**. At 300 K, the average Fe-N bond distances change to 2.1544 Å and 2.1552 Å, respectively for complexes **8** and **9**, suggesting conversion of Fe(II) LS to Fe(II) HS state. The Fe-N<sub>isothiocyanate</sub>-C angles for the complexes are larger in the LS state than the HS state, influencing differences in crystal packing as well as intermolecular interactions, thus leading to different magnetic properties.

To correlate the SCO process and luminescence, variable temperature fluorescence emission spectroscopy was measured in the range of 100 K and 300 K. For complex **8**, two fluorescence

emission peaks at 441 nm and 465 nm were observed, and the relative intensities of the two bands gradually increase in the temperature range of 100-220 K, which is well consistent with the magnetic data. For complex **9**, the intensity of the emission band at 457 nm shows a similar trend when going from 190 K to 320 K, correlating with the thermally induced spin transition process. Thus, SCO can significantly influence the fluorescence intensity, which can be utilized to develop advanced magneto-optical devices.

As the bifunctional fluorescent complexes incorporating AIEgens are growing interest in recent times, Liu and co-workers reported a series of SCO-fluorescent bifunctional Fe(II) complexes based on tpe fluorophore decorated ligand **L7**, (**L7**=(E)-2,6-bis(1*H*-pyrazol-1-yl)-4-(4-(1,2,2-triphenylvinyl)styryl)pyridine (tpe-bpp)) (**Scheme 1**). Further, three Fe(II) complexes  $[\text{Fe}(\text{L7})_2](\text{ClO}_4)_2 \cdot 5.75\text{CH}_2\text{Cl}_2$  (**10**),  $[\text{Fe}(\text{L7})_2](\text{ClO}_4)_2 \cdot \text{CH}_2\text{Cl}_2 \cdot 3\text{CH}_3\text{OH}$  (**11**) and  $[\text{Fe}(\text{L7})_2](\text{BF}_4)_2 \cdot \text{CH}_2\text{Cl}_2 \cdot 3\text{CH}_3\text{OH}$  (**12**) were synthesized (Fig. 10a) [69]. Solid-state magnetic measurements on polycrystalline samples of **10**, **11**, and **12** suggested a complete one-step SCO with the  $T_{1/2}$  temperatures of 375 K, 260 K, and 248 K, respectively (Fig. 10b).

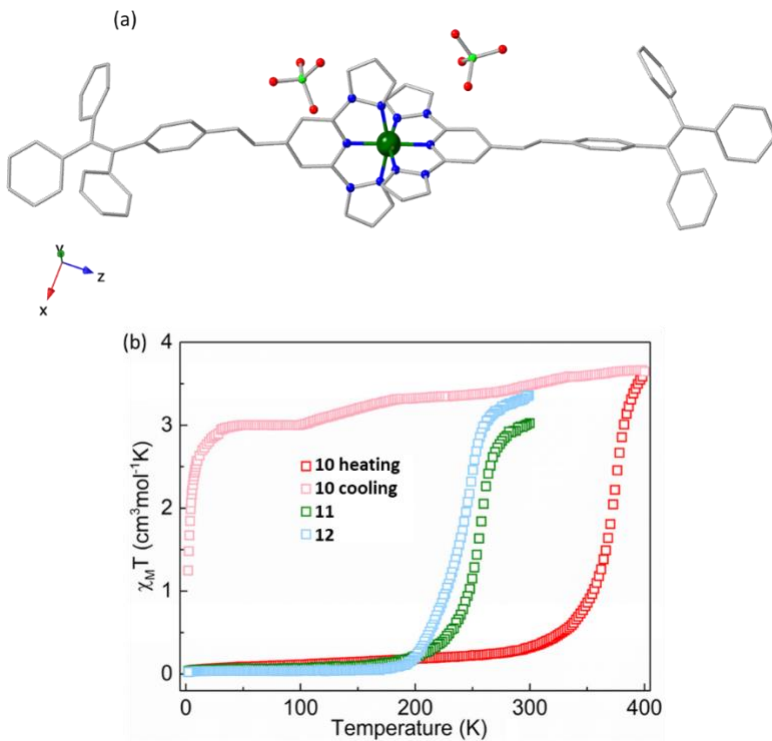


**Fig. 10.** (a) Simplified crystal structure of  $[\text{Fe}(\text{L7})_2](\text{ClO}_4)_2$  unit, for clarity hydrogen atoms are omitted (Fe: green, C: gray, N: blue, O: red, Cl: light green); (b)  $\chi T$  vs T plot for the complexes **10** (red), **11** (green), **12** (blue). Complex **10** remains in the HS state after loosing the lattice solvents at high temperature. Adapted with permission from Ref. [69].

The magnetic data shows that the lattice solvents have a more notable effect on the SCO properties than variation of the counteranions, which again can modify the local structure and cooperativity between SCO centers. To study the synergy between fluorescence and SCO properties, variable temperature fluorescence emission spectra were recorded on all the complexes **10**, **11**, and **12**, in the range of 100 K and 300 K. The maximum emission intensity of the complexes **10-12** show monotonic decrease while heated from 100 K to 300 K, with indication of coexisting SCO and fluorescence property. However, no anomalous change in the fluorescence emission in the SCO range suggests a lack of direct synergy between SCO and fluorescence. The reason for

the observed effect is due to the far distance of the luminophore from Fe(II) SCO center as well as the short interactions between counteranions/solvent molecules and fluorophore failing to produce enough variations in the conformation of the fluorophore to overcome the thermal quenching. Overall, this work explores the strategy to involve functional units such as fluorescent and conductive molecules to construct multifunctional SCO molecular materials.

Meng and co-workers reported two bifunctional Fe(II) complexes,  $[\text{Fe}(\text{L8})_2](\text{ClO}_4)_2$  (**13**) and  $[\text{Fe}(\text{L9})_2](\text{ClO}_4)_2 \cdot 2.63\text{CH}_2\text{Cl}_2$  (**14**) (**L8**=4-(naphthalen-1-yl)-2,6-bis(1-pyrazolyl)pyridine, **L9**=(*E*)-2,6-bis(1-pyrazolyl)-4-(2-(pyren-1-yl)vinyl)pyridine) (**Scheme 1**) based on modified bis(pyrazole)pyridine ligands with synergistic effect between fluorescence and SCO in **13** [70].

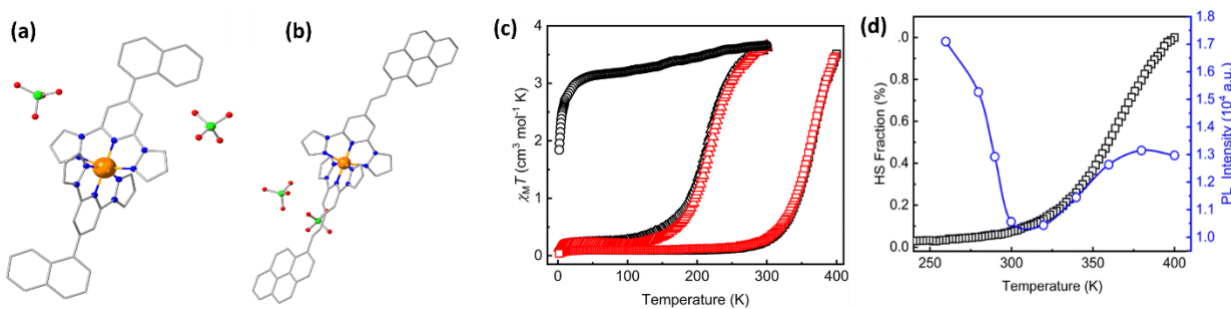


**Fig. 11.** (a) Simplified crystal structure of complex **13** (b) Simplified crystal structure of complex **14**, for clarity hydrogen atoms are omitted (Fe: orange, C: gray, N: blue, O: red, Cl: green). (c) Variable temperature solid state magnetic measurement data for complex **13** (red and black rectangles), for complex **14** (red and black triangles), and desolvated complex **14-d** (black circles). (d) Correlation of temperature-dependent HS fraction and PL intensity with temperature for complex **13**. Adapted with permission from Ref. [70].

Single crystal x-ray structure analysis revealed that at 120 K, complex **13** crystallizes in orthorhombic space group *Pcc*a, the Fe(II) center sits in a distorted octahedral  $\text{N}_6$  coordination geometry (Fig. 11a). The average  $\text{Fe}-\text{N}_{\text{pyridyl}}$  and  $\text{Fe}-\text{N}_{\text{pyrazole}}$  bond distances of 1.8964(19) Å and

1.964(2)-1.966(2) Å suggests the Fe(II) center present in LS state. Upon increasing temperature to 400 K, the average Fe-N<sub>pyridyl</sub> and Fe-N<sub>pyrazole</sub> bond distances increase to 2.054(6) Å and 2.111 Å, suggesting a change of spin-state from LS to HS state. Complex **14** crystallizes in triclinic *P*-1 space group, and at 120 K, the average Fe-N<sub>pyridyl</sub> and Fe-N<sub>pyrazole</sub> bond distances of 1.889 Å and 1.973 Å indicate the presence of Fe(II) LS state (Fig. 11**b**). In both complexes, the short intermolecular interactions help form an extended network, *i.e.*, a “W”-shaped plane for the complex **13** and a planar 2D network for the complex **14**.

Temperature dependent magnetic susceptibility measurements on complexes **13** and **14** revealed the occurrence of SCO behavior in both complexes (Fig. 11**c**). At 400 K, the observed  $\chi T$  value 3.51 cm<sup>3</sup> mol<sup>-1</sup> K for complex **13**, is typical for mononuclear Fe(II) HS complex. Upon decreasing temperature, the  $\chi T$  value decreases sharply first, then slowly decreases below 300 K, finally reaching a  $\chi T$  value of 0.04 cm<sup>3</sup> mol<sup>-1</sup> K, showing the characteristic of Fe(II) LS ion. For complex **14** also,  $\chi T$  vs. T plot revealed similar SCO behavior while going from 2 K to 300 K. At 300 K, the  $\chi T$  value of 3.66 cm<sup>3</sup> mol<sup>-1</sup> K corresponding to Fe(II) HS state decreases sharply upon initial cooling, then decreasing slowly below 150 K, finally reaching a minimum value of 0.14 cm<sup>3</sup> mol<sup>-1</sup> K at 2 K. The influence of solvent molecules on the spin state was also investigated, and it was observed that the desolvated sample **14-d** didn't show any SCO behavior and remained in the HS state over the temperature range of 2-300 K.

To find out the correlation between SCO and fluorescence property, temperature-dependent fluorescence emission spectra were recorded for complexes **13** and **14** along with the ligands **L8** and **L9**. The temperature-dependent fluorescence spectra of the ligand **L8** show a monotonous decrease in the intensity upon increasing the temperature due to the enhancement of non-radiative

transitions. For complex **13**, temperature-dependent emission spectra show a decreasing nature for the intensity in the range of 260-300 K. Afterwards, the fluorescence intensity starts to increase slowly in the range of 300-380 K, close to the temperature range of the SCO process (Fig. 11d). After 400 K, thermal quenching effects predominate, and a decrease in the emission intensity was observed again. In contrast to the ligand, the abnormal evolution of the fluorescence emission spectra for complex **13** indicates a direct synergy between the SCO and luminescence properties. For complex **14** also, the coexistence of SCO and luminescence was observed, but no direct synergy between them, as may be due to the far distance between the Fe(II) SCO centers and the luminophore as well as for many weak interactions present in the system leading to energy dissipation by non-radiative pathways.

The development of advanced multifunctional devices requires molecular systems that can switch the physical properties upon the application of mild external stimuli. Recently, Cano and co-workers reported the SCO active Co(II) molecular nanomagnet that can exhibit pH-based switching of luminescent, redox, and magnetic properties [71]. Two complexes  $\{[\text{Co}(\text{HL10})_2][\text{Co}(\text{HL10})(\text{L10})]\}$  ( $\text{ClO}_4$ )<sub>3</sub>·9H<sub>2</sub>O (**15**) and  $[\text{Co}(\text{L10})_2]$ ·5H<sub>2</sub>O (**16**) (**HL10** = (4-carboxyphenyl)-2,2':6',2''-terpyridine) (**Scheme 1**) were prepared by the reaction of  $\text{Co}(\text{ClO}_4)_2$ ·6H<sub>2</sub>O and **HL10** in acetonitrile/methanol as solvent (**15**) or reaction of  $\text{Co}(\text{OAc})_2$ ·4H<sub>2</sub>O and **NaL10** in DMSO/water mixtures (**16**).

In complex **15**, a statistical disorder is present in Co(II) complex cations  $[\text{Co}(\text{HL10})_2]^{2+}/[\text{Co}(\text{HL10})(\text{L10})]^{2+}$  together with counteranions  $\text{ClO}_4^-$  and crystallization water molecules. Complex **16** only contains mononuclear neutral  $[\text{Co}(\text{L10})_2]$  unit with free water molecules. The comparison between C-O bond length in the carboxyl/carboxylate groups shows that although the bond lengths are quite different in complex **15** ( $d_{\text{C}-\text{O}} = 1.203(6)/1.216(7)$  and  $d_{\text{C}-$

$d_{\text{C}-\text{O}} = 1.310(5)/1.294(7)$  Å), they are similar for the complex **16** ( $d_{\text{C}-\text{O}} = 1.263(3)/1.256(4)$  and  $d_{\text{C}-\text{O}} = 1.260(4)/1.252(4)$  Å). In both complexes, the octahedral coordination sphere exhibits some distortions. The average Co(II)-N distances at 120 K are of typical Co(II) LS form.. The difference in the weak interactions between the complex cation and solvent molecules and counteranions is the reason for the difference in the crystal packing for the two pH-dependent isomers.

To understand the effect of protonation on the spin-state, magnetic measurements were performed on both complexes **15** and **16**. The  $\chi T$  vs. T plot shows a similar gradual SCO behavior for both **15** and **16**, with no effect of the protonation level on SCO. Around room temperature, the  $\chi T$  value for complex **15** is  $0.62 \text{ cm}^3 \text{ mol}^{-1} \text{ K}$ , whereas  $0.75 \text{ cm}^3 \text{ mol}^{-1} \text{ K}$  for complex **16**, both are much less than the expected value for a HS Co(II) ion ( $2.7 \text{ cm}^3 \text{ mol}^{-1} \text{ K}$ ,  $S=3/2$ ,  $g=2.4$ ). The  $\chi T$  value decreases to  $0.41 \text{ cm}^3 \text{ mol}^{-1} \text{ K}$ , reaching a plateau of around 150 K, matching the expected value for one Co(II) LS ion ( $0.45 \text{ cm}^3 \text{ mol}^{-1} \text{ K}$ ,  $S=1/2$ ,  $g=2.2$ ). The electronic emission spectra of both the complexes  $[\text{Co}(\text{HL10})_2]^{2+}$  and  $[\text{Co}(\text{L10})_2]$  ( $\lambda_{\text{excitation}} = 295 \text{ nm}$ ) show emission in near UV region at 370 nm having shoulder around 465 nm. The emission intensity decreased fivefold compared to the respective ligand counterparts because of the quenching effect after coordinating with Co(II) ion. To observe the pH effect on the emission intensity of complex **15**, emission spectra were recorded upon acid-base titration of 0.01 mM DMSO/H<sub>2</sub>O solution at 298 K. Changing the pH from 2.8 to 6.9 resulted in enhancement of the fluorescence intensity of the asymmetric band centered at 370 nm due to the deprotonation of the ligand to form completely  $[\text{Co}(\text{L10})_2]$  species. The reversible trend observed upon protonation of the ligand suggests the change in the fluorescence intensity coming from the alteration in the electron-donor characteristics of the benzoate group. This leads to changes in the electronic configuration, affecting spin-orbit coupling and promoting deactivation of the emitting state. The quenching of fluorescence intensity upon

protonation can be associated with a state having different spin moments, which is only possible in spin-transition systems. From the study of the variation of the fluorescence intensity ( $I/I_0$ ) upon changing pH *via* acid-base titration, it was concluded that around pH = 4, all three protonated, semi-protonated, and deprotonated species are in coexistence with a high degree of overlap. Overall, this study proposes a new optical (luminescent) acid sensor based on switching the fluorescence emission intensity.

In 2023, Rentschler and co-workers reported an interplay between SCO and luminescence in a mononuclear Fe(II) complex [72]. The complex  $[\text{Fe}(\text{L11})(\text{NCBH}_3)_2] \cdot 1.5 \text{ CH}_3\text{OH}$  (**17**) (**L11** = 2-(naphthalen-2-yl)-5-[N,N-bis(2-pyridylmethyl)aminomethyl]-1,3,4-oxadiazole) (**Scheme 1**) was prepared by reaction of  $[\text{Fe}(\text{py})_4(\text{NCBH}_3)_2] \cdot 2.5\text{H}_2\text{O}$  with **L11** in methanol. Slow evaporation of the methanol solution afforded orange block crystals of **17**.

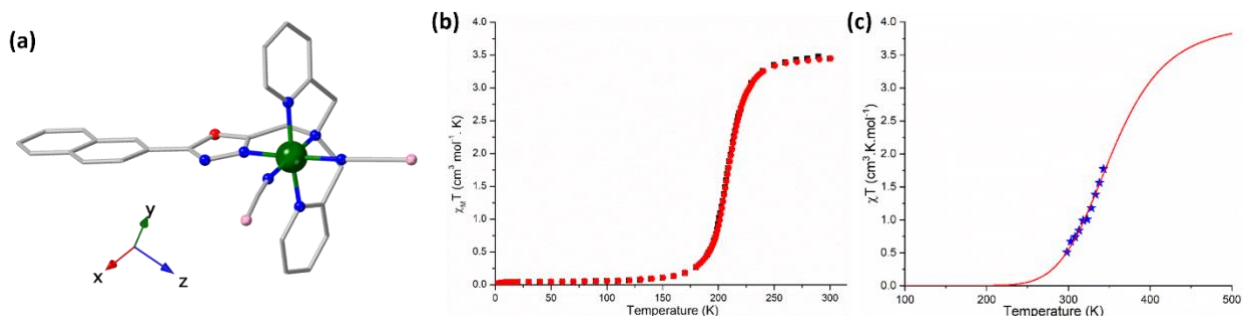


**Fig. 12.** (a) Simplified crystal structure of complex **17**, for clarity hydrogen atoms are omitted (Fe: green, O: red, N: blue, B: light pink); (b)  $\chi T$  vs T data from variable temperature solid-state magnetic measurement for the complex **17**; (c)  $\chi T$  vs T data from solution state variable temperature Evans NMR method for complex **17**. Adapted with permission from Ref. [72].

To correlate the change in the bond length with the spin state change, single crystal XRD data was measured at 120 K. At this temperature, the complex **17** crystallizes in the monoclinic *C2/c*

space group (Fig. 12a). The average Fe-N bond distance is 1.97 Å, suggesting the presence of Fe(II) LS state. At 220 K, the crystal retains the same space group; however, a distinct change is observed in the average Fe-N bond distance, *i.e.*, 2.17 Å, typical for Fe(II) HS ion, along with increased distortion in the coordination sphere and 5% increase in the unit cell volume. These results agreed well with the solid-state magnetic measurements, which reveals an abrupt and complete SCO with a  $T_{1/2}$  of 207 K (Fig. 12b). At 300 K, the  $\chi T$  value of  $3.45 \text{ cm}^3 \text{ mol}^{-1} \text{ K}$  ( $g=2$ ) is typical for the  ${}^5\text{T}_{2g}$  HS ground state. After increasing the temperature to 400 K, the  $T_{1/2}$  slightly shifts higher to 210 K due to the loss of solvent methanol molecules. The SCO in the solution state was also studied *via* variable temperature Evans  ${}^1\text{H}$ -NMR method in  $\text{CD}_3\text{CN}$  from 298 to 343 K and fitted by regular solution model. The  $T_{1/2}$  for the SCO in solution state was found to be 357 K (Fig. 12c).

The ligand **L11** was designed such a way that it should have a tetradeятate binding cavity with the naphthyl luminophore. The PL spectra at room temperature and 77 K were measured for the ligand **L11** and the complex **17**, and the emission spectra of the complex are close to the emission of the naphthalene from the ligand. To investigate the thermal dependency of the of the emission intensity, a series of time-dependent measurements was carried out on complex **17**. The intensity of the fluorescence gradually decreases with time (with temperature therefore), although not following a steady nature. The normalized emission intensity decreases sharply between 10 min and 20 min, again decreasing progressively until reaching a plateau of about 60 min, around 10% intensity. From the time evolution of the emission spectra, an interplay between SCO and luminescence is indicated until 20 min, after which thermal quenching takes over.

In 2023, Guo and co-workers reported a SCO complex based on Fe(II) ( $[\text{Fe}(\text{L12})_2(\text{NCS})_2] \cdot 2\text{DMF}$  (**18**), where **L12** = N-[3,5-di(pyridin-2-yl)-4H-1,2,4-triazol-4-yl]-1,8-

naphthalimide) (**Scheme 1**) with synergy of ratiometric fluorescence for application in thermosensing [73]. The system consists of naphthalimide fluorophore as donor with  $\text{FeN}_6$  SCO chromophore as switchable acceptor.

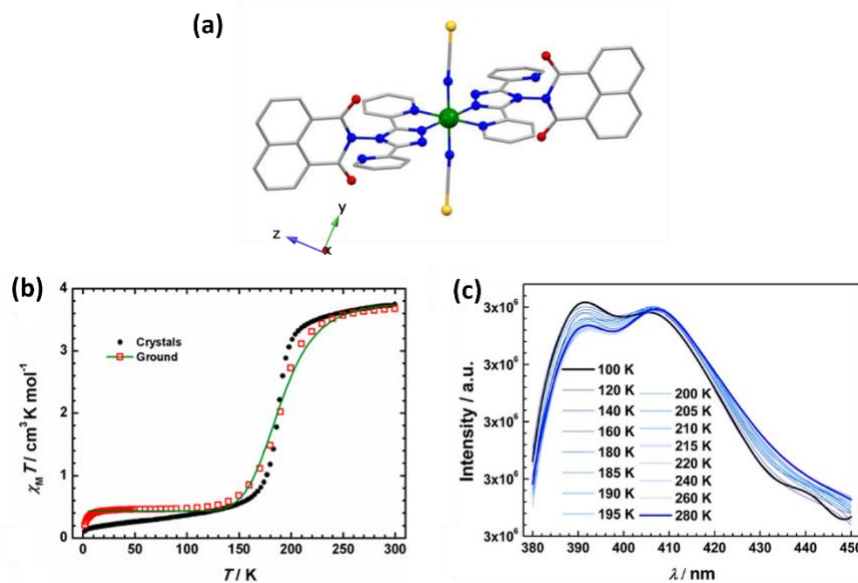


**Fig. 13.** (a) Simplified crystal structure of complex **18**, hydrogen atoms are omitted for clarity (Fe: green, C: gray, O: red, N: blue, S: yellow). (b)  $\chi T$  vs. T plot from solid-state variable temperature magnetic measurement on fresh crystals of **18** (black) and grounded powder samples of **18** (red); (c) Variable temperature fluorescence emission spectra for the complex **18**. Adapted with permission from Ref. [73].

Single Crystal X-ray Diffraction studies were performed at 100 K and 300 K for the complex **18**. The system crystallizes in the Monoclinic  $P2_1/c$  space group at both temperatures. The Fe(II) centers reside in a hexa-coordination environment with four equatorial N atoms coming from two **L12** units and two N atoms from two coordinating NCS<sup>-</sup> ions in a trans fashion (Fig. 13a). At 100 K, the average Fe-N bond distances fall in the range of 1.941(5)-2.004(5) Å, suggesting the presence of Fe(II) LS state. The average Fe-N bond distances increase by 0.186 Å from 100 K to 300 K, suggesting switching from LS to HS state. This also accords with a large change in

octahedral distortion index  $|\Delta\Sigma|$  of 21.67° while going from 100 K to 300 K. To inquire into the magnetic properties of the complex **18**, solid-state magnetic susceptibility measurements were performed **18** to get  $\chi T$  vs. T plot. At 300 K, the  $\chi T$  value of  $3.74 \text{ cm}^3 \text{ mol}^{-1} \text{ K}$  is consistent with one Fe(II) HS state ( $S=2$ ) (Fig. 13b). Upon decreasing the temperature, the  $\chi T$  value slowly decreases up to 200 K, following a steep drop to reach the  $\chi T$  value of  $0.11 \text{ cm}^3 \text{ K mol}^{-1}$  at 2 K. To study the synergy between the spin state switching and fluorescence properties, variable temperature fluorescence emission spectra for both complex **18** and ligand **L12** were recorded with the excitation wavelength of 310 nm. For the free ligand, the 394 and 412 nm fluorescence peaks show brighter emission with temperatures from 80 K to 300 K coming from the singlet to triplet state and reabsorption with delayed fluorescence. For complex **18**, two distinct emission bands at 390 and 408 nm were found (Fig. 13c). The emission band at 390 K was found to be SCO independent with increasing the temperature, whereas the integrated intensity at 408 nm with variable temperature shows a sigmoidal nature which can be attributed to the effect of SCO phenomena. This complex **18** has a potential to be applied in ratiometric fluorescence thermosensing based on SCO considering luminescence intensity ratio (LIR), where  $I_{390}$  (T) can serve as a reference while  $I_{408}$  (T) is the SCO response. As the temperature increases, Fe(II) LS centers (strong quencher) get replaced with Fe(II) HS centers (weak quencher), changing the spin-state equilibrium as well as the LIR of complex **18**, which exhibits a sharp increase. . The  $S_r$  (relative sensitivity) calculated from the fluorescence intensity yielded a working temperature range of the sensor from 155 K to 195 K. The maximum sensitivity is found at the HS fraction of 0.28 around 174 K, below the  $T_{1/2}$  of 189 K.

One important aspect of finding the correlation between the fluorescence and SCO properties is the efficient overlap between the emission and absorption band of the fluorophore and the SCO

material, respectively. To verify this, temperature-dependent solid-state UV-Vis absorption spectra were measured for complex **18**, and a broad absorption band around 510 nm is observed at 100 K due to metal-to-ligand charge transfer (MLCT) transition from Fe(II) LS ion associating with visible color changing from pink (RT) to dark red (78 K). The emission band at 408 nm stays close to the MLCT band thus having much more influence from SCO compared to the emission band at 390 nm, far from the MLCT band thus being SCO insensitive. Overall, Complex **18** represented the first of its kind SCO device by ratiometric fluorescence sensing method with high sensitivity.

### Dinuclear Complexes:

In 2011, Garcia and co-workers reported the synergic correlation between SCO and luminescence in a dinuclear iron(II) complex  $[\text{Fe}_2(\text{L13})_5(\text{NCS})_4] \cdot 4\text{MeOH}$  (**19**) (**L13** = *N*-salicylidene-4-amino-1,2,4-triazole; (**Scheme 1**) [74]. The iron(II) complex was prepared by the reaction of  $\text{Fe}(\text{NCS})_2$  and the ligand **L13** in methanol, followed by slow evaporation of the reaction mixture to obtain **19** as bright-yellow crystals. Single crystal X-ray structure analyses at 100 and 200 K revealed that **19** crystallizes in monoclinic space group  $C2/c$  at both temperatures. In the dinuclear complex, each iron is coordinated with two *cis*- $\text{NCS}^-$  and the **L13** is acting as both a monodentate and bidentate bridging ligands. At 240 K, the average Fe-N bond distance is 2.180(3) Å, which lies in the range expected for a HS Fe(II) in a  $\text{N}_6$  coordination environment. The average Fe-N bond distance reduces to 1.983(2) Å at 100 K, suggesting a LS Fe(II) state in **19**. Crystallographic studies indicated a thermo-induced SCO in **19**, which was further supported by DSC and Mössbauer studies. DSC measurement of **19** shows first-order phase transition with  $T_{\max} = 155(1)$  K (Fig. 14a). Variable temperature Mössbauer spectra of **19** displayed two quadrupolar

doublets corresponding to almost LS state at 77 K ( $A^{\text{LS}} = 94(2)\%$ ) and HS ( $A^{\text{HS}} = 6(2)\%$ ), while only one quadrupolar doublet corresponding to HS Fe(II) ( $A^{\text{HS}} = 100\%$ ) was observed at 300 K.

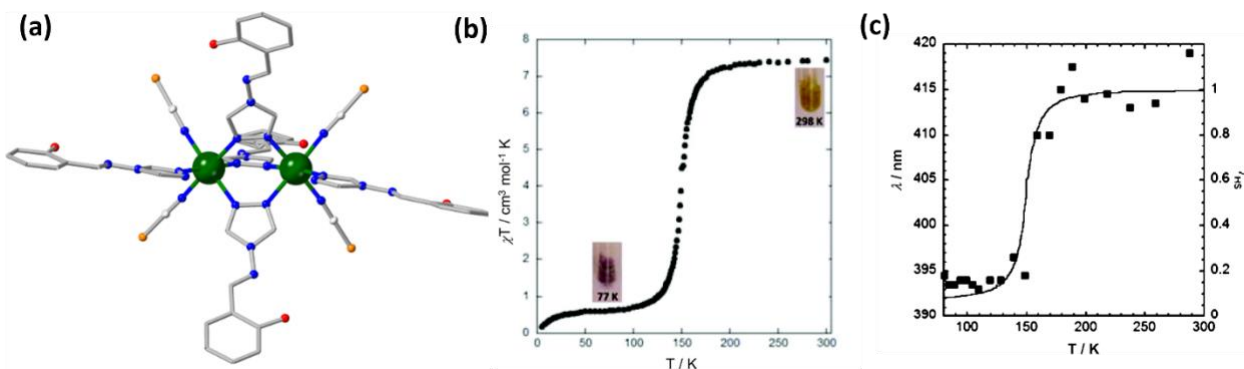


**Fig. 14.** (a) Simplified crystal structure of complex  $[\text{Fe}_2(\text{L13})_5(\text{NCS})_4] \cdot 4\text{MeOH}$  (**19**) at 200 K, for clarity hydrogen atoms are omitted (Fe: green, C: gray, N: blue, O: red, S: orange). (b)  $\chi T$  vs T plot for **19**. Thermochromic properties are shown in the photographs of **19**. (c) Variable temperature  $\lambda_{\text{max}}$  enol\* in the emission spectrum of **19** (■), which follows  $\gamma_{\text{HS}}$  derived from the magnetic data (solid line). Adapted with permission from Ref. [74].

Temperature dependency of the magnetic properties of **19** was studied by variable temperature magnetic susceptibility measurements in between 300 – 5 K. The measured  $\chi T$  value at 300 K is  $7.46 \text{ cm}^3 \text{ mol}^{-1} \text{ K}$ , confirming the HS state of two Fe(II) centers in **19** with significant orbital contributions. Upon cooling down, the  $\chi T$  vs T plot displays a sharp decrease in the temperature range of 161 – 138 K with a minimum value of  $0.60 \text{ cm}^3 \text{ mol}^{-1} \text{ K}$ , corresponding LS state of two Fe(II) centers with a residual HS Fe(II) state in **19**. Overall results confirm a SCO from [HS–HS] to [LS–LS] pairs at  $T_{1/2} = 150 \text{ K}$  without an intermediate [LS–HS] phase. (Fig. 14b)

Variable temperature PL measurements revealed that complex **19** exhibits an emission maximum centered at 350 nm, corresponding to radiative deexcitation of the excited enol\* form at 80 K, which shifted to 414 nm with a bathochromic shift of  $\sim 20 \text{ nm}$  along with the appearance

of another band at 510 nm (radiative relaxation of the excited *cis*-keto\* form upon increasing the temperature to 300 K). In contrast, emission spectra of the ligand **L13** show the above-mentioned two bands at 444 and 526 nm in the temperature range of 80 – 289 K, describing a significant effect of the coordination environment around the iron centers with the ligands. Moreover, the temperature dependence of the shift of enol\* band ( $\lambda_{\max}$  enol\*) as  $\lambda_{\max}$  enol\* vs T shows a sharp jump of 20 nm in between 135 and 179 K (from ~395 nm below 150 K to 415 nm above 200 K). Similar temperature dependence of the HS molar fraction ( $\gamma_{HS}$ ) derived from the magnetic measurements of **19**, confirming the synergic relation between SCO and luminescence in **19** (Fig. 14c).

In 2016, Tao and co-workers reported an isostructural dinuclear complex using the derivative of the ligand **L13** without an OH substituent group to avoid keto-to-enol transition [75]. The iron complex  $[Fe_2(L14)_5(NCS)_4] \cdot 4MeOH$  (**20**) (**L14** = phenyl-N-(4H-1,2,4-triazol-4-yl)methanimine) (**Scheme 1**) was synthesized by the reaction between  $FeCl_2$ , ammonium thiocyanate, and the ligand **L14** in methanol. Slow evaporation of the complex solution gave bright yellow crystals of **20** in good yield. Variable temperature single-crystal X-ray structure analyses at 230, 100, and 85 K revealed that **20** crystallizes in triclinic space group  $P\bar{1}$  in all temperatures. The molecular motif of the neutral complex **20** is isostructural with the complex **19**. In complex **20**, the average Fe-N bond distances are 2.193(3) and 2.043 Å at 230 and 85 K, respectively, indicating the presence of HS and LS Fe(II) centers in **20** at these temperatures respectively. Temperature dependence of the magnetic susceptibility showed a similar SCO behavior as observed by Garcia and co-workers for complex **19**. In contrast, hidden three-step transitions were observed in **20** at 87/90 K ( $T_{1/2}(1)\downarrow/T_{1/2}(1)\uparrow$ ), 125/135 ( $T_{1/2}(2)\downarrow/T_{1/2}(2)\uparrow$ ) and 154/156 K ( $T_{1/2}(3)\downarrow/T_{1/2}(3)\uparrow$ ) in cooling/heating mode with a hysteresis loop of 3, 10, and 2 K respectively.

Temperature-dependent PL measurements of the complex **20** and ligand **L14** were carried out in the temperature range of 300 – 80 K. PL spectra at room temperature revealed emission maxima centered at 515 and 466 nm for **20** and **L14** respectively, indicating the effect of metal coordination on the ligand system. Upon increasing the temperature from 80 to 300 K, PL spectra of **20** displayed a blue shift of 18 nm in the emission maxima. The emission intensity varies in a wave-like nature with three maxima between 80 and 95 K, 125 and 135 K, and 145 and 190 K, respectively. These changes are around three-step SCO temperature, suggesting a synergic correlation between SCO and luminescence in **20**.

In 2017, Aromí, and co-workers reported SCO in a luminescent dinuclear iron complex coordinated with a bis(pyrazolylpyridyl) ligand that contains a central photochromic dithienylethene spacer [76]. The iron complex  $[\text{Fe}_2(\text{L15})_3](\text{ClO}_4)_4$  (**21**) (**L15** = 1,2-bis(5-(2-(pyrazol-3-yl)-pyridin-5-yl)-2-methyl-thiophen-3-yl)-cyclopentene; (**Scheme 1**) was prepared as orange crystals by the reaction between  $\text{Fe}(\text{ClO}_4)_2$  and **L15** in either methanol or acetone and successive diffusion of toluene into the reaction mixture. Crystallographic studies at 100 K revealed that each Fe(II) centers in the cationic  $[\text{Fe}_2(\text{L15})_3]^{4+}$  unit coordinated with pyrazolylpyridyl unit coming from the three **L15** ligands which also bridged by other iron centers, making a triple-stranded helicate. The average Fe–N distances are 1.97(2) and 1.97(3) Å, indicating the presence of LS iron(II) in **21** at 100 K (Fig. 15a).

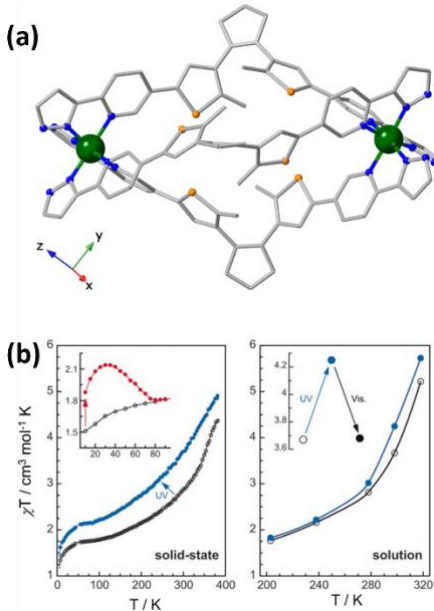


**Fig. 15.** (a) Simplified Perspective view of complex cation in  $[Fe_2(L15)_3](ClO_4)_4$  (**21**) at 100 K. Hydrogen atoms and counteranions are omitted for clarity (Fe: green, C: gray, N: blue, S: orange). (b) Plot of magnetic susceptibility product with temperature for complex  $[Fe_2(L15)_3](ClO_4)_4$  (**21**) in the solid-state, before (hollow black dots) and after UV light irradiation (solid blue dots,  $\lambda < 425$  nm). Inset: Partial LIESST effect upon irradiation at 10 K with red light ( $800\text{ nm} < \lambda < 900\text{ nm}$ , solid red dots). Adapted with permission from Ref. [76].

Temperature dependency of magnetic susceptibility measurements revealed that **21** exhibits an incomplete and reversible SCO where the measured  $\chi T$  value of  $4.41\text{ cm}^3\text{ mol}^{-1}\text{ K}$  at 385 K gradually reduced to  $1.7\text{ cm}^3\text{ mol}^{-1}\text{ K}$  below 90 K. Interestingly, the magnetic properties change significantly upon *ex-situ* irradiation with UV light at room temperature where a noteworthy increase in the HS fraction with lowering of  $T_{1/2}$  was observed. Although  $\chi T$  vs. T plot remains the same upon irradiation with visible light, confirming the irreversible effect of light on magnetic properties in **21**. (Fig. 15b) Moreover, photomagnetic measurements of **21** under red ( $\lambda = 800$ –900 nm), green ( $\lambda = 500$ –650 nm), or white ( $\lambda = 400$ –900 nm) lights at 10 K displayed a partial

photo-conversion between the LS to the photo-excited metastable HS state ( $\sim$ 7%) with a  $T_{LIESST}$  value of *ca.* 80 K. Although complex **21** exhibited reversible photo-switchable PL properties in solution due to photo-conversation of diarylethene ligand, no synergic relation between SCO and luminescence was observed (Fig. 15b).

In 2020, Piguet and co-workers reported a series of dinuclear triple-stranded helicates  $[\text{LnFe}(\mathbf{L16x})_3](\text{CF}_3\text{SO}_3)_5$  (**22**) ( $\text{Ln} = \text{La(III), Eu(III)}$  and **L16x = L16a – L16b**) (Scheme 1) [77], which were prepared by the stoichiometric reaction between the ligand (**L16a – L16b**),  $\text{Ln}(\text{CF}_3\text{SO}_3)_3$  ( $\text{Ln} = \text{La(III), Eu(III)}$ ) and  $\text{Fe}(\text{CF}_3\text{SO}_3)_2$  in DCM. A suitable single-crystal for X-ray diffraction analyses was obtained by diffusion of diethyl ether into the reaction mixture. Single crystal X-ray analyses revealed a Fe(II) center in the cationic  $[\text{LnFe}(\mathbf{L16x})_3]^{5+}$  unit coordinated with bidentate di-imine unit coming from the two **L16x** ligands which also bridged other Ln center, making a  $C_3$ -symmetrical dinuclear triple-stranded helicate. The average Fe-N bond distances are 2.14 and 1.95 $\text{\AA}$  for  $[\text{LnFe}(\mathbf{L16x})_3]^{5+}$  ( $\text{Ln} = \text{La(III)}$ ) for **L16a** and **L16b**, respectively. Magnetic studies revealed that  $[\text{LnFe}(\mathbf{L16b})_3]^{5+}$  ( $\text{Ln} = \text{La(III)}$ ) complex shows an incomplete SCO between 100 K and room temperature, while  $[\text{LnFe}(\mathbf{L16a})_3]^{5+}$  ( $\text{Ln} = \text{La(III)}$ ) complex remains in HS state in the whole measurement range (Fig. 16a).

Variable temperature PL measurements were carried out on SCO  $[\text{EuFe}(\mathbf{L16b})_3]^{5+}$  complex under irradiation with 355 nm, where the intensity of the Eu-based  $^5\text{D}_0 \rightarrow ^7\text{F}_J$  ( $J = 0–6$ ) transition increased unusually upon increasing the temperature in the range of 200 – 300 K. While HS  $\text{EuFe}(\mathbf{L16b})_3]^{5+}$  complex displayed a monotonous decrease in intensity with temperature. Such a feature can be described by the replacement of strong Fe(II) LS quenchers by weaker accepting Fe(II) HS centers with the increasing temperature near the SCO region, indicating the synergic correlation between SCO and luminescence in  $[\text{EuFe}(\mathbf{L16b})_3]^{5+}$  complex (Fig. 16b).

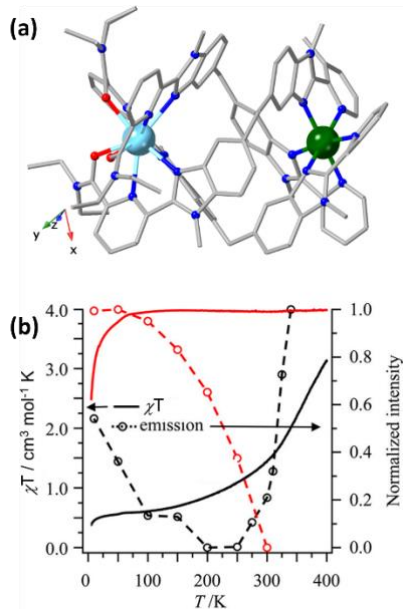


**Fig. 16.** (a) Simplified crystal structure of complex cation  $[\text{EuFe}(\text{L16b})_3]^{5+}$  at 180 K, for clarity hydrogen atoms and counteranions are omitted (Eu: Cyan, Fe: green, C: gray, N: blue, O: red); (b) Solid-state  $\chi T$  (left axis, solid lines) and normalized emission (right axis, circles and dashed lines) for HS  $[\text{LnFe}(\text{L16a})_3](\text{CF}_3\text{SO}_3)_5$  (red) and SCO  $[\text{LnFe}(\text{L16b})_3](\text{CF}_3\text{SO}_3)_5$  (black) (Ln used for magnetism: La(III), Ln used for luminescence: Eu(III)). Adapted with permission from Ref. [77].

In 2023, Piguet and co-workers again worked on a similar system, replacing terminal pyridine moiety in **L16x** by hydrolysis of the sensitive pyrimidine group associated with weaker Fe-N interactions resulting from the complexation [78]. The transition temperature for the complex  $[\text{EuFe}(\text{L16c})_3]^{5+}$  (**22c**) becomes 317 K to allow more conversion from Fe(II) LS state to the Fe(II) HS state within the accessible temperature range. Moreover, the reduced quenching of Eu ( ${}^5\text{D}_0$ ) based emission band due to the decrease in Fe(II) MLCT absorption bands intensity can help presenting these systems as lanthanide-based emission detection of SCO process in solution.

### Trinuclear Complexes:

Ruben and co-workers incorporated alkynyl coordinated Pt(II)-terpy unit with ligand (**L-Pt**) and prepared a trinuclear (Pt<sub>2</sub>Fe) complex  $[\text{Fe}(\text{L-Pt})_2]_2(\text{BF}_4)_2$  (**23**) [79], which was crystallized in an

inseparable mixture of two different types of crystals (Fig. 17). Both crystals crystallize in different space groups, differ in the packing as well as number of solvent molecules: **23**·3.5CH<sub>2</sub>Cl<sub>2</sub> in *P* $\bar{1}$  and **23**·10CH<sub>2</sub>Cl<sub>2</sub> in *C*2/c. Complex **23**·10CH<sub>2</sub>Cl<sub>2</sub> shows SCO with a T<sub>1/2</sub> of 268 K, while complex **23**·3.5CH<sub>2</sub>Cl<sub>2</sub> remains in the HS state. Complex **23**·10CH<sub>2</sub>Cl<sub>2</sub> exhibited luminescence features where the emission spectral shape, intensity, and lifetime are greatly influenced by the temperature; although these did not exhibit any synergistic correlation with the temperature-dependent magnetic properties. Moreover, the luminescence properties of **23** and **L-Pt** are very similar, suggesting no synergic cooperation between SCO and luminescence. Data for correlating magnetic and luminescence properties are shown in Table 1.

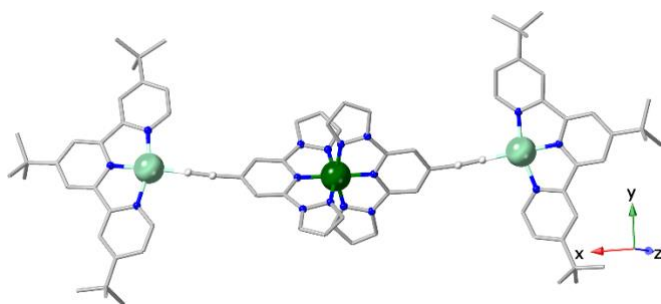


**Fig. 17.** Simplified crystal structure of complex cation in [Fe(**L-Pt**)<sub>2</sub>]<sub>2</sub>(BF<sub>4</sub>)<sub>2</sub> (**23**) at 180 K, for clarity hydrogen atoms and counteranions are omitted (Pt: cyan, Fe: green, C: gray, N: blue). Adapted with permission from Ref. [79].

**Table 1.** Correlation between the magnetic and luminescent properties of the complexes discussed in this review.

Complex	Complex Fluorescen- ce		Ligand Fluoresce- nce	Coordin- ation type	SCO behavior	Direct synergy between SCO and Lumines- cence Present	Refer- ence	
	$\lambda_{\text{ex}}$	$\lambda_{\text{em}}$	$\lambda_{\text{ex}}$	$\lambda_{\text{em}}$				
[Fe( <b>L1</b> ) <sub>2</sub> ](BF <sub>4</sub> ) <sub>2</sub> ( <b>1</b> )	-	359 nm	-	493 nm	Mononu- clear	Hystereti- c SCO with $T_{1/2}$ = 259 K.	Yes	[61]
[Fe( <b>L2</b> ) <sub>2</sub> (NCS) <sub>2</sub> ] ( <b>2</b> )	380 nm	513 nm	380 nm	516 nm	Mononu- clear	Abrupt SCO with $T_{1/2}$ = 267 K with photoma- gnetic effect at low temperat- ure.	Yes	[63]
[Fe( <b>L3</b> ) <sub>2</sub> ](ClO <sub>4</sub> ) <sub>2</sub> ·3CH <sub>3</sub> OH·CH <sub>2</sub> Cl <sub>2</sub> ·0.8H <sub>2</sub> O ( <b>3</b> )	-	-	-	560 nm	Mononu- clear	Reversib- le three- step SCO. 40 K hysteresi- s loop with sharp transition in <b>3-d</b> .	Yes	[64]
[Fe( <b>L4</b> ) <sub>6</sub> ](tcnsme) <sub>2</sub> 4CH <sub>3</sub> CN ( <b>5</b> )	-	600 nm	-	412 nm	Mononu- clear	Gradual SCO with $T_{1/2}= 114$ K.	Yes	[65]

[Fe( <b>L5</b> ) <sub>2</sub> ](ClO <sub>4</sub> ) ( <b>6</b> )	375 nm	420 nm	-	432 nm	Mononuclear	Gradual and incomplete SCO with T <sub>1/2</sub> = 173 K for <b>6-d</b> .	No	[66]
[Fe( <b>L6</b> ) <sub>2</sub> (SeCN) <sub>2</sub> ]·4DMF ( <b>7</b> )	365 nm	483 nm	365 nm	484 nm	Mononuclear	Gradual SCO with T <sub>1/2</sub> = 295 K	Yes	[67]
[Fe( <b>L6</b> ) <sub>2</sub> (NCS) <sub>2</sub> ]·4MeCN ( <b>8</b> )	365 nm	441 nm	365 nm	478 nm	Mononuclear	Complete abrupt transition with T <sub>1/2</sub> = 129 K.	Yes	[68]
[Fe( <b>L6</b> ) <sub>2</sub> (NCS) <sub>2</sub> ]·2MeCN·2CH <sub>2</sub> Cl <sub>2</sub> ( <b>9</b> )	365 nm	457 nm	365 nm	478 nm	Mononuclear	Complete abrupt transition with T <sub>1/2</sub> = 203 K.	Yes	[68]
[Fe( <b>L7</b> ) <sub>2</sub> ](ClO <sub>4</sub> ) <sub>2</sub> ·5.75CH <sub>2</sub> Cl <sub>2</sub> ( <b>10</b> )	365 nm	473 nm	365 nm	484 nm	Mononuclear	Complete one-step SCO with T <sub>1/2</sub> = 375 K.	No	[69]
[Fe( <b>L7</b> ) <sub>2</sub> ](BF <sub>4</sub> ) <sub>2</sub> ·CH <sub>2</sub> Cl <sub>2</sub> ·3CH <sub>3</sub> OH ( <b>12</b> )	365 nm	457 nm	365 nm	484 nm	Mononuclear	Complete one-step SCO with T <sub>1/2</sub> = 248 K.	No	[69]
[Fe( <b>L8</b> ) <sub>2</sub> ](ClO <sub>4</sub> ) <sub>2</sub> ( <b>13</b> )	320 nm	-	387 nm	485 nm	Mononuclear	Gradual SCO.	Yes	[70]
[Fe( <b>L9</b> ) <sub>2</sub> ](ClO <sub>4</sub> ) <sub>2</sub> ·2.63CH <sub>2</sub> Cl <sub>2</sub> ( <b>14</b> )	395 nm	475 nm	467 nm	550 nm	Mononuclear	Gradual SCO.	No	[70]

$\{[\text{Co}(\text{HL10})_2][\text{Co}(\text{HL10})(\text{L10})]\} (\text{ClO}_4)_3 \cdot 9\text{H}_2\text{O}$ ( <b>15</b> )	295 nm	370 nm	-	367 nm	Mononuclear	Gradual SCO.	No	[71]
$[\text{Co}(\text{L10})_2] \cdot 5\text{H}_2\text{O}$ ( <b>16</b> )	295 nm	370 nm	-	367 nm	Mononuclear	Gradual SCO.	No	[71]
$[\text{Fe}(\text{L11})(\text{NCBH}_3)_2] \cdot 1.5\text{CH}_3\text{OH}$ ( <b>17</b> )	300 nm	359 nm	-	-	Mononuclear	Abrupt and complete SCO with $T_{1/2} = 207\text{ K}$ .	Yes	[72]
$[\text{Fe}(\text{L12})_2(\text{NCS})_2 \cdot 2\text{DMF}$ ( <b>18</b> )	310 nm	390, 408 nm	310 nm	394, 412 nm	Mononuclear	Abrupt one-step SCO with $T_{1/2} = 189\text{ K}$ .	Yes	[73]
$[\text{Fe}_2(\text{L13})_5(\text{NCS})_4] \cdot 4\text{MeOH}$ ( <b>19</b> )	350 nm	394 nm	350 nm	444, 526 nm	Dinuclear	Incomplete abrupt SCO with $T_{1/2} = 150\text{ K}$	Yes	[74]
$[\text{Fe}_2(\text{L14})_5(\text{NCS})_4] \cdot 4\text{MeOH}$ ( <b>20</b> )	374 nm	515 nm	-	466 nm	Dinuclear	Three-step SCO with hysteresis width of 3,10 and 2 K.	Yes	[75]
$[\text{Fe}_2(\text{L15})_3](\text{ClO}_4)_4$ ( <b>21</b> )	290 nm	440 nm	-	-	Dinuclear	Gradual and incomplete SCO.	No	[76]
$[\text{LnFe}(\text{L16b})_3](\text{CF}_3\text{SO}_3)_5$ ( <b>22</b> ) ( $\text{Ln} = \text{La(III)}$ and $\text{L16x} = \text{L16b}$ )	355 nm	-	-	-	Dinuclear	Incomplete SCO.	Yes	[77]
$[\text{Fe}(\text{L-Pt})_2]_2(\text{BF}_4)_2$ ( <b>23</b> )	323 nm	515 nm	337 nm	516 nm	Trinuclear	Reversible SCO with $T_{1/2} = 268\text{ K}$ for	No	[79]

**23·10CH<sub>2</sub>Cl<sub>2</sub>.**

[Fe( <b>L17</b> )(bipy)] <sub>n</sub> ( <b>24</b> )	337 nm	550, 673 nm	1D	Reversible complete SCO with thermal hysteresis; $T_{1/2}\uparrow = 380 - 371$ K and $T_{1/2}\downarrow = 323$ K	Yes	[80]	
Dinuclear $\{(\mu\text{-bipy})[\text{Fe}(\text{L17})(\text{MeOH})]_2\} \cdot 2\text{MeOH}$	337 nm	550, 686 nm	Dinuclear	Not observed	No	[80]	
{[Fe( <b>L18</b> )]( <b>L19</b> ) <sub>0.5</sub> ·3CH <sub>3</sub> OH} <sub>n</sub> ( <b>25</b> ·3CH <sub>3</sub> OH)	-	-	365 nm	462 nm	2D	Reversible complete SCO with thermal hysteresis of 25 K; $T_{1/2}\downarrow = 202$ K and $T_{1/2}\uparrow = 227$ K	[81]
{[Fe( <b>L18</b> )]( <b>L19</b> ) <sub>0.5</sub> ·xCH <sub>3</sub> OH} <sub>n</sub> ( <b>25</b> ·xCH <sub>3</sub> OH)	-	-	365 nm	462 nm	2D	Reversible complete SCO with thermal hysteresis of 5 K; $T_{1/2}\downarrow = 205$ K and $T_{1/2}\uparrow = 210$ K	[81]

$\{[\text{Fe}(\text{L18})(\text{L19})_{0.5}\}_n$ <b>(25)</b>	365 nm	460 nm	365 nm	462 nm	2D	Gradual SCO with $T_{1/2}$ = 205 K	Yes	[81]
$\{[\text{Fe}(\text{L20})_2(\text{NCSe})_2]\cdot 6\text{M}$ $\text{eOH}\cdot 14\text{H}_2\text{O}\}_n$ <b>(26)</b>	395 nm	524, 570 nm	-	565 nm	2D	Gradual SCO of $T_{1/2}$ = 150 K and photoma gnetic effect $T_{\text{LIEST}} =$ 80 K.	Yes	[82]
$[\text{Fe}^{\text{II}}\text{21}(\text{L19})_{0.5}]$ <b>(27)</b>	360 nm	442 nm	360 nm	472 nm	2D	Incomple te gradual SCO	Yes	[84]
$[(\text{Fe}^{\text{II}}_3\text{L21}_3(\text{L19})_{1.5})]$ <b>(28)</b>	360 nm	464 nm	360 nm	472 nm	2D	No SCO, No mostly LS		[84]
$[\text{Fe}(\text{L22})_2\text{Pt}(\text{CN})_4]$ <b>(29)</b>	380 nm	572 nm	380 nm	534 nm	2D	Reversib le complete Spin transition with thermal hysteresi s of 21 K: $T_{1/2}\downarrow$ = 205 K and $T_{1/2}\uparrow$ = 226 K	Yes	[85]
$[\text{Fe}(\text{L22})_2\text{Pt}(\text{CN})_4]\cdot x\text{H}_2$ $\text{O}$ <b>(29·xH<sub>2</sub>O)</b>	380 nm	584 nm	380 nm	534 nm	2D	Three step spin transition	Yes	[85]
$[\text{Fe}(\text{L22})_2\text{Pt}(\text{CN})_4]\cdot x\text{Solv}$ <b>(29·xSolv)</b>	380 nm	510 nm	380 nm	534 nm	2D	Two step spin transition with thermal	Yes	[85]

$\{\text{Fe}^{\text{II}}(\text{L23})_2(\text{SCN})_2 \cdot \text{CHC}$ $\text{l}_3 \cdot 4\text{CH}_3\text{OH}\}_{\text{n}}$ ( <b>30</b> )	325 nm	-	-	-	2D	hysteresis. $T_{1/2}\downarrow = 119, 190$ $K$ and $T_{1/2}\uparrow = 129, 210$ $K$	Incomplete and gradual SCO with $T_{1/2} = 110$ K.	No	[86]
$\{[\text{Fe}^{\text{II}}(\text{L23})_2(\text{SeCN})_2] \cdot \text{C}$ $\text{H}_2\text{Cl}_2 \cdot 4\text{CH}_3\text{OH}\}_{\text{n}}$ ( <b>31</b> )	330 nm	417, 450. 467, 528 nm	378 nm	487 - 497 ,	2D	One step incomplete and gradual SCO with $T_{1/2} = 144$ K.	Yes	[86]	
$\{\text{Fe}(\text{L24})[\text{Au}(\text{CN})_2]\} @$ pyr ( <b>32@pyr</b> )	332 nm	392, 478 nm	-	-	3D	Complete three stepped SCO with $T_{1/2} = 190$ K. and showing photomagnetic effect with $T_{\text{LIEST}} = 50$ K.	Yes	[87]	
$\{\text{Zn}(\text{L24})[\text{Au}(\text{CN})_2]\} @$ pyr ( <b>33@pyr</b> )	332 nm	439, 484 nm	-	-	3D	-	No	[87]	
$\{\text{Fe}^{\text{II}}(\text{L25})[\text{Ag}^{\text{I}}(\text{CN})_2]_2\}$ ( <b>34</b> )	345, 262 nm	350- 490 nm			3D	One step SCO with thermal hysteresis of 6 K and $T_{1/2}\downarrow = 222$ K	Yes	[88]	

							and $T_{1/2}\uparrow$ = 228 K	
$\{\text{Fe}^{\text{II}}(\textbf{L25})[\text{Au}^{\text{I}}(\text{CN})_2]_2\}$ <b>(35)</b>	-	-	-	-	3D	Two step SCO with thermal hysteresi s of 10 K & 20 K and $T_{1/2}(1)\downarrow/$ $T_{1/2}(1)\uparrow$ =	No	[88]
$\{\text{Zn}^{\text{II}}(\textbf{L25})[\text{Au}^{\text{I}}(\text{CN})_2]_2\}$ <b>(34/35-Zn)</b>	-	-	-	-	3D	-	No	[88]
$\{\text{Fe}^{\text{II}}(\textbf{L26})[\text{Ag}^{\text{I}}(\text{CN})_2]_2\}$ pyrene ( <b>36@pyr</b> )	345	-	-	-	3D	Incomple te gradual SCO with $T_{1/2}$ $\approx 100$ K	Yes	[88]
$\{\text{Fe}^{\text{II}}(\textbf{L26})[\text{Au}^{\text{I}}(\text{CN})_2]_2\}$ pyrene ( <b>37@pyr</b> )	-	-	-	-	3D	Incomple te two step SCO with thermal hysteresi s of 4 K & 7 K and $T_{1/2}(1)\downarrow/$ $T_{1/2}(1)\uparrow$ =	No	[88]

							156/160 K and $T_{1/2}(2)\downarrow/$ $T_{1/2}(2)\uparrow$ =		
[Fe( <b>L19</b> )Ag(CN) <sub>2</sub> ]ClO <sub>4</sub> ·5MeOH·14H <sub>2</sub> O·CH <sub>2</sub> Cl · <sub>2</sub> ( <b>38</b> )	355 nm	534 nm	-	462 -	3D	Complete spin transition with $T_{1/2} = 230$ K.	Yes	[89]	
[Fe( <b>L19</b> )Ag(CN) <sub>2</sub> ]ClO <sub>4</sub> (Desolvated <b>38</b> )	-	-	-	-	3D	No SCO, remained HS	No	[89]	
[Fe( <b>L19</b> )Au(CN) <sub>2</sub> ]ClO <sub>4</sub> ·14MeOH·18H <sub>2</sub> O·CH <sub>2</sub> Cl <sub>2</sub> ( <b>39</b> )	355 nm	-	-	462 -	3D	Abrupt and incomplete spin transition with $T_{1/2} = 245$ K.	Yes	[89]	
[Fe( <b>L19</b> )Au(CN) <sub>2</sub> ]ClO <sub>4</sub> (Desolvated <b>39</b> )	355 nm	-	-	462 -	3D	Gradual and incomplete SCO	Yes	[89]	
[{Fe( <b>L27</b> )[Ag(CN) <sub>2</sub> ] <sub>2</sub> } ·2EtOH] <sub>n</sub> ( <b>40</b> )	398 nm	450, 480 nm	398 nm	471 nm	3D	Incomplete SCO with $T_{1/2} = 161$ K and reversible photomagnetic effect with $T_{LIEST} = 75$ K.	Yes	[90]	

Tcnsme = 1,1,3,3-tetracyano-2-thiomethylpropenide, bipy = 4,4'-bipyridine.

## 2.2 Luminescent SCO in 1D Systems

Weber and co-workers reported a synergic tie-up between the luminescence and SCO in 1D iron(II) Coordination Polymer (CP) [80]. The CP  $[\text{Fe}(\text{L17})(\text{bipy})]_n$  (**24**) (bipy = 4,4'-bipyridine) was prepared as plate-like crystals from the reaction between  $[\text{Fe}(\text{L17})(\text{MeOH})_2]$  and 10 equivalents of bipy in methanol, while a dinuclear  $\{(\mu\text{-bipy})[\text{Fe}(\text{L17})(\text{MeOH})_2]\} \cdot 2\text{MeOH}$  was obtained as block-shaped crystals using 0.5 equivalents of bipy (Fig.18a). Single crystal X-ray diffraction analysis of **24** at 123 K divulged that each Fe(II) center lies in an octahedral  $\text{N}_3\text{O}_3$  surrounding and coordinates with two of the nitrogen and two of the oxygen donor atoms coming from ligand **L17**, one oxygen atom from a methanol molecule and bridged by a bipy ligand. The average Fe-N, Fe-O bond distances, and the characteristic O-Fe-O angle, suggested the HS state of the Fe(II) metal center at this temperature. Although single-crystal X-ray diffraction analysis was not obtained after many attempts, the polymeric nature and the structural formula of **24** were corroborated by the elemental analysis, mass spectrometry, powder X-ray diffraction, and scanning electron microscopy analysis.

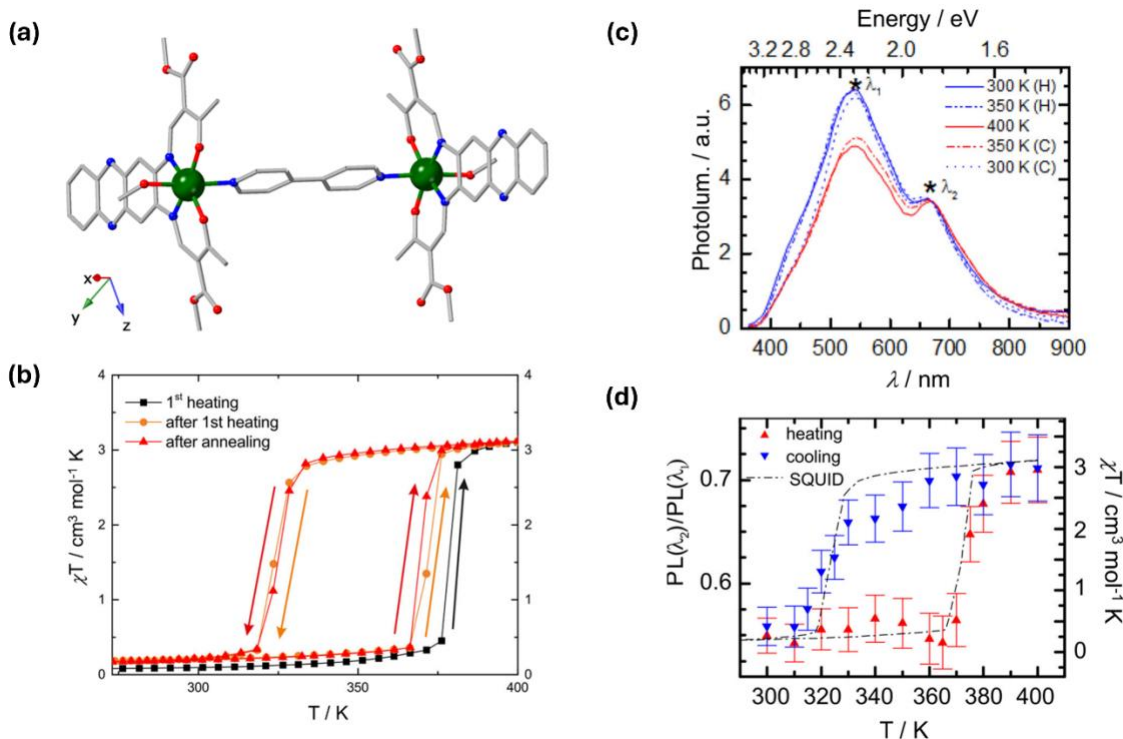


**Fig. 18.** (a) Representative view of the dinuclear complex **24** at 123 K. Hydrogen atoms were excluded for clarity (Fe: green, C: gray, O: red, N: blue). Reproduced with permission from Ref [80]. (b)  $\chi T$  vs T plot for **24** between 275 and 400 K. (c) Temperature-dependent emission spectra of **24** with  $\lambda_{\text{ex}} = 337 \text{ nm}$  upon heating (H) and cooling (C) processes. The stars defined the peaks at  $\lambda_1 = 550 \text{ nm}$ ,  $\lambda_2 = 673 \text{ nm}$ . (d) Comparison of photoluminescence ratio at  $\lambda_2 = 673 \text{ nm}$  and  $\lambda_1 = 550 \text{ nm}$  with  $\chi T$  value of **24**. Adapted with permission from Ref. [80].

The magnetic measurements as  $\chi T$  vs T revealed that the complex **24** remained HS in the whole measured temperature range of 400 - 50 K, which was expected for one Fe(II) center remain in a  $\text{FeN}_3\text{O}_3$  surrounding with weak ligand field strength. In contrast, **24** exhibited LS to HS transition with  $T_{1/2\uparrow} = 380 \text{ K}$  and  $T_{1/2\downarrow} = 323 \text{ K}$ , exhibiting hysteresis width of 48 K in the very first cycle (Fig. 18b), where the  $\chi T$  value reached  $0.009 \text{ cm}^3 \text{ mol}^{-1} \text{ K}$  and  $3.11 \text{ cm}^3 \text{ mol}^{-1} \text{ K}$  at room temperature and 400 K respectively. However, during the next heating and consecutive cooling

cycles  $T_{1/2\uparrow}$  value decreased to 371 K while  $T_{1/2\downarrow}$  remained constant. Moreover, the HS to LS conversion in heating mode was more abrupt than the LS to HS conversion in cooling mode. The SCO phenomenon was further validated by DSC measurements, where a sharp endothermic and a broad exothermic transition at 375 K and 327 K were observed during the first heating and cooling cycle. A shift in the endothermic peak to 373 K was noticed during the second heating cycle, which is also accordant with the magnetic data. Additionally, sharp endothermic peak and the broad exothermic peak were consistent with the nature of abrupt spin transitions in heating and cooling cycles, respectively.

To investigate the synergic interconnection between luminescence and SCO, PL measurements were carried out for the **24** at 300 - 400 K, excited with 337 nm nitrogen laser. The dinuclear complex exhibited two emission peaks centered at  $\lambda_2 = 686$  nm, and  $\lambda_1 = 550$  nm, which remained unchanged upon changing temperature. The PL spectra of the **24** also revealed two emission peaks centered at  $\lambda_2 = 673$  nm and  $\lambda_1 = 550$  nm (Fig. 18c). Significant changes in the intensity of both emission peaks were observed in spin transition area upon changing temperature, where a prominent effect was noticed for the  $\lambda_1 = 550$  nm. The temperature rise of the emission intensity ratio of peaks  $\lambda_1$  and  $\lambda_2$  as  $PL(\lambda_2)/PL(\lambda_1)$  showed the occurrence of SCO following a similar curve shape as the temperature dependence of  $\chi T$  (Fig. 18d). Upon increasing temperature  $PL(\lambda_2)/PL(\lambda_1)$  stays constant up to 365 K, then starts increasing sharply to attain a constant value at around 400 K. With lowering temperature, the high-temperature value was constant down to 33 K, then reduced gradually to reach the initial value at 300 K. The overall results demonstrated a magnificent interplay among the luminescence and SCO properties in **24**.

Also, the change in the relative intensity of the peaks at  $\lambda_1$  and  $\lambda_2$  depended on the spin state of the **24** and concluded to have two competitive relaxation processes, (i) MLCT dependent

relaxation process involving excitation of one electron from metal-centered  $t_{2g}$  orbital into the ligand-centered  $\pi_L^*$  orbital and successive relaxation ( $\lambda_1$ ); (ii) metal- centered relaxation process involving excitation of one electron from metal-centered  $t_{2g}$  orbital into ligand-centered  $\pi_L^*$  orbital, thus successive transfer of one electron can take place from the ligand-centered  $\pi_L^*$  orbital to the metal  $e_g^*$  orbital, and consecutive relaxation to the metal-centered  $t_{2g}$  orbital ( $\lambda_2$ ) [80].

### 2.3. Luminescent SCO in 2D Systems

In 2019, Zuo and co-workers published the first 2D Fe(II) CP with synergetic SCO and luminescence properties [81]. The 2D CP  $\{[\text{Fe}(\text{L18})](\text{L19})_{0.5} \cdot 3\text{CH}_3\text{OH}\}_n$  (**25**·3CH<sub>3</sub>OH) was acquired as dark color red bar shape crystals from the reaction between  $[\text{Fe}(\text{L18})(\text{CH}_3\text{OH})_2]$  (**L18** = diethyl(*E,E*)-2,2'-[1,2-phenyl-bis(iminomethylidyne)]bis(3-oxobutanoate)-(2-)N,N',O3,O3') with **L19** (**L19** = 1,1,2,2-tetrakis(4-(pyridin-4-yl)phenyl)-ethene; TPPE) using liquid-liquid diffusion technique in MeOH and DCM solvents, while a desolvated sample  $\{[\text{Fe}(\text{L18})](\text{L19})_{0.5}\}_n$  (**25**) was obtained by heating **25**·3CH<sub>3</sub>OH at 77 °C under a nitrogen atmosphere over half an hour.

X-ray crystallography studies of **25**·3CH<sub>3</sub>OH at 263 and 123 K showed that the asymmetric unit contains one  $[\text{FeL2}]$  motif, half of **L3** ligand, and three CH<sub>3</sub>OH molecules as interstitial solvents (Fig. 19). Each iron center was situated in distorted octahedral  $[\text{FeN}_4\text{O}_2]$  surrounding and bound with two N and two O donor atoms coming from the ligand **L18** and two N donor atoms of two **L19** ligands. The average Fe-N, Fe-O bond distances along with the O-Fe-O bond angle, suggested the occurrence of HS and LS Fe(II) center at 263 and 123 K respectively. The Fe-N bond distances lowered to 1.924 -2.008 Å from 2.025 - 2.201 Å with decrease in the temperature from 263 K to 123 K, while also a decrease in Fe-O bond distance to 1.924 -1.956 Å from 2.070 Å was observed with lowering the temperature. Further, the O-Fe-O angle became 95° from 109° with a lowering

of the temperature. The four divergent pyridine donor atoms of **L19** ligand connected to iron(II) centers to form a 2D square grid CP, where large void areas between the square units containing methanol molecules were observed.

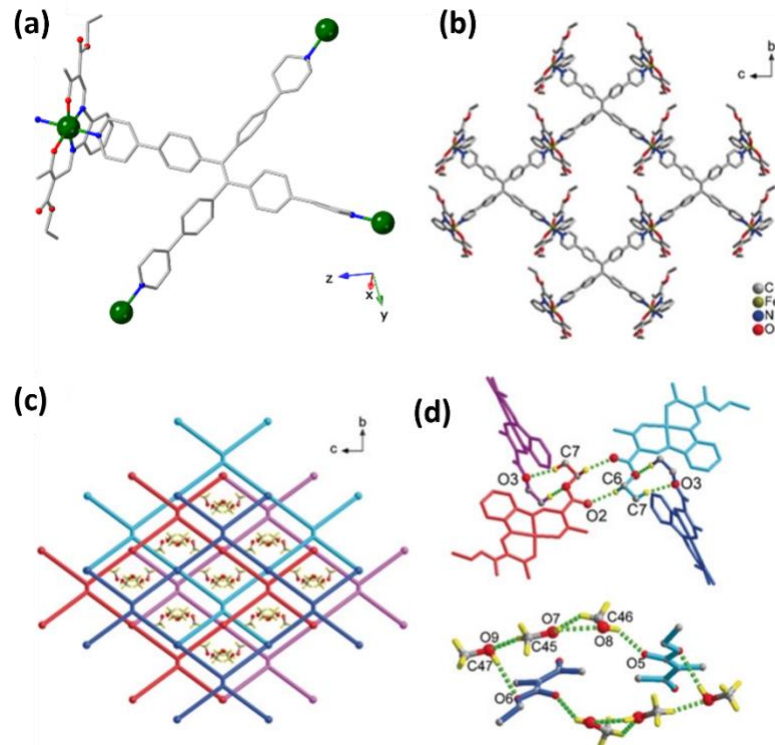


**Fig. 19.** Representative view of complex **25**· $3\text{CH}_3\text{OH}$  at 123 K. (a) Coordination surrounding of the Fe(II) center. Reproduced with permission from Ref. [81]. (b) 2D network exhibiting the  $[4 \times 4]$  connection of the ligand **L19** to Fe(II) Schiff base-like planar moiety. (c) Interlocking of adjacent layers (four layers shown in different colors). Methanol occupied the void space between layers. (d) Weak interactions (dashed lines) were obtained between the adjacent layers (top) and between  $\text{CH}_3\text{OH}$  and the network (bottom). Terminal motifs of **L19** ligand colored as blue and sky blue appear from two different 2D layers. Adapted with permission from Ref. [81].

Temperature dependency of the magnetic properties of fresh **25**· $3\text{CH}_3\text{OH}$  with partially desolvated **25**· $x\text{CH}_3\text{OH}$  and fully desolvated **25** samples have been explored in the temperature range of 300 – 2 K (Fig. 20a). Magnetic properties of **25**· $3\text{CH}_3\text{OH}$  revealed that the CP exhibited

a HS to LS transition with  $T_{1/2\downarrow} = 202$  K and  $T_{1/2\uparrow} = 227$  K showing a 25 K hysteresis width in the cooling and heating modes, where the  $\chi T$  attained a value  $3.17 \text{ cm}^3 \text{ mol}^{-1} \text{ K}$  and  $0.57 \text{ cm}^3 \text{ mol}^{-1} \text{ K}$  at around 300 K and below 100 K respectively. The hysteretic SCO properties have been significantly affected by the crystallized methanol molecules indicating the significance of the H-bonding to the SCO behavior. The partially desolvated **25**· $x$ CH<sub>3</sub>OH sample exhibited the SCO behavior with hysteresis width of 5 K ( $T_{1/2\downarrow} = 205$  K and  $T_{1/2\uparrow} = 210$  K), while gradual SCO without hysteresis at  $T_{1/2} = 205$  K was observed for fully desolvated sample **25**. Moreover, the residuary HS state population at low temperature increased with the desolvation of methanol solvent from the sample. The DSC and Mössbauer spectroscopy further supported the magnetic studies. DSC measurement of **25**·3CH<sub>3</sub>OH showed that with heating/cooling at 10 and 5 K min<sup>-1</sup>, endothermic/exothermic peaks were observed at ~230/201 and 228/202 K, respectively. The photomagnetic studies of **25** under green laser (532 nm) irradiation at 10 K revealed a 14% LS to the photo-induced HS conversion, which relaxed back to the LS ground state at 50 K ( $T_{\text{LIESST}} = 50$  K) when heated in dark.

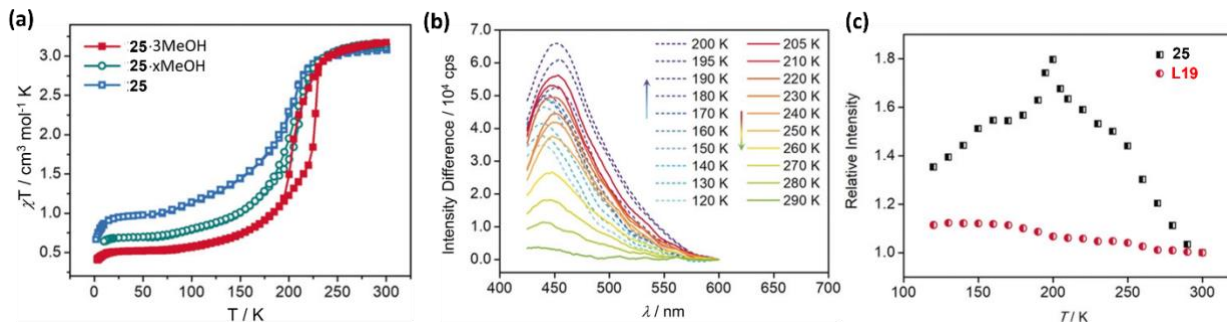


**Fig. 20.** (a)  $\chi T$  vs T plot for **25**·3CH<sub>3</sub>OH, partially desolvated form, **25**· $x$ CH<sub>3</sub>OH, and fully desolvated species **25**. (b) Difference in luminescence intensities  $\{I(T)-I(300 \text{ K})\}$  for temperatures covering SCO transition. (c) The temperature dependency of intensity at the maxima (460 nm) compared to that at 300 K for **25** (black) and L19 (red). Adapted with permission from Ref. [81].

To explore the correlation between SCO and luminescence, PL studies were performed on the free **L19** ligand and **25** in the temperature span of 120 – 300 K (Fig. 20b). At room temperature, the free **L19** ligand exhibited a strong emission peak situated at around 462 nm while excitation at 365 nm, while a similar emission peak with lower intensity ( $\lambda_{\text{em}} = 460$  nm) was noticed for **25**, confirming the retention of emission properties of **L19** ligand after coordination with the Fe(II) center. Upon increasing temperature, relative intensity ( $I(T) - I(300\text{K})$ ) was increased with temperature to reach a maximum at around SCO temperature, *i.e.*, 200 K (Fig. 20c), while a small monotonous decrease in the relative intensity due to thermal quenching was observed for free **L19** ligand. The results clearly described a synergic tie-up between luminescence and SCO in **25**.

Later in 2020, our group reported a unique 2D CP,  $\{[\text{Fe}(\mathbf{L20})_2(\text{NCSe})_2] \cdot 6\text{MeOH} \cdot 14\text{H}_2\text{O}\}_n$  (**26**) (**L20** = 2,5-dipyridylethylenylene-3,4-ethylenedioxothiophene) by incorporation of redox-active 3,4-ethylenedioxothiophene (EDOT)-based luminescent ligand (**L20**) with iron(II) center to explore SCO and luminescence properties [82]. The 2D CP was obtained as red crystals by reacting Fe:2NCSe with ligand **L20** in DCM/MeOH solvent mixture and diffusion of Et<sub>2</sub>O into the reaction mixture. Crystallographic studies at 200 and 120 K revealed that the molecular unit of **26** consisted of a neutral molecular motif  $[\text{Fe}(\mathbf{L20})_2(\text{NCSe})_2]_n$  with spacial methanol and water molecules. Each iron(II) center was in the N<sub>6</sub> coordination surrounding and coordinated to four N donor atoms of four **L20** ligands and two N donor atoms coming from NCSe<sup>-</sup> coligands (Fig. 21a). **L20** was attached to Fe(II) centers to construct the extended 2D [4 × 4] square-grid network (Fig. 21b). With decreasing temperature from 200 K to 120 K, average Fe–N<sub>Py</sub>, Fe–N<sub>NCSe</sub> bond distances of 2.212 and 2.090 Å shortened to 1.999 and 1.941 Å respectively, which suggested the HS and LS states of Fe(II) metal center at 200 and 120 K respectively. Additionally, a significant contraction of unit cell volume, the grid diagonal dimension, the Fe···Fe distance across the bridging **L20**

ligand, and the solvent-accessible void volume was detected with HS to LS conversion. Overall crystallographic studies described a thermo-induced SCO in **26**, further confirmed by magnetic measurements.

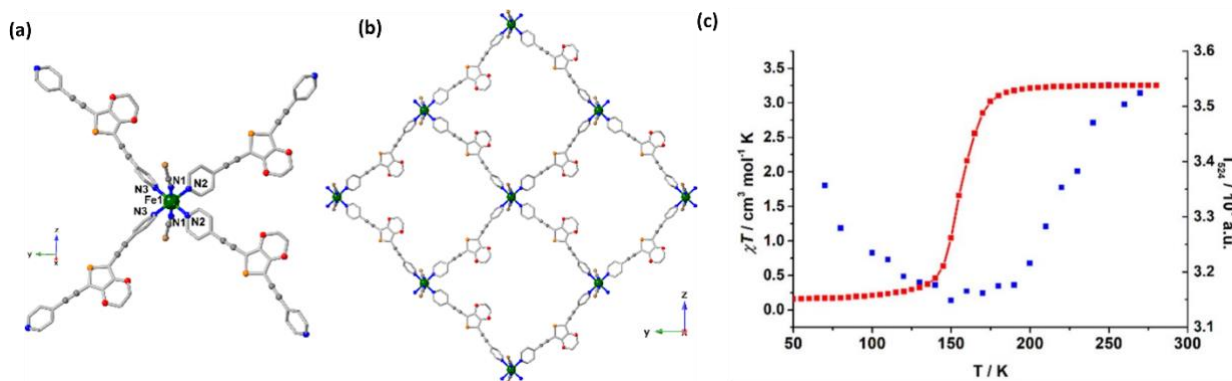


**Fig. 21.** (a) Coordination surroundings of the iron(II) center in **26**. (b) 2D network of **26** possessing a [4  $\times$  4] square grid. Hydrogen atoms and solvent molecules were excluded for clarity (colour codes: Fe, green; C, gray; N, blue; O, red; S, orange; Se, brown). (c) Temperature dependence of the luminescence intensity of the maximum emission ( $\lambda_{\text{em}} = 524 \text{ nm}$ ) for **26** along with temperature dependence of  $\chi T$  value. Adapted with permission from Ref. [82].

The magnetic properties of **26** were explored by measuring  $\chi T$  vs. T on polycrystalline samples of **26** at a magnetic field of 1000 Oe in between 280 K and 2 K (Fig. 21c, red curve). The **26** exhibited a gradual LS to HS SCO at  $T_{1/2} = 150 \text{ K}$ , where the  $\chi T$  values were 3.25 and 0.15  $\text{cm}^3 \text{ mol}^{-1} \text{ K}$  at 280 and below 55 K, respectively. The SCO property was also supported by the thermally dependent absolute reflectivity measurements. Interestingly, **26** showed ON/OFF and an almost complete photo-switching between LS ground state and photo-induced HS state using consecutive 625 nm and 850 nm light irradiation over many cycles at around 10 K under an external dc magnetic field of 10000 Oe, which was studied by absolute optical reflectivity and photomagnetic studies [82]. This photo-induced metastable HS state relaxes back to LS ground state at 80 K (showing  $T_{\text{LIESST}} = 80 \text{ K}$ ) while kept heating **26** in the dark [82].

To explore the synergic relation between SCO and luminescence in **26**, PL measurements were carried out at room temperature as well as between 270 to 70 K (Fig. 21c, blue curve). At room temperature, the **26** exhibited two emission bands centered at  $\lambda_1 = 524$  nm,  $\lambda_2 = 570$  nm while excited at 395 nm, which were significantly different from the emission band of 565 nm of the free **L20** ligand, indicating the effect of coordination of the metal center with ligand. Upon lowering the temperature, the emission intensity of  $\lambda_1 = 524$  nm ( $I_{524}$ ) decreased to reach a minimum at around 150 K and then rose gradually till 70 K (Fig. 21c). The minimization of  $I_{524}$  around SCO temperature (150 K) confirmed the unified correlation between luminescence and SCO.

In 2021, we also reported the isostructural 2D CP, similar to **26** using NCS<sup>-</sup> coligand instead of NCSe<sup>-</sup>, which exhibited thermo-and photo-induced SCO and luminescent properties; however, we could not find any correlation between SCO and luminescence behaviors in the measured window [83].

In 2021, Kurmoo and co-workers reported two polymorphic coordination polymers [84],  $[\text{Fe}^{\text{II}}\mathbf{21}(\mathbf{L19})_{0.5}]$  (**27**) and  $[(\text{Fe}^{\text{II}}_3\mathbf{L21}_3(\mathbf{L19})_{1.5})]$  (**28**), which were made up with the Fe(II) metal center, redox-active tetrathiafulvalene (TTF)-functionalized Schiff-base ligand (**L21**) and fluorescent-active TPPE ligand (**L19**) to introduce redox and synergistic SCO-luminescence properties in the system. The mixture of  $[\text{Fe}^{\text{II}}\mathbf{L21}(\text{MeOH})_2]$  and **L19** in DCM/MeOH was warmed at 70 °C for 24 hours, leading to the formation of **27**, and for 48 hours, leading to the formation of **28**. Complex **27** crystallized in monoclinic space group of  $C2/c$ . The unit cell involved one independent  $[\text{Fe}(\text{II})\mathbf{L21}]$  subunit and half of **L19** ligand. The Fe(II) coordination was little bit distorted in  $[\text{FeN}_4\text{O}_2]$  octahedral environment in which two N atoms and two O atoms from the Schiff-base ligand generate the basal plane, and other two N atoms of tetradentate bridging **L19** constructed the expected square-grid of  $[\text{Fe}(\text{II})\mathbf{L21}(\mathbf{L19})_{0.5}]$  (Fig. 22a-b). Average Fe-N<sub>eq</sub> (1.882

$\text{\AA}$ ), Fe-O<sub>eq</sub> (1.930  $\text{\AA}$ ) and Fe-N<sub>ax</sub> (2.004  $\text{\AA}$ ) bond distances were well consistent with typical LS Fe(II) unit.

The magnetic studies for **27** were performed from 2 to 350 K in 1000 Oe (Fig. 22c). The  $\chi T$  of 2.28  $\text{cm}^3 \text{ mol}^{-1} \text{ K}$  at 350 K indicated that almost 70% [LS-LS] fractions converted to [HS-HS] fractions. Then the gradual reduction in  $\chi T$  value with decrease in temperature and reaching a plateau at 1.13  $\text{cm}^3 \text{ mol}^{-1} \text{ K}$  around 90 K suggested the occurrence of SCO in Fe(II) center. Below 28 K, the  $\chi T$  product decreased to 0.71  $\text{cm}^3 \text{ mol}^{-1} \text{ K}$  till 2 K and it is due to the zero-field splitting of the residuary HS Fe(II) centers as well as antiferromagnetic interactions among Fe(II) centers.

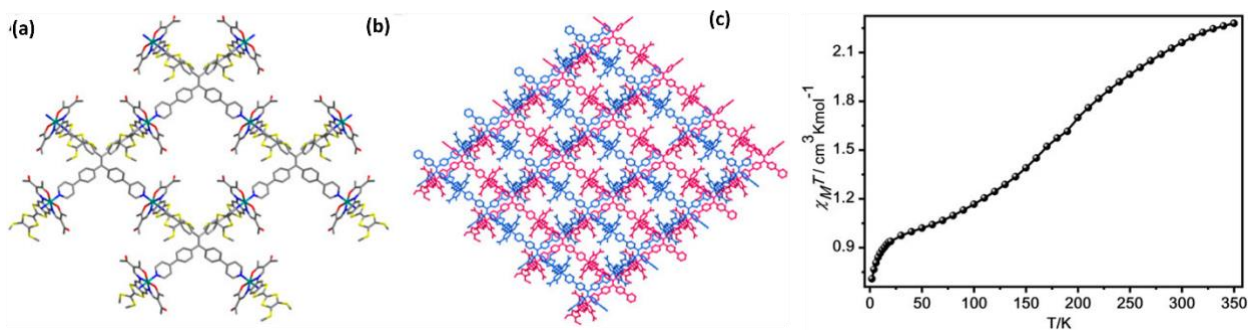


**Fig. 22.** (a) 2D network and (b) neighboring interlinking layers along *a* axis (middle) for **27**. All the hydrogen atoms were excluded for clarity; Colour code: C: grey; N: blue; O: red; S: yellow; Fe: teal. (c) The temperature dependency of  $\chi T$  product in 1000 Oe for **27**. Adapted with permission from Ref. [84].

The fluorescence properties of **L19** shows an intense emission at around 472 nm when excited with 360 nm light. Hence, when excited at 360 nm wavelength, the emission bands for **27** occurred at 442 nm, and the fluorescence intensities were reduced by a factor of three. The clear hypochromic shift occurred in fluorescence spectra, denoted as  $\pi-\pi^*$  transition in the center of the ligand. These results were credited to the coordination of Fe(II) metal center with the Schiff-base ligand and introduction of **L19** in the Fe(II) complex.

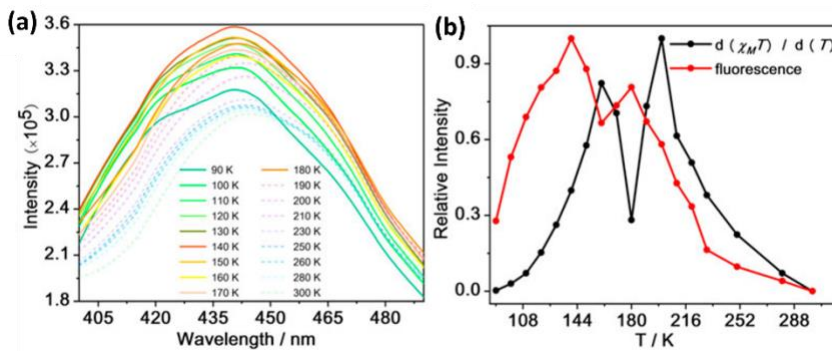


**Fig. 23.** (a) Fluorescence spectra of **27** between temperature range of 90–300 K. (b) The  $d\chi T/dT$  curve (black line) and normalized fluorescence plot (red line) for **27**. Adapted with permission from Ref. [84].

To correlate the SCO and fluorescence properties in **27**, temperature-dependent fluorescence emission study was performed from 90 to 300 K (Fig. 23a). For **27**, upon heating, the fluorescence intensity increased gradually and reached highest around 140 K followed by a decrease again till 160 K. Further above 160 K to 180 K, the intensity began to increase rapidly and decreased while further heated [84]. These extreme temperature-dependent anomaly in fluorescence intensity happened in the measured temperature range of 90–300 K and agreed quite well with the thermo-induced SCO behavior of **27**. Also, to further support this hypothesis, they have shown the normalized derivative of  $\chi T$  and fluorescence intensity curve for **27** within 90–300 K (heating mode) (Fig. 23b). The SCO profile obtained from this plot for **27** obtained are well accordant to the variations in fluorescence intensity, demonstrating the fluorescence intensity change was associated to the SCO transition.

With even longer reaction time, more close-packed complex  $[(\text{Fe}(\text{II})_3\text{L21}_3(\text{L19})_{1.5})]$  (**28**) was obtained. Again, it also crystallized in monoclinic space group of  $C2/c$ , similar to that of **27**. Here, asymmetric unit contained three autonomic  $[\text{Fe}(\text{II})\text{21}]$  units and one and a half of **L19**. Magnetic measurement was performed for **28** from 2 K to 350 K in 1000 Oe dc magnetic field. Although, at 350 K, the  $\chi T$  for **28** was obtained  $2.16 \text{ cm}^3 \text{ K mol}^{-1}$  which is quite lesser than the anticipated

value for three independent HS Fe(II) centers suggesting that significant amount of LS Fe(II) centers are also present in **28** [84].

In 2022, Wang and co-workers reported a 2D Hofman type Fe(II)-based coordination polymer and showed that the magnetic and fluorescence properties can be synchronously tuned by various external stimuli [85]. They synthesized  $[\text{Fe}(\text{L22})_2\text{Pt}(\text{CN})_4]$  (**29**) {**L22** = (E)-Nphenyl-1-(pyridin-4-yl)methanimine} complex by taking aqueous solution of  $(\text{NH}_4)_2\text{Fe}(\text{SO}_4)_2 \cdot 6\text{H}_2\text{O}$ , positioned at bottom of a test tube, then a mixture of methanol and water was put on as a buffering solvent, further freshly made methanolic solution of **L22** and  $\text{K}_2[\text{Pt}(\text{CN})_4] \cdot 3\text{H}_2\text{O}$  was layered. Orange plate type of single crystals were obtained. The dehydrated sample of **29** was obtained after heating the orange crystals for 14 h at 333 K. **29** exhibited a 2D Hofmann-type polymeric structure. **29**·xH<sub>2</sub>O was obtained by placing **29** in deionized water. Similarly, the new phase **29**·xSolv was achieved by situating **29** in water: methanol (1:1 v/v) mixture for 20 hours. These two new phases were obtained from **29** by single crystal-to-single crystal transformation

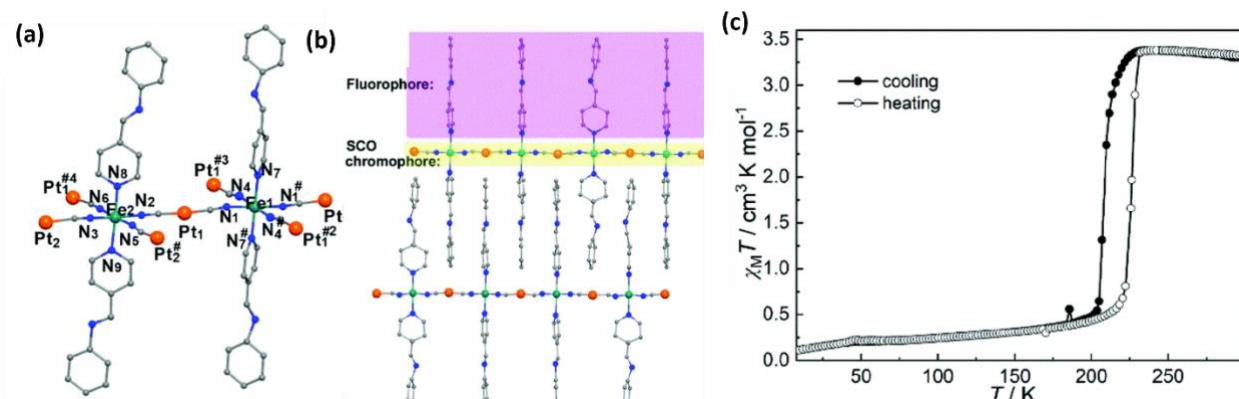


**Fig. 24.** (a) SCXRD structure of **29** at 100 K. (b) 3D representation of **29** at 100 K projected through *bc* plane. Color code: Fe: green, C: gray, N: blue, and Pt: yellow. All hydrogen and disordered atoms were excluded for clarity. (c) The thermal variation of magnetic susceptibility plot for **29**. Adapted with permission from Ref. [85].

In the asymmetric unit of **29**, two independent Fe(II) centers are present having occupancies of half (Fe1) and one (Fe2), two Pt(II) centers carrying one (Pt1) and half (Pt2) occupied atoms, six CN<sup>-</sup> and three **L22** ligands (Fig. 24a). The Fe(II) centers were coordinated to four cyanide N atoms situated at the equatorial positions, and two N atoms from **L22** ligands at the apical sites, making a distorted octahedral geometry. These Fe(II) centers were bridged through [Pd(CN)<sub>4</sub>]<sup>2-</sup> forming a 2D molecular layer (Fig. 24b). The axially oriented ligands were arranged in “head to tail” fashion with adjacent ligands from the adjoining layers.

The magnetic susceptibility measurements of **29** (Fig. 24c) revealed that the  $\chi T$  value of **29** was 3.36 cm<sup>3</sup> mol<sup>-1</sup> K in 250–290 K, defining that all the Fe(II) centers were in HS state (HS<sub>1.0</sub>LS<sub>0.0</sub>). Below 250 K, the  $\chi T$  value of **29** started decreasing and attained a value of 0.24 cm<sup>3</sup> K mol<sup>-1</sup> at 120 K, that gave clear evidence of complete spin transition with  $T_{1/2} = 205$  and 226 K in cooling and heating processes, respectively possessing a thermal hysteresis loop of ~21 K indicated an increased lattice cooperative effect among the metal centers due to the guests solvent loss.

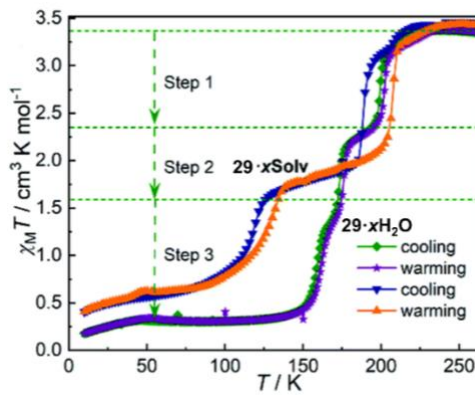


**Fig. 25.** The temperature-dependent magnetic susceptibility of **29**·xH<sub>2</sub>O and **29**·xSolv. Adapted with permission from Ref. [85].

Detailed magnetic properties of **29**·xH<sub>2</sub>O and **29**·xSolv were compared with that of the parent sample **29** (Fig. 25). The three-step spin transition was obtained for **29**·xH<sub>2</sub>O due to the

incorporation of water molecules in **29**. For **29**·xH<sub>2</sub>O, the  $\chi T$  remained constant at 3.34 cm<sup>3</sup> mol<sup>-1</sup> K from 250–300 K, suggesting all Fe(II) sites were present in HS state (HS<sub>1.0</sub>LS<sub>0.0</sub>). Upon cooling, the  $\chi T$  value decreased and attained an intermediate step situated at 188 K with  $\chi T = 2.30$  cm<sup>3</sup> mol<sup>-1</sup> K, which represents the presence of one-third of HS Fe(II) sites – defining the intermediate state of HS<sub>0.67</sub>LS<sub>0.33</sub>. A further lowering in temperature led to an plateau having the slope at around 172 K with  $\chi T = 1.63$  cm<sup>3</sup> mol<sup>-1</sup> K, indicating the presence of half of HS Fe(II) centers (HS<sub>0.50</sub>LS<sub>0.50</sub>). Below 170 K, the  $\chi T$  value decreased and attained an intermediate step of  $\chi T$  value 0.30 cm<sup>3</sup> mol<sup>-1</sup> K from 75–50 K range which suggested that small amount of HS Fe(II) still remained in this low-temperature region (Fig. 25). For **29**·xSolv, variable-temperature  $\chi T$  vs T measurements suggested that SCO of **29**·xSolv occurred in a stepwise manner of HS<sub>1.0</sub>LS<sub>0.0</sub>  $\leftrightarrow$  HS<sub>0.50</sub>LS<sub>0.50</sub>  $\leftrightarrow$  HS<sub>0.25</sub>LS<sub>0.75</sub>. For both the complexes **29**·xH<sub>2</sub>O and **29**·xSolv, SCO associated with the variation of solvent guests was further verified by variable-temperature single crystal XRD and DSC measurements.

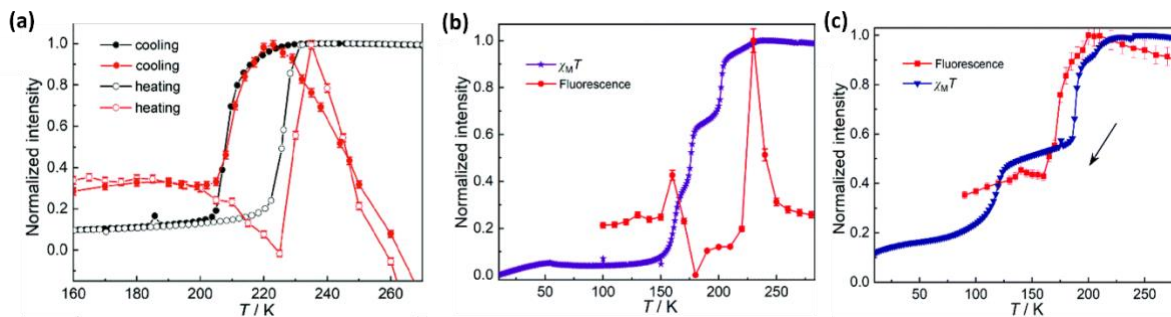


**Fig. 26.** (a) Normalized  $\chi T$  vs. T (black) and fluorescence intensity (red) of **29** in the heating and the cooling cycle. (b) Normalized temperature-dependent magnetic susceptibility and fluorescence intensity of **29**·xH<sub>2</sub>O in heating cycle. (c) Normalized  $\chi T$  vs. T and fluorescence intensity of **29**·xSolv in the cooling cycle. Adapted with permission from Ref. [85].

To find out the effect of SCO on the fluorescence properties of **29**, the temperature-dependent fluorescence intensity of **29** exhibited two peaks in the normalized intensity plot with  $T^{FL}_{max}$  at 206 K and 230 K for heating and cooling cycles from 150 – 270 K range, respectively having a hysteresis loop of 21 K [85]. These  $T^{FL}_{max}$  values of **29** were in good accordance with the spin-state switching temperatures (Fig. 26a). In the case of **29**·xH<sub>2</sub>O, three irregular peaks with  $T^{FL}_{max}$  at 162 K, 195 K, and 230 K, respectively were obtained in the fluorescence intensity versus temperature plot. These  $T^{FL}_{max}$  values provides a suitable correlation among fluorescence and spin state of **29**·xH<sub>2</sub>O (Fig. 26b). Similarly, for **29**·xSolv, presence of two anomalous peaks with  $T^{FL}_{max}$  at 140 K and 210 K matched well with the spin-transition temperatures (Fig. 26c).

In 2022, Song and co-workers reported two 2D [4 X 4] square grid complexes [86], consisting of  $\{\text{Fe}^{\text{II}}(\text{L23})_2(\text{SCN})_2 \cdot \text{CHCl}_3 \cdot 4\text{CH}_3\text{OH}\}_n$  (**30**) and  $\{\text{[Fe}^{\text{II}}(\text{L23})_2(\text{SeCN})_2]\cdot \text{CH}_2\text{Cl}_2 \cdot 4\text{CH}_3\text{OH}\}_n$  (**31**); where **L23** {3,6,11,12-tetra(pyridin-4-yl)dibenzo[*a,c*]phenazine (TPDP)} was a fluorescent tetradentate pyridine ligand exhibiting strong emissions. Crystals of **30** were obtained using layering method – the methanolic solution of Fe(NCS)<sub>2</sub> onto a solution of **L23** CH<sub>2</sub>Cl<sub>2</sub>:CHCl<sub>3</sub> (1:1, v/v) which was separated by CH<sub>2</sub>Cl<sub>2</sub>:CHCl<sub>3</sub>:CH<sub>3</sub>OH (1:1:1 v/v) solvent mixture. Slow diffusion gave dark red color bar shaped crystals of **30**. To obtain crystals of **31**, the methanolic solution of Fe(NCSe)<sub>2</sub> was layered onto a solution of **L23** using CH<sub>2</sub>Cl<sub>2</sub>:CH<sub>3</sub>OH (2:1, v/v) and CH<sub>2</sub>Cl<sub>2</sub>/CH<sub>3</sub>OH (1:1 v/v) mixture solution as a buffer layer. Red color rod-like crystals were obtained after 7 days at room temperature.

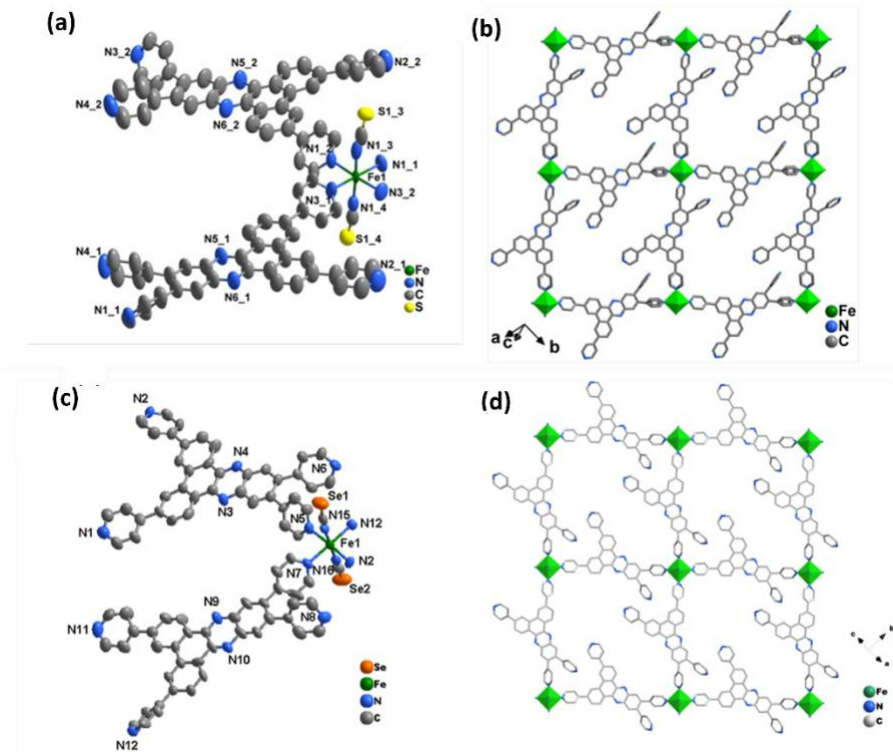


**Fig. 27.** (a) Coordination surroundings of the Fe(II) center in **30**. (b) [4×4] 2D grid network of **30**. (c) The octahedral coordination surroundings of Fe(II) metal center in **31**; (d) 2D [4 × 4] network of **31** along *c* axis; Hydrogen atoms were removed for clarity. Adapted with permission from Ref. [86].

**30** and **31** crystallized in monoclinic space group of *Cc*. The asymmetric units of both **30** and **31** were connected by two **L23** and  $\text{Fe}(\text{NCX})_2$  [ $\text{X} = \text{S}$  (**30**) and  $\text{Se}$  (**31**)] moieties. The coordination environment for Fe(II) centers in both **30** and **31** were having slightly distorted octahedral  $[\text{N}_6]$  geometry where Fe(II) centers was connected by four equatorial  $\text{N}_{\text{pyridyl}}$  atoms of two **L23** ligands, and two axial N atoms of  $\text{NCX}^-$  coligands. Since, **L23** is planar, so these 2D grids exhibited interesting planer geometry (Fig. 27).

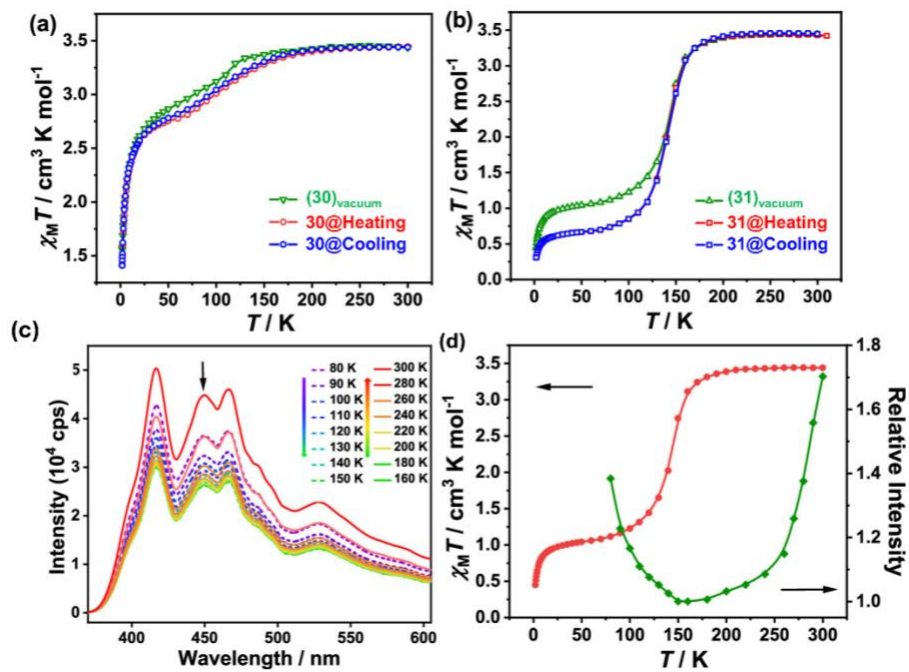


**Fig. 28.**  $\chi T$  vs T plots of (a) **30** and (b) **31** in the heating (red curve) and cooling (blue curve) cycles using 1000 Oe magnetic field. (c) Temperature-dependent fluorescence spectra of vacuum-desolvated complex  $(\mathbf{31})_{\text{vacuum}}$ , excited at 330 nm. (d) Plots of  $\chi T$  (red) and normalized emission intensity (green) as a function of temperature for  $(\mathbf{31})_{\text{vacuum}}$ . Adapted with permission from Ref. [86].

The  $\chi T$  vs. T measurements were performed for **30** and **31** under externally applied dc magnetic field of 1000 Oe from 300–1.8 K (Fig. 28a and 28b). For **30**, the  $\chi T = 3.45 \text{ cm}^3 \text{ mol}^{-1} \text{ K}$  at 300 K suggested single isolated HS Fe(II) ion containing remarkable orbital contribution. While decreasing the temperature till 190 K,  $\chi T$  value was fixed and then gradually lowered to  $2.75 \text{ cm}^3 \text{ mol}^{-1}$  around 50 K with a  $T_{1/2} = 110 \text{ K}$ , suggesting the occurrence of incomplete and gradual SCO in **30** (Fig. 28a). Then the  $\chi T$  value was dropped abruptly upon decreasing the temperature below 50 K to  $1.31 \text{ cm}^3 \text{ mol}^{-1} \text{ K}$  at 1.8 K, which might be due to the zero-field splitting (ZFS) of residuary HS Fe(II) centers or the antiferromagnetic interactions involving the adjacent Fe(II) centers (Fig. 28a). In the case of **31**, the  $\chi T$  remained constant at  $3.47 \text{ cm}^3 \text{ mol}^{-1} \text{ K}$  within 300–180

K. As the temperature reduced to 80 K,  $\chi T$  sharply decreased to  $0.73 \text{ cm}^3 \text{ mol}^{-1} \text{ K}$  and reached a plateau at  $0.56 \text{ cm}^3 \text{ mol}^{-1} \text{ K}$  till 12 K, indicating that **31** underwent a one-step but incomplete SCO having  $T_{1/2}$  of 144 K. This fast decrease in  $\chi T$  value below 12 K was also because of the ZFS of the residuary HS Fe(II) centers or the antiferromagnetic interaction among Fe(II) centers (Fig. 28b). Also, exothermic and endothermic peaks at around 147 K in DSC measurement during heating and cooling cycles matched well with the  $T_{1/2}$  of SCO [86]. Magnetic susceptibility data for the partially desolvated  $(\mathbf{30})_{\text{vacuum}}$  and  $(\mathbf{31})_{\text{vacuum}}$  samples, revealed that the SCO in  $(\mathbf{30})_{\text{vacuum}}$  and  $(\mathbf{31})_{\text{vacuum}}$  could be prompted by the solvents, and more fractions of HS Fe(II) centers were situated at the low-temperature region while the SCO temperature for  $(\mathbf{31})_{\text{vacuum}}$  didn't change with the removal of solvents.

To look insight into the correlation between the fluorescence and SCO of  $(\mathbf{31})_{\text{vacuum}}$ , temperature dependency of the fluorescence was measured for pure **L23**, while excited at 378 nm from 80–300 K. At 80 K, the emission spectra of **L23** exhibited major peak having a shoulder located at around 487 and 513 nm, respectively (Fig. 28c). With increased temperature, the shoulder peak started vanishing, and the major peak was slightly red shifted at 497 nm at 300 K (Fig. 28c). The emission intensity was found to be 6.6 times lesser compared to that of at 80 K, indicating thermal quenching behavior. Then temperature dependency of fluorescence emission spectra of  $(\mathbf{31})_{\text{vacuum}}$  was measured with excitation of 330 nm from 80–300 K (LS to HS SCO). At 80 K, the emission spectra exhibited three main bands at 417, 450, and 467 nm and a very less intense shoulder band at 528 nm – confirming that the fluorescence behavior for **L23** and  $(\mathbf{31})_{\text{vacuum}}$ , were contrasting in which the major band of  $(\mathbf{31})_{\text{vacuum}}$  showed a hypsochromic shift as compared to that of **L23**. While warming to 150 K, the emission intensity gradually lowered to a minimum value nearby the  $T_{1/2} = 144 \text{ K}$  might be due to the thermal quenching behavior of fluorescence. Above 150 K, the emission

intensity increased continuously reaching the highest value at 300 K. The fluorescence intensities of **(31)<sub>vacuum</sub>** and **L23** at 450 and 487 nm manifested intuitively (Fig. 28d). Hence, it has been stated clearly that synchronization exists between spin states changes and fluorescence emission. However, the intensity of fluorescence emission in the HS state of the metal center was vast stronger than the LS state, revealed that the effect of change in the spin-state of Fe(II) center was higher than the thermal quenching effect originated through the SCO process. By studying the variable temperature SCXRD structures of **(31)<sub>vacuum</sub>** at 100 K and 173 K, it was established that the intermolecular interactions between **L23** and SeCN<sup>-</sup> were prominently decreased with increment of temperature, thus decreasing the efficiency of intermolecular energy transfer and canceling the nonradiative decay, which caused a proper rise in fluorescence intensity at HS states. Thus, it has been demonstrated that the SCO property affected the fluorescence behavior of **(31)<sub>vacuum</sub>**.

#### 2.4. Luminescent SCO in 3D Systems

In 2018, Real and co-workers reported cooperative luminescence and SCO properties in 3D Fe(II) Hofmann-type CP for the first time [87]. The CP {Fe(**L24**)[Au(CN)<sub>2</sub>]@pyr (**32@pyr**) (**L24** = 1,4-bis(4-pyridyl)benzene) was incorporated along with pyrene (pyr) as guest molecule. The CP **32@pyr** and analogous Zn(II) CP **33@pyr** were prepared as pale yellow and white crystals, respectively, using diffusion technique by taking stoichiometric equivalents of M<sup>II</sup>(BF<sub>4</sub>)<sub>2</sub>·6H<sub>2</sub>O (M<sup>II</sup> = Fe, Zn), **L24**, K[Au(CN)<sub>2</sub>] and an excess of pyrene in MeOH.

Single crystal X-ray structure analyses of both CPs revealed that the isostructural CPs were crystallized in monoclinic space group Cc. There were two crystallographically non-equivalent [M(II)N<sub>6</sub>] motifs formed by four N donor atoms appearing from four linear [NC-Au-CN]<sup>-</sup> units in

equatorial positions and two nitrogen donor atoms coming from two **L24** ligands in axial positions (Fig. 29a). Four equivalents of  $[M(II)N_6]$  motifs bridged by the  $[NC-Au-CN]^-$  units to form aligned pile of  $\{M_4^{II}[Au(CN)_2]_4\}_n$  2D grids, which were pillared by the **L24** ligands to generate a 3D open scaffold with the primitive cubic unit (pcu) topology. Additionally,  $\{M_4^{II}[Au(CN)_2]_4\}$  framework interpenetrated to an identical framework, which was constructed from the other crystallographically non-equivalent  $[M(II)N_6]$  motif. The void space created by two permeating skeletons were occupied by two crystallographically non-equivalent pyrene guest molecules, forming several strong short  $\pi-\pi$  interactions with the coordinated **L24** ligands. Moreover, strong Au…Au interactions played an important role in holding two frameworks. For Fe(II) CP **32@pyr**, the average Fe–N bond distances are 1.960 and 2.154 Å at 120 and 280 K, respectively, confirming the presence of Fe(II) LS and HS respectively at these measured temperatures and a thermo-induced SCO within Fe(II) metal center.

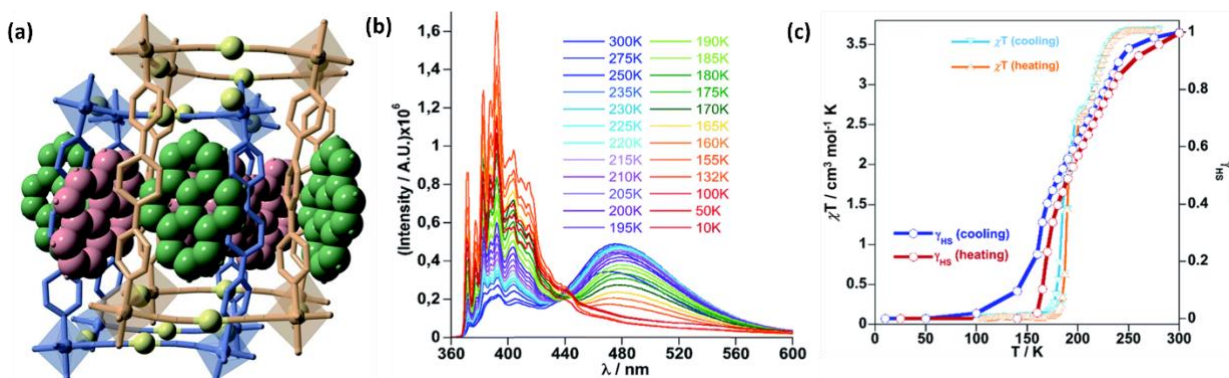


**Fig. 29.** (a) Two perpendicular perspective side views of the identical fragment of the doubly interpenetrated networks of **32@pyr** showing the **L24** pillars, coordination centers, and pyrene units. Two crystallographically independent networks, represented in blue (network 1) and beige (network 2) colors, while the different pyrene molecules were shown in red (pyr1) and green (pyr2) colors. Au centers were yellow spheres. (b) Temperature-dependent fluorescence spectra, cooling from 300–10 K at 5 K min<sup>-1</sup> for

**32@pyr.** (c) Comparison of the SCO and luminescence properties achieved from magnetic measurements and fluorescence spectroscopy for **32@pyr**. Adapted with permission from Ref. [87].

Magnetic measurements were performed for Fe(II) CP **32@pyr** in the temperature range 300 – 10 K [87]. The  $\chi T$  value at 300 K is  $3.64 \text{ cm}^3 \text{ mol}^{-1} \text{ K}$ , confirming the HS state of Fe(II) center in **32@pyr** with significant orbital contributions. Decreasing the temperature with scan rate of 1 K min<sup>-1</sup>,  $\chi T$  vs T plot displayed a drastic decrease in  $\chi T$  value to  $0.14 \text{ cm}^3 \text{ mol}^{-1} \text{ K}$  in the temperature range 250 – 160 K with three succeeding steps centered at 227, 195, and 180 K, confirming a complete three stepped SCO between HS to LS. While heating, the  $\chi T$  vs T plot exhibited the hysteresis in the 2<sup>nd</sup> and 3<sup>rd</sup> steps with ~ 5 K wide. Such three-stepped SCO might result from a contest between ferro- and antiferro-elastic interrelation driven by the volume difference accompanied with the LS and HS centers. The stepped SCO behavior was further supported by DSC plots, which showed three exothermic as well as endothermic peaks in cooling/heating mode, which were agreeing with the  $\chi T$  vs T plot [87]. The photomagnetic studies of **32@pyr** under red light ( $\lambda = 633 \text{ nm}$ ) irradiation at 10 K revealed that the  $\chi T$  value increases continuously to reach saturation with a value of  $3.50 \text{ cm}^3 \text{ mol}^{-1} \text{ K}$ , describing a complete photo-conversion from LS state to photo-induced metastable HS state, which relaxed back to the LS ground state at 50 K ( $T_{\text{LIESST}} = 50 \text{ K}$ ) upon heating in dark [87].

To explore the synergic cooperation among luminescence and SCO in **32@pyr**, PL measurements were performed within 300 K and 10 K in heating and cooling cycles using scan rate of 5 K min<sup>-1</sup> upon excitation at 332 nm (Fig. 29b). At room temperature, **32@pyr** exhibited two emission peaks centered at 400 and 500 nm respectively attributing to the monomer and excimer of pyrene. Upon cooling down the temperature down to 190 K, the intensity of both peaks

slightly increased while again cooling down in the range of SCO around 235 – 155 K, the monomer signal intensity increased substantially along with concomitant quenching of the excimer signal. No such changes in the intensity of emission peaks at 439 and 484 nm for the Zn(II) CP **33@pyr** were detected, describing the synergic relationship among luminescence and SCO properties in **32@pyr**. From the PL intensity ratio at 392 and 478 nm during heating and cooling at scan rate of 5 K min<sup>-1</sup>, the thermal development of the normalized HS molar fraction ( $\gamma_{HS}$ )<sup>norm</sup> achieved (Fig. 29c). The thermal SCO established depending on the luminescence characteristics of **32@pyr** matched well with the SCO curve obtained from magnetic measurements.

Later, in 2020, Real and co-workers also explored the extrinsic and intrinsic nature of luminescence in correlation with SCO properties in a series of 3D Fe(II) Hofmann-type CPs [88]. They prepared {Fe<sup>II</sup>(**L25**)[M<sup>I</sup>(CN)<sub>2</sub>]<sub>2</sub>} (**L25** = bis(4-pyridyl)anthracene, M<sup>I</sup> = Ag (**34**), Au (**35**) as well as pyrene as guest inserted {Fe<sup>II</sup>(**L26**)[M<sup>I</sup>(CN)<sub>2</sub>]<sub>2</sub>}·pyrene (**L26** = bis(4-pyridyl)butadiyne, M<sup>I</sup> = Ag (**36@pyr**), Au (**37@pyr**)). The CP **34**, **35** and their analogous zinc CP **34/35-Zn** were obtained by diffusion technique using equivalent ratio of M<sup>II</sup>(BF<sub>4</sub>)<sub>2</sub>·6H<sub>2</sub>O (M<sup>II</sup> = Fe, Zn), **L25** and K[M<sup>I</sup>(CN)<sub>2</sub>] (M<sup>I</sup> = Ag, Au) in methanol. Similarly, crystals of **36@pyr** and **37@pyr** were obtained following a similar protocol with methanol solutions of fluorophoric pyrene moiety, **L26** instead of **L25**. Crystallographic analyses revealed that the structure of all 3D CPs was essentially similar to that of **32@pyr**. However, the most notable changes were observed in the accessibility of the pcu framework depending on the length of the bridging ligands. Moreover, strong  $\pi$ – $\pi$  stacking among guest pyrene molecules and the coordinated bridging ligands were observed for the guest-inserted CPs **36@pyr** and **37@pyr** [88]. In contrast, a symmetry breaking with the change of the space group from monoclinic *P2/c* to orthorhombic *Cmma* upon decreasing temperature from 280

to 100 K was observed in **35** (Fig. 30a-b). Similar to **32@pyr**, the change in average Fe-N bond distance of around 0.2 Å between 100 K and 280 K, confirming SCO in the system.

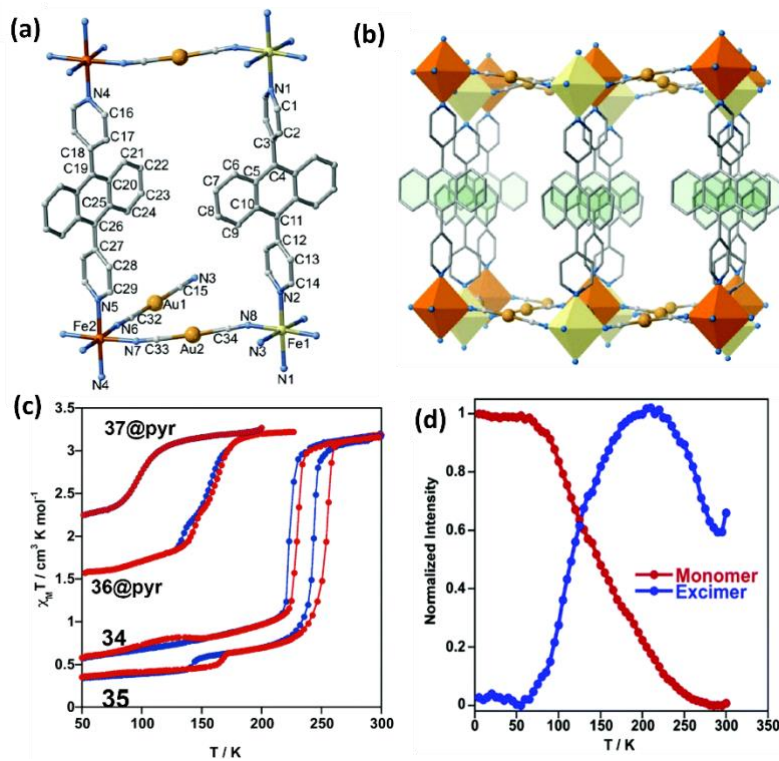


**Fig. 30.** (a) Illustrative fragment of the network with given atom numbering for the asymmetric unit of **35** at 280 K, Color Code: Fe1: Yellow, Fe2: Orange, Au: Mustard Yellow, C: Grey, N: Blue, and (b) perspective view single 3D network of **35**; Yellow- and orange-colored octahedrons represents Fe1 and Fe2, respectively. (c)  $\chi_T$  vs. T plots of complexes **34**, **35**, **36@pyr**, and **37@pyr** (blue and red filled circles represents to the cooling and heating cycles, respectively). (d) Temperature dependency of the monomer and excimer emission intensity of **36@pyr** in the cooling cycle. Adapted with permission from Ref. [88].

Magnetic properties of all the Fe(II) CPs **34**, **35**, **36@pyr**, and **37@pyr** were investigated by magnetic susceptibility measurements between 300 and 50 K (Fig. 30c). For all CPs, the observed  $\chi_T$  value at 300 K is around  $3.20 \text{ cm}^3 \text{ mol}^{-1} \text{ K}$ , confirming the HS state of Fe(II) center with significant orbital contributions. Upon lowering the temperature,  $\chi_T$  vs T plot for CP **35** displayed two-step SCO with a spin state conversion of 80% and 10% at  $T_{1/2}(1)\downarrow/T_{1/2}(1)\uparrow = 242/252 \text{ K}$ ,

$T_{1/2}(2)\downarrow/T_{1/2}(2)\uparrow = 143/163$  K with hysteresis loops of 10 K and 20 K respectively. While a one-step SCO of  $T_{1/2}(1)\downarrow/T_{1/2}(1)\uparrow = 222/228$  K having hysteresis loop of 6 K was observed for the CP **34**. Additionally, a slight enhancement in the  $\chi T$  value was noticed above 85 K which got stabilized at around 130 K, defining an asymmetric hysteresis loop. In contrast, pyrene-inserted CPs **36@pyr** and **37@pyr** exhibited incomplete SCO, where  $\chi T$  vs T plot for the CP **37@pyr** displayed two-step SCO with a spin state conversion of 31% and 15% at  $T_{1/2}(1)\downarrow/T_{1/2}(1)\uparrow = 156/160$  K,  $T_{1/2}(2)\downarrow/T_{1/2}(2)\uparrow = 136/143$  K with the hysteresis loops of 4 K and 7 K respectively. A gradual SCO at  $T_{1/2}$  ( $\sim 100$  K) with a presence of 52% residuary Fe(II) HS was observed for the CP **36@pyr**. DSC measurements further supported the SCO behaviors of the CPs.

To explore the synergic relation among luminescence and SCO along with the impact of coordinated luminescent ligand *vs* luminescent guest, Temperature-dependent PL measurements were performed on CPs **34** and **36@pyr** between 300 K and 10 K upon excitation at 345 nm [88]. The CP **36@pyr** exhibited similar behavior to that of CP **32@pyr** as described above (Fig. 30d). In contrast, at room temperature, the CP **34** exhibited two emission peaks between 350-490 nm and 490-700 nm respectively, corresponding to the monomer and excimer coming from the anthracene unit of the coordinated ligand **L25** [88]. With lowering the temperature, both the peak intensities enhanced, while further cool down around SCO region of 230 K, the monomer signal intensity increased highly with concomitant quenching of the signal of the excimer. The thermal SCO was established, depending upon the luminescence properties of **34** which is matching well with the SCO characteristics obtained from magnetic measurements, suggesting the synergic relationship among luminescence and properties in **34**.

In 2022, Wu and co-workers reported two new 3D Hofmann-type fluorescence-active SCO complexes  $[\text{Fe}(\text{L19})\text{Ag}(\text{CN})_2]\text{ClO}_4 \cdot 5\text{MeOH} \cdot 14\text{H}_2\text{O} \cdot \text{CH}_2\text{Cl}_2$  (38) and  $[\text{Fe}(\text{L19})\text{Au}(\text{CN})_2]\text{ClO}_4 \cdot 14\text{MeOH} \cdot 18\text{H}_2\text{O} \cdot \text{CH}_2\text{Cl}_2$  (39) [89]. **38** was prepared by taking the mixture of **L19** in DCM and  $\text{K}[\text{Ag}(\text{CN})_2]$  in methanol, which was kept at the bottom of a test tube, followed by methanol:DCM (1:1, v/v) mixture as a buffer solution. Then a methanolic solution of  $\text{Fe}(\text{ClO}_4)_2 \cdot 6\text{H}_2\text{O}$  was added on top of the buffer solution. This gave yellow block crystals of **38** after 5 days. **39** was also synthesized by following a similar method of **38** by taking  $\text{K}[\text{Au}(\text{CN})_2]$  instead of  $\text{K}[\text{Ag}(\text{CN})_2]$ .

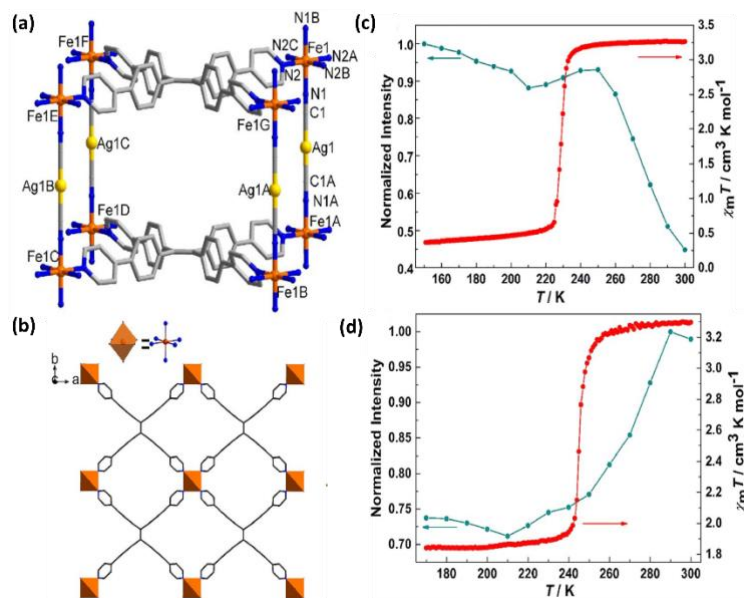


**Fig. 31.** (a) Representative 3D network of **38** at 100 K, Color code: Fe: Orange, Ag: Yellow, C: Grey, N: Blue. (b) Perspective representation of the **L19**-bridged layer for **38** along the *c*-axis direction. (c)  $\chi T$  and normalized maximum fluorescence emission intensity ( $\lambda_{\text{ex}} = 355$  nm) in the heating cycle for **38**. (d)  $\chi T$  and normalized maximum fluorescence emission intensity ( $\lambda_{\text{ex}} = 355$  nm) in the heating process for **39**. Adapted with permission from Ref. [89].

The quality of single crystals of **39** was not good enough to diffract well, which prevented the exact determination of its structure even at 173 K. But its actual network can be observed by seeing 173 K data, which was isostructural to **38**. Single Crystal structure of **38** at 100 K showed that it crystallized in the orthorhombic space group of *Pmmm*. It consisted of  $[\text{Fe}(\text{L19})\text{Ag}(\text{CN})_2]^+$  polymeric ion, in which the Fe(II) centers were bridged by **L19** and  $[\text{Ag}(\text{CN})_2]^-$  anion to build the 3D cationic CP (Fig. 31a-b). The  $\text{ClO}_4^-$  counteranions and various solvent molecules were present within the cavity of the network. Fe(II) centers were attached with four N atoms from **L19** ligands situated in the equatorial plane, two N atoms of  $[\text{Ag}(\text{CN})_2]^-$  bridging ligands positioned at the axial positions. At 260 K, the unit cell volume was higher than four times as compared to that of at 100 K and the space group of the crystal system became *Cmmm*.

Magnetic susceptibility measurements for **38** revealed that almost all Fe(II) centers have encountered a spin transition with a  $T_{1/2} = 230$  K in the temperature range of 300–10 K [89]. However, no hysteresis was observed. The magnetic properties of the fully desolvated **38** showed HS nature in the measured temperature range, suggesting that the SCO behavior was highly related to the lattice solvent molecules. **39** showed an abrupt and incomplete SCO without hysteresis with a  $T_{1/2} = 245$  K. The fully desolvated form of **39** exhibited a gradual and incomplete SCO within 75–200 K temperature range [89].

A notable bathochromic shift was observed in fluorescence emission maxima for **38** (534 nm) as compared to free **L19** (462–480 nm) at 150 K. As the temperature increased, the fluorescence emission intensity of **38** gradually lowered, which was well in agreement with the thermal quenching as expected. However, with increase in temperature above 210 K, the fluorescence intensity started to enhance exceptionally and reached a maxima at 250 K, and then decreased further (Fig. 31c). For **39**, the abnormal emission behavior was observed from 210–290 K (Fig.

31d). Also, it showed a red shift of 28 nm as temperature increased from 170 to 300 K. The complete desolvated solid sample of **39** showed the red shift of 29 nm in 100–150 K which defined that the structural variation was responsible for the gradual SCO. Hence, the experimental outcomes revealed that the complexes **38**, **39**, and desolvated **39** exhibited synergic fluorescence-SCO correlations.

In 2023, Liu and co-workers, reported Fe(II)-based 3D MOF [ $\{\text{Fe}(\text{L27})[\text{Ag}(\text{CN})_2]_2\} \cdot 2\text{EtOH}$ ]<sub>n</sub> (**40**) having interpenetrated Hofmann-type structure [90]. Pale yellow crystals of **40** were acquired from slow diffusion in H-tube reaction using  $\text{Fe}(\text{ClO}_4)_2 \cdot 6\text{H}_2\text{O}$  and a bidentate ligand **L27**,  $\text{K}[\text{Ag}(\text{CN})_2]$  in ethanol and DMF mixed solvent. The asymmetric unit of **40** consisted of one individual Fe(II) center, half of **L27** ligand and single  $[\text{Ag}(\text{CN})_2]^-$  unit along with one EtOH molecule as crystalline solvent molecule (Fig. 32a). The  $[\text{Ag}(\text{CN})_2]^-$  units bridged the Fe(II) centers to construct 3D Hofmann-type grid network  $[\text{Fe}_6\{\text{Ag}(\text{CN})_2\}_6]_n$ , in which the **L27** ligands were aligned across the network, bridging the Fe(II) centers (Fig. 32b).

Magnetic susceptibility of **40** from 2–300 K under 1000 Oe dc field revealed an incomplete SCO with  $T_{1/2} = 161$  K (Fig. 32c) without any thermal hysteresis loop. Temperature-dependent UV-vis absorption spectra of **40** at 300 K revealed an absorption band around 840 nm. But at around 100 K, it showed two absorption bands around 410 – 450 and 500 – 590 nm. Hence, 532 and 808 nm laser lights were taken into account to study the photo-responsiveness in **40**. By using 532 nm laser light (it showed maximum enhancement in  $\chi T$  value) at 10 K, **40** showed the  $T_{\text{LIEST}}$  of 75 K (Fig. 32c). In contrast, the 808 nm laser light irradiation at 10 K on metastable HS Fe(II) for 90 min lowered the  $\chi T$  value from  $2.36 \text{ cm}^3 \text{ mol}^{-1} \text{ K}$  to  $0.69 \text{ cm}^3 \text{ mol}^{-1} \text{ K}$ , which indicated that the metastable HS Fe(II) state might be reversibly transformed back into the LS state when 808 nm light was used on sample – confirming the reverse LIEST effect (Fig. 32d).

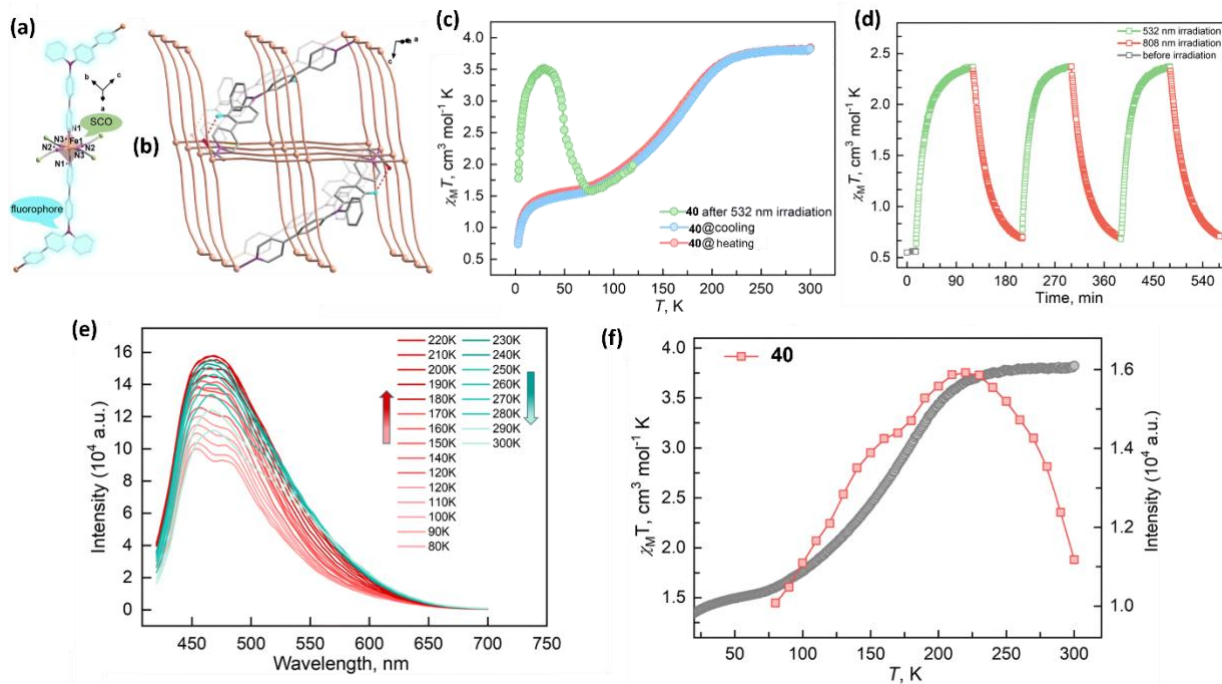


**Fig. 32.** (a) Coordination surroundings of the Fe(II) metal for **40** at 120 K. (b) 3D Hofmann-type network of  $[Fe_6\{Ag(CN)_2\}_6]$  grid. Red dashed lines represented C–H...O interactions among the ligands and crystallized EtOH molecules. Hydrogen atoms and solvent molecules were excluded for clarity. Color codes: Fe, orange; Ag, pale green; N, violet; C, pale gray; H, blue; O, red. (c)  $\chi T$  vs. T for **40** under 1000 Oe dc magnetic field. (d) Multiple cycles of  $\chi T$  vs. time after successive irradiation with 532 and 808 nm lasers at 10 K for **40**. (e) Variable temperature fluorescence emission spectra for **40** in solid state while excited at 398 nm during heating process from 80 K to 300 K. (f) Temperature dependency of  $\chi T$  and the fluorescence intensity of the maximum emission for **40**. Adapted with permission from Ref. [90].

To investigate the synergistic relationship among fluorescence and SCO in **40**, variable temperature fluorescence spectra were recorded for **40** from 80 to 300 K while heating the sample, using the excitation light of 398 nm ( $\lambda_{ex}$ ). The fluorescence emission spectra of **40** at 80 K exhibited two bands having the maxima at around 450 nm and 480 nm. With a rise in temperature from 80 K, both of these two bands became intensified and merged into one band showing the maxima at

220 K. Upon further increase in temperature, the intensity decreased further (Fig. 32e). Temperature dependency of the emission intensity exhibited a similar portrait to that of the  $\chi T$  value till 225 K, and above which the thermal quenching occurred predominantly. This anomaly in fluorescence increment was observed from 80–220 K, exhibiting the similar temperature range for the SCO (Fig. 32f), confirming the complex **40** is showing the synergetic relation among the fluorescence and SCO.

## 2.5. Luminescent SCO Nanomaterials

The advancing research in the field of SCO combined with prevalent advancements in techniques and technologies to implement these systems in real-world applications has led to a development in the field of SCO systems in various forms such as nanoparticles, nanopatterns, nanocomposites, nano-heterostructures, and thin films. This part of the review concerns the presentation of attempts at exploring the luminescent SCO systems in various applications. Luminescence is an easy-to-detect property that can indicate the occurrence of molecular events in real-time and space. Luminescent SCO nanoparticles provide the best of both worlds, where we can exploit their applicability in magneto-optical switches.

The first report in 1999 by Fabbrizzi and co-workers outlined a modular approach to design a two-component luminescent sensor for temperature using spin-state switching of the Ni<sup>II</sup> ion in a tetra-aza coordinative environment (Fig. 33a) in square planar (LS) and octahedra (HS) geometry (Fig. 33b). The high-spin/low-spin conversion in  $[\text{Ni}^{\text{II}}(\text{L28})]^{2+}$  (**41**) is endothermic, where increasing temperature favors the LS square planar form of the complex, and the emission spectra recorded over the temperature range established the applicability of  $[\text{Ni}^{\text{II}}(\text{L28})]^{2+}$  as a thermometric probe operating at the molecular level (Fig. 33c) [91].

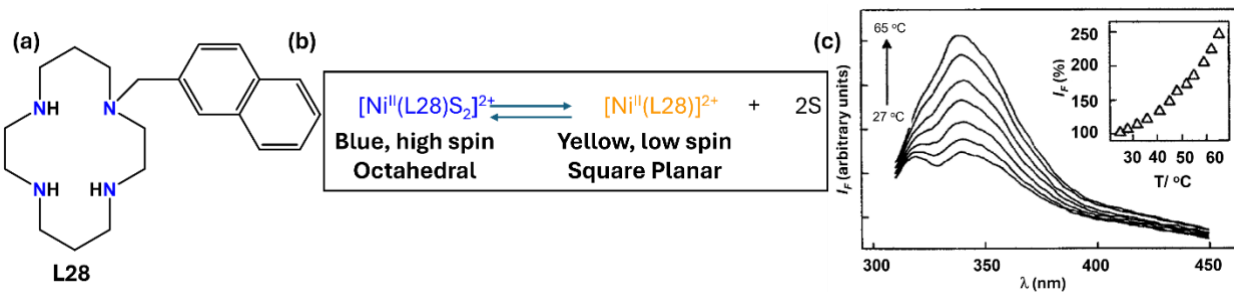


**Fig. 33.** (a) Schematic representation of cyclam ligand decorated with naphthalene fluorescent fragment, (b) schematic representation of solution phase equilibrium mixture of the high- and low-spin forms for Ni(II) complex, (c) Emission spectra of  $[Ni^{II}(L28)](ClO_4)_2$  in MeCN recorded in the temperature range 27–65 °C and the inset shows IF vs. temperature profile. Adapted with permission from Ref. [91].

In 2008, Matsuda and co-workers reported the first observation of thermo-induced ON/OFF switching of the electroluminescent (EL) emission in an organic thin film device spin-coated with SCO active  $[Fe(dpp)_2](BF_4)_2$  (**42**) ( $dpp=2,6\text{-di(pyrazol-1-yl)pyridine}$ ) [92]. The ease of formulating a thin film of **42**, owing to its solubility in a polar solvent, with retention of SCO property, facilitated the fabrication of ITO/chlorophyll a– $[Fe(dpp)_2](BF_4)_2$ /Al [93]. Further investigation of this led to the conclusion that **42** acts as the electron injection material, leading to the formation of electron-hole pairs, which recombine with electrons to give radiative luminous emission in OLEDs. The quenching of EL results from low-temperature LS Fe(II) form, where the excited state of the luminophore is responsible for electroluminescence beyond  $T_c$  does not occur due to a change in the efficiency of the charge injection process [94].

The attempts at thermal imaging using a two-component system involving a combination of thermal phase transition in SCO nanoparticles of  $[Fe(NH_2Trz)_3](X)_2$  ( $X = OTs^-$  (**43**) or  $NO_3^-$  (**44**)) with fluorescent properties of a fluorescent agent (rhodamine-110) within one material were reported by Bousseksou and co-workers for thermometry application *via* thermal imaging in 2010 [95]. In 2011, Colacio and co-workers fabricated bifunctional SCO  $\{[Fe(HTrz)_2(Trz)](BF_4)\}_n$  (**45**)

/luminescence (3-(dansylamido)propyltrimethoxysilane) nanoparticles using a silica matrix. In nanoparticles, the bulk magnetic and optical bistability are conserved, and the spin state switching of **45** can alter the luminescence of the fluorophore grafted on the surface of the nanoparticles [96]. In 2012, Bousseksou and co-workers reported thin films and nanopatterns of  $[\text{Fe}^{\text{II}}(\text{hptrz})_3](\text{OTs})_2$  (**46**) (hptrz: 4-heptyl-1,2,4-triazole and Ots: tosylate) doped with acridine orange by spin coating and soft-lithography, respectively. The spin state changes for the thin films can be traced through luminescence measurements at thicknesses below 100 nm. Soft lithography technique was used to pattern the regular arrays of **46** where SCO behavior wasn't much affected by the size of nanoparticles. The study traced the thermo-induced variation of luminescence in the thin films, arrays, and, the most fascinatingly, in the individual nano-dots [97]. Colacio and co-workers further reported pure and silica-wrapped Fe(II)-triazole SCO nanoparticles where magnetic properties are significantly modified by the silica shell surrounding the nanostructured Fe(II)-triazole polymer. These silica-wrapped Fe(II)-triazole nanoparticles were coated with a dansyl-based fluorophore, where the spin state of the SCO polymer guided the luminescence properties. Further, the time-dependent luminescence indicated the existence of Förster-type non-radiative energy transfer between LS Fe(II) ion and dansyl-based fluorophore [98]. Bousseksou and co-workers reported pyrene-functionalized  $[\text{Fe}(\text{H-trz})_2(\text{trz})]\text{BF}_4$  (**47**) and silica shell hybrid nanoparticles with unaltered SCO and the direct impact of SCO on the excimer luminescence from pyrene fluorophore [99]. Bousseksou and co-workers reported nanorods of  $[\text{Fe}(\text{Htrz})_2(\text{trz})]\text{BF}_4@\text{SiO}_2$  with a  $\text{Tb}^{3+}$  complex chemically bound to the silica surface, showing the first-ever successful use of rare earth luminescence to follow the SCO process [100]. Further, in 2016, Bousseksou and co-workers reported the nanomaterial containing the luminescent CdTe nanocrystals,  $[\text{Fe}(\text{H-trz})_2(\text{trz})]\text{BF}_4$  nanoparticles grafted with  $\text{SiO}_2$  or BPEI shells, undergoing a

reversible alteration of the luminescence intensity upon the spin transition [101]. In 2017, Bousseksou and co-workers reported near-infrared-emitting luminescent nanocomposite material of the  $[\text{Fe}(\text{Htrz})_2\text{-}(\text{trz})]\text{(BF}_4)$  SCO nanoparticles by associating them with Cy7-NHS polymethine cyanine dye as a doping agent (Fig. 34a). This SCO-Cy7-BPEI nanocomposite (Fig. 34) exhibited hysteretic SCO (Fig. 34b) and an unexpected reversible and strong luminescence intensity drop when switching the spin state from HS Fe(II) to the LS Fe(II) (Fig. 34c-f). The luminescence-intensity variation with SCO in the composite is attributed to the change in the crystal lattice (volume, stiffness, *etc.*) upon undergoing SCO. This study revealed the possibility of molecular spin-state switching affecting the luminescence behavior without any spectral overlap between the metal complex and the luminophore [102].

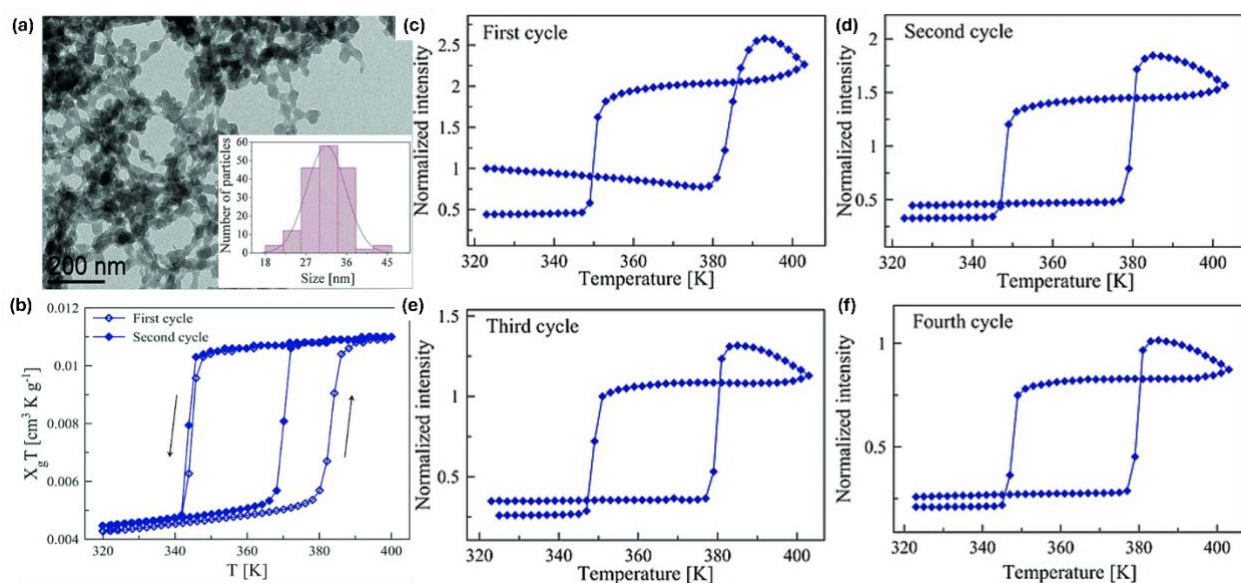


**Fig. 34.** (a) TEM image and size-distribution histogram of SCO-Cy7-BPEI nanocomposite, (b) bulk magnetic susceptibility versus temperature for the SCO-Cy7-BPEI nanocomposite, (c) Luminescence intensity vs. temperature for SCO-Cy7-BPEI nanocomposite [excitation  $(700 \pm 7)$  nm, emission  $(780 \pm 25)$  nm]. Adapted with permission from Ref. [102].

In 2018, Tao and co-workers reported 9-anthraldehyde (AD) and 9-phenanthrenecarboxaldehyde (PD) fluorophores coupled with the 1D SCO compound  $[\text{Fe}(\text{L30})_3](\text{ClO}_4)_2$  (**48**, L=4-amino-1,2,4-triazole) undergoing a synchronized spin-state switching and changes in the fluorescence intensity. Bousseksou and co-workers reported bilayer thin films of SCO complex  $[\text{Fe}(\text{HB(tz)}_3)_2]$  (**49**) and the luminescent complex  $\text{Ir(ppy)}_3$  (ppy: tris(2-phenylpyridine), where the change in the spin state of iron ions around 337 K causes a reversible jump in the luminescence intensity. This study shows that luminescence can indicate thermo-induced SCO [103]. Herrera and co-workers reported bare and silica coated nanocomposites of SCO active  $\{[\text{Fe}(\text{NH}_2\text{Trz})_3](\text{BF}_4)_2\}_n$  (**50**) complex where the silica shell of the nanoparticles was grafted with luminescent Re(I) complex affording a bifunctional SCO luminescence material. Temperature-dependent studies showed a synchronization between luminescence and SCO [104]. A few reports have been on SCO responsive Aggregation-Induced (AI) Emission [105, 67].

### 3. Spin Crossover and Dielectricity Coupled Systems

#### 3.1. Spin Crossover and Dielectricity Coupled in 0D Molecules

Nakano and co-workers first studied the dielectric behavior along with the SCO property in 2002, where they studied a Mn(III) SCO complex and found that  $[\text{Mn}(\text{L29})]$  (**51**) [ $\text{L29}$  = tris(1-(2-azolyl)-2-azabuten-4-yl)amine] (Fig. 35a) exhibit changes in the dielectric property at same temperature region where the SCO occurs, around 48 K (Fig. 35b). They commented that this behavior is due to the dynamic Jahn Teller effect of the HS state which leads to higher Mn-N bond length and thus higher polarizability and higher dielectric permittivity of the system [59].

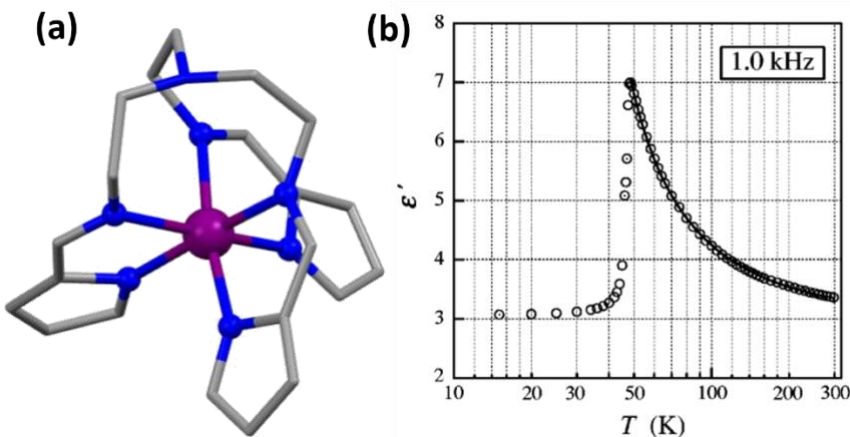


**Fig. 35.** (a) Simplified crystal structure of **51** omitting hydrogen atoms and counteranions for clarity (Mn: purple, N: blue, C: gray) (b) Plot of temperature dependent change of dielectric constant  $\epsilon'$  for **51** at 0.1 KHz. Above 48 K, the solid line represents the Curie-Weiss law with  $\theta = 26$  K and  $C = 91$  K. Adapted with permission from Ref. [59].

Then, in 2003, this phenomenon was observed with some Fe(II) complexes, as reported by Bousseksou and co-workers. Some previously synthesized complexes (**52-57**) were taken for this work, and their dielectric property at variable temperatures were measured, and then a correlation between the SCO and dielectric property was established [52]. A dielectric hysteresis loop (Fig. 36a,c) is observed in the temperature dependence of dielectric property measurements. Among the six samples studied here, only one sample showed a decrease in the dielectric constant from LS to HS state (Fig. 36c-d), and others exhibited an increase in the dielectric constant (Fig. 36a).

Magnetic and dielectric parameters for other complexes are summarized in Table 2.

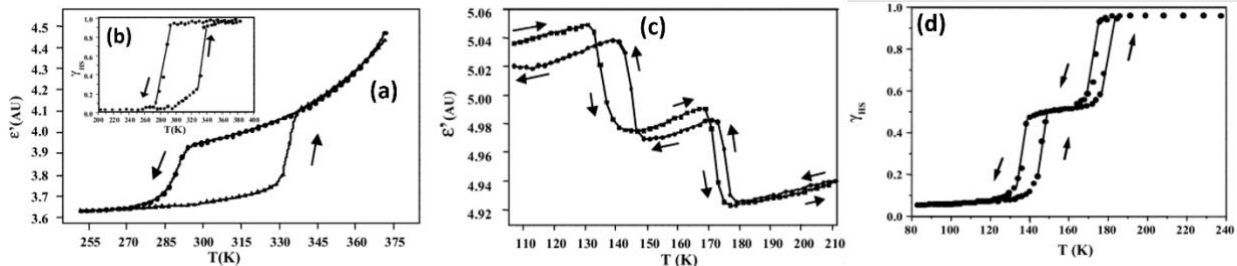


**Fig. 36.** (a) Thermal hysteresis of the dielectric constant associated with the spin-transition of  $[\text{Fe}(\text{L30})_3](\text{NO}_3)_2$  (**52**). (b) Thermal variation of HS percentage ( $\gamma_{\text{HS}}$ ) of molecules ( $\gamma_{\text{HS}}$ ) in **52**. (c) Thermal hysteresis loops of the dielectric constant associated with the two-step spin-transition in  $\text{Fe}(\text{L31})$  (**53**). (d) Thermal variation HS percentage ( $\gamma_{\text{HS}}$ ) of molecules in **53** obtained from  $\chi$  vs T measurements. (Data points are connected to guide the eye). Adapted with permission from Ref. [52].

Later, in 2006, the same group investigated the change in dielectric property upon light irradiation. This is very important as the combination of dielectric switching and optical addressability are two necessary requirements for applying these materials in information storage and for reading and writing the information.  $[\text{Fe}(\text{L35})(\text{CN})_2]\cdot\text{H}_2\text{O}$  (**58**), complex was used for this study which has a  $T_{\text{LIEST}}$  of 130 K [106]. From the temperature dependency of magnetic and the dielectric properties (Fig. 37a-b), it can be clearly seen that both properties change in a very similar fashion, proving the synergy between these two properties. Also, from the light-induced excitation and relaxation experiments (Fig. 37c), it was found that the dielectric properties can be switched using light irradiation. To support this change in the polarizability upon photo-irradiation, they also performed DFT calculations, which showed that the average polarizability is always higher in the HS state than in the LS state.

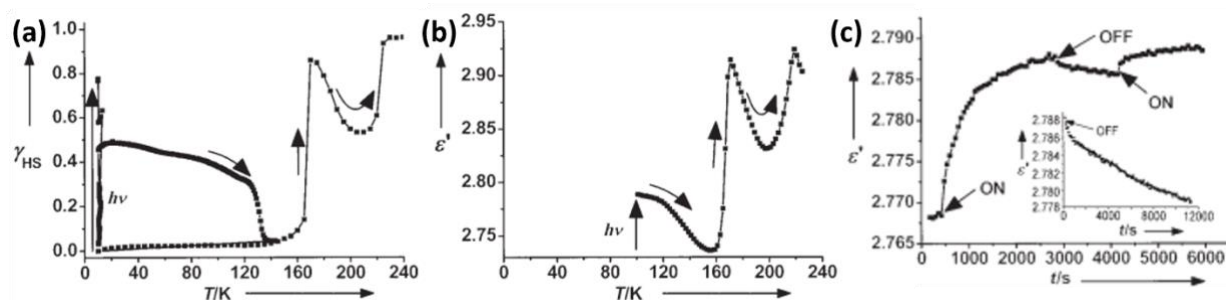


**Fig. 37.** (a) Thermal variation of the fraction of HS molecules ( $\gamma_{\text{HS}}$ ) in **58** obtained from  $\chi$  vs T measurements with light irradiation at 10 K. (b) Thermal variation of the dielectric constant in **58** following light irradiations at 100 K. (c) At 100 K, light irradiation dependent change of the dielectric constant for **58**

(initially in a pure LS state) is shown. The points at which the light source was switched ON and OFF are indicated by the labels “ON” and “OFF” respectively. The relaxation curve at 115 K with the irradiation at 100 K is shown in the inset. Adapted with permission from Ref. [106].

In an article by Guillon and co-workers, it was found that  $[\text{Fe}(\text{L36})_2][\text{BF}_4]_2$  (**59**) (Fig. 38a) shows higher relative permittivity in the LS state than the HS state (Fig. 38b-c), which is in contrast with the general observation in most of the complexes where the relative permittivity is higher in the HS state. DFT calculations were performed on the complex (**59**) cation, but that also provided contrasting observations where the mean electronic polarizability change was positive,  $\Delta\alpha = \alpha_{\text{HS}} - \alpha_{\text{LS}} = 7.01$  a.u. From this, they concluded that counteranion and various intermolecular interactions play a major role in shaping the overall electronic polarizability and, hence, the relative permittivity of molecules in particular spin states [107].

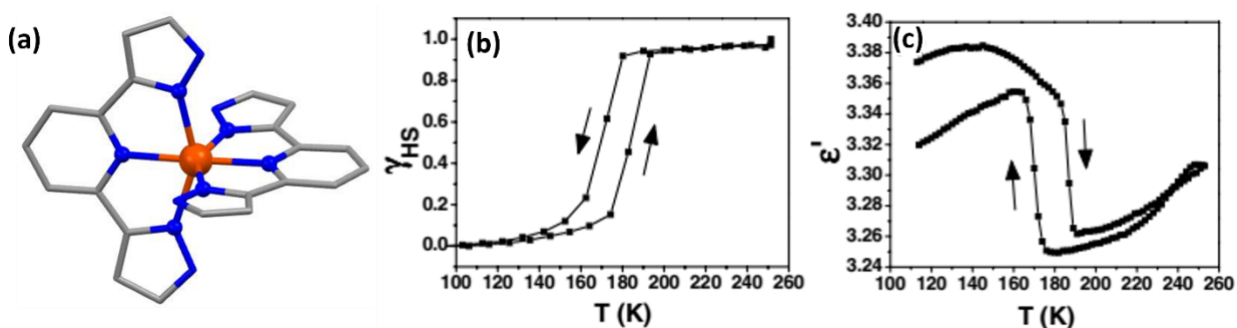


**Fig. 38.** (a) Optimized crystal structure of the cation  $[\text{Fe}(\text{L36})_2]^{2+}$  in the HS state. Hydrogen atoms and counteranions are excluded for clarity (Fe: orange, N: blue, C: gray) (b) Thermal variation of the proportion of HS molecules ( $\gamma_{\text{HS}}$ ) in **59** obtained from  $\chi$  vs T measurements. (c) Thermal hysteresis of the dielectric constant associated with the spin transition of **59**. Adapted with permission from Ref. [107].

In 2013,  $\text{Fe}(\text{H-L37})(\text{L37}) \cdot \text{H}_2\text{O}$  (**60**) (Fig. 39a) was reported to exhibit SCO and dielectric anomaly for the first time in Fe(III) system by Sato and co-workers [57]. They used a thiosemicarbazide-based ligand for this purpose, having  $\text{N}_2\text{O}_2\text{S}_2$  coordination environment around the Fe(III) center. The magnetic data revealed that the complex exhibits a two-step spin transition

with a small hysteresis loop (Fig. 39b). In the dielectric study, it was observed that it shows dielectric anomaly around 240 K and 270 K, which is where the two-step spin state change happens. Still, the dielectric change is not accompanied by any hysteresis loop (Fig. 39c). This is most probably due to the less cooperativity in the system. In order to obtain a hysteresis in the dielectric property, a strong cooperative interaction is essential criteria. This becomes more clear when we look at  $[\text{Fe}(\text{H-L38})(\text{L38})](\text{BF}_4)$  (**61**) and its magnetic and dielectric behavior. It shows a robust spin transition with 25 K width of hysteresis loop. In the dielectric property study with respect to temperature, it was found to exhibit a 25 K-wide hysteresis loop and a change large change in the real part of dielectric permittivity. Here also, the LS value is higher than HS state [108].

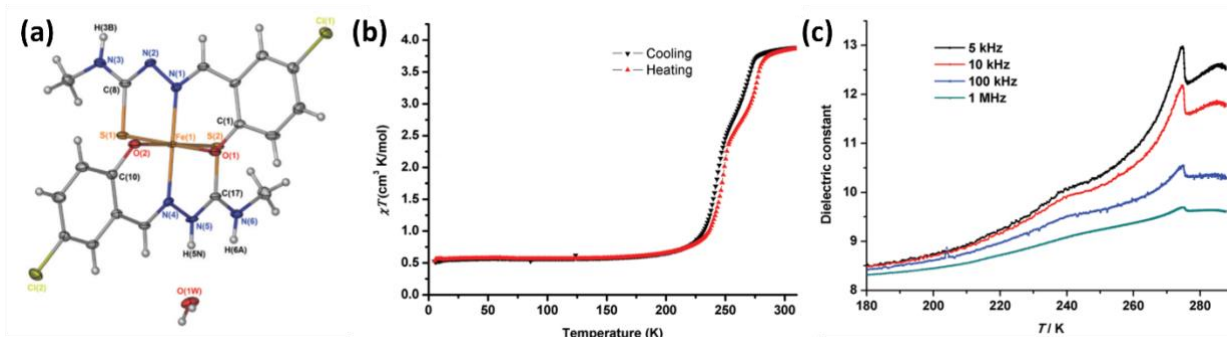


**Fig. 39.** (a) Crystal structure of **60** (thermal ellipsoid plot at the 50% probability level). (b) Temperature-dependent magnetic susceptibility data. (c) Variation of dielectric constant with temperature at different frequencies. Adapted with permission from Ref. [57].

Simultaneous occurrence of thermal, light-induced SCO along with dielectric anomaly was also observed for  $[\text{Fe}_2\text{L39}_2(\mu\text{-L39})_3(\text{NCSe})_4]\cdot 2\text{DMF}\cdot 2\text{H}_2\text{O}$  (**62**) [109]. The dielectric anomaly was observed at 165 K, confirming the synergy between SCO and dielectric property as the spin transition ( $T_{1/2}$ ) was observed at 164 K. In an effort to create multifunctional material, Li, Xiong, Zuo, and co-workers synthesized a complex having a chiral center to induce chirality as well as dielectric property into the system (Fig. 40a). Advantage of coupling a chiral center with a SCO

active metal center is that it can provide magneto-chiral dichroism [110]. They used two enantiomeric chiral ligands (*R*)/(*S*)-4,5-pineneypyridyl-2-pyrazine [(*R*)/(*S*)-**L40**]. These complexes [ $\text{Fe}\{(\text{R})\text{-L40}\}(\text{bpz})_2$ ] ( $\text{bpz}$  = bis(1-pyrazolyl)borohydride) (**63R**) and [ $\text{Fe}\{(\text{S})\text{-L40}\}(\text{bpz})_2$ ] (**63S**) exhibits very interesting hysteretic SCO behavior. **63R** shows a narrow 2 K wide hysteresis loop ( $T_{\text{up}} = 189$  K and  $T_{\text{down}} = 187$  K) (Fig. 40b). **63R** and **63S** also show LIESST effect and 57% and 73% LS to HS conversion, respectively, after light irradiation. Circular dichroism (CD) and vibrational circular dichroism (VCD) spectra show the chiral nature of the complexes. When the dielectric property is measured, the real part of the dielectric constant ( $\epsilon'$ ) exhibits an anomaly around 200 K, indicating a structural phase transition resulting from the SCO. A hysteresis loop is also observed in the dielectric temperature dependence curve having  $\Delta\epsilon' = \epsilon'_{\text{HS}} - \epsilon'_{\text{LS}} = 0.58$  for **63R** (Fig. 40b), and this value is 0.46 for **63S**. These differences in the dielectric constant at LS and HS are rather higher than usual SCO complexes as the polarizability is coming mainly from the electronic contributions in the SCO complexes. In these chiral molecules, the ligand is polar, and thus, dipolar reorientation can contribute significantly to the dielectric response. So, in these complexes, both SCO and chirality play a major role in the higher  $\Delta\epsilon'$  value of the complexes [58].

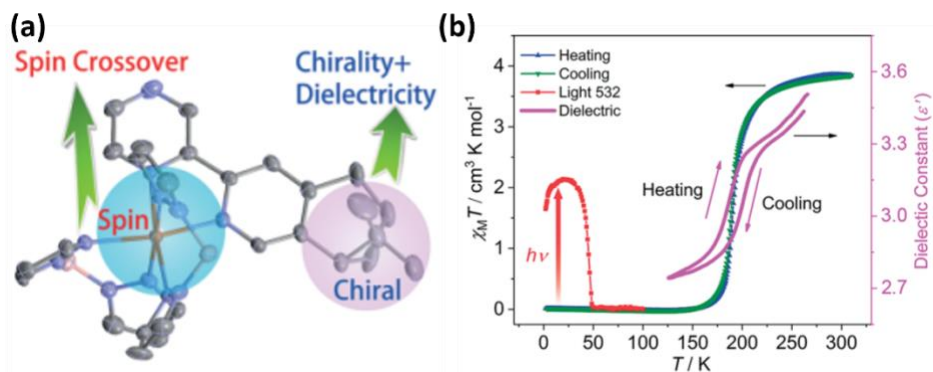


**Fig. 40.** (a) Schematic representation of the molecule designed and its components to combine chirality, spin crossover, and dielectricity. (b) The  $\chi T$  vs  $T$  plot for **63R** with 1000 Oe applied dc field and after light irradiation (red squares). The triangles (blue) and inverted triangles (green) denote  $\chi T$  values with

increasing and decreasing temperatures, respectively. The purple line represents the dielectric constant ( $\epsilon'$ ) versus  $T$  plot for **63R**. Adapted with permission from Ref. [58].

**Table 2.** Characteristic parameters of SCO and dielectric properties

Compounds	Tc (up) K	Tc (down) K	$\Delta T/K$	$\Delta \epsilon'_{HL}$	Reference
[Mn( <b>L29</b> )] ( <b>51</b> )	43.7	43.7	0	0	59
[Fe( <b>L30</b> ) <sub>3</sub> ](NO <sub>3</sub> ) <sub>2</sub> ( <b>52</b> )	337	287	50	0.3	52
Fe( <b>L31</b> ) ( <b>53</b> )	145	135	10 (Tc1)	-0.07	52
	(Tc1)	(Tc1)		(Tc1)	
	176	172	4 (Tc2)	-0.06	52
	(Tc2)	(Tc2)		(Tc2)	
Fe <sub>0.8</sub> Ni <sub>0.2</sub> ( <b>L32</b> ) <sub>2</sub> (NCS) <sub>2</sub> , H <sub>2</sub> O ( <b>54</b> )	146	126	20	0.03	52
Fe( <b>L33</b> ) <sub>2</sub> (NCS) <sub>2</sub> ( <b>55</b> )	179	174	5	0.15	52
Fe( <b>L34</b> ) <sub>2</sub> (NCS) <sub>2</sub> ( <b>56</b> )	179	178	1	0.015	52
[Fe <sub>0.85</sub> Zn <sub>0.15</sub> ( <b>L30</b> ) <sub>3</sub> ](NO <sub>3</sub> ) <sub>2</sub> ( <b>57</b> )	280	280	0	0.008	52
[Fe( <b>L35</b> )(CN) <sub>2</sub> ]·H <sub>2</sub> O ( <b>58</b> )	172	159	13	0.17	106
[Fe( <b>L36</b> ) <sub>2</sub> ][BF <sub>4</sub> ] ( <b>59</b> )	186	170	16	-0.11	107
Fe(H- <b>L37</b> )( <b>L37</b> )·H <sub>2</sub> O ( <b>60</b> )	249	245	4	---	57
	(Tc1)	(Tc1)			
	278	270	8	---	57
	(Tc2)	(Tc2)			

[Fe(H- <b>L38</b> )( <b>L38</b> )](BF <sub>4</sub> ) ( <b>61</b> )	372	348	24	5	108
[Fe <sub>2</sub> <b>L39</b> <sub>2</sub> (μ-	164	164	0	0	109
<b>L39</b> ) <sub>3</sub> (NCSe) <sub>4</sub> ]·2DMF·2H <sub>2</sub> O ( <b>62</b> )					
[Fe{(R)- <b>L40</b> }(bpz) <sub>2</sub> ] ( <b>63R</b> )	189	187	2	0.58	58
[Fe{(S)- <b>L40</b> }(bpz) <sub>2</sub> ] ( <b>63S</b> )	192	190	2	0.46	58
[Fe <sup>II</sup> ( <b>L41</b> )(bipy)] <sub>n</sub> ( <b>64</b> )	334.7	326.6	8.1	0.3	111
[Tp)Fe <sup>III</sup> (CN) <sub>3</sub> ] <sub>2</sub> Fe <sup>II</sup> ( <b>L42</b> )·4H <sub>2</sub> O	171	169	2	1.9	112
( <b>65</b> )					
[Fe <sup>II</sup> ( <b>L43</b> )][(pzTp)Fe <sup>III</sup> -(CN) <sub>3</sub> ] <sub>2</sub>	134	128	6	2.3	54
( <b>66</b> )					
{Fe( <b>L44</b> )[Pt(CN) <sub>4</sub> ]}·0.5anth ( <b>67</b> )	189, 178, 136, 112	---	2.5	60	
	(four	step			
		transition)			
{[Fe( <b>L45</b> ) <sub>2</sub> ][Pt(CN) <sub>4</sub> ]}) ( <b>68</b> )				113	
{[Fe( <b>L45</b> ) <sub>2</sub> ][Pd(CN) <sub>4</sub> ]}) ( <b>69</b> )				113	
{Fe( <b>L46</b> ) <sub>2</sub> [Ag(CN) <sub>2</sub> ] <sub>2</sub> }·2EtOH	231	---	0.9	114	
( <b>70</b> )					

bpz = bis(1- pyrazolyl)borohydride, bipy = 4,4'-bipyridine, pzTp = tetrakis(pyrazolyl)borate,  
anth = anthracene, Tp = hydrotris(pyrazolyl)borate.

### 3.2. Spin Crossover and Dielectricity Coupled in 1D - 3D Systems

In order to increase the change in the dielectric response during the SCO, the local change in spin-state and structure can be used as a trigger to control the spin arrangement and charge distribution in the whole framework. Several extended frameworks were studied in this aspect.

Here, a negatively charged cyanide-based building block is used along with Fe(II) metal ions and connecting ligands having nitrogen on both ends to bind the metal centers. The main idea is that if the molecules are strongly connected to each other, then changes in one metal center can propagate throughout the crystal framework, creating a more cooperative SCO and leading to higher changes in the dielectric tensor.

A Jager type of ligand (**L41**) has been utilized for synthesizing 1D Fe(II) complex for multifunctional behavior. A redox-active tetrathiafulvalene (TTF) functionalized Schiff-base ligand is chosen as a chelating ligand to the Fe(II) center and ditopic linker 4,4'-bipyridine (bipy) is used to form a one-dimensional polymer,  $[\text{Fe}^{\text{II}}(\text{L41})(\text{bipy})]_n$  (**64**) (Fig. 41a). The magnetic profile shows a 8 K wide thermal hysteresis in the  $\chi T$  vs T plot. The dielectric property measurement profile with respect to temperature exhibits a thermal hysteresis in the same region where the magnetic thermal hysteresis occurs (Fig. 41d). This synergistic change in the dielectric and magnetic properties come from the fact that there is a local structural change in the Fe(II) octahedron due to the spin-state change and also there is bending motion of the TTF moiety associated during SCO process (Fig. 41b-c). The  $\epsilon'$  value is high in the LS state and low in the HS state [111].

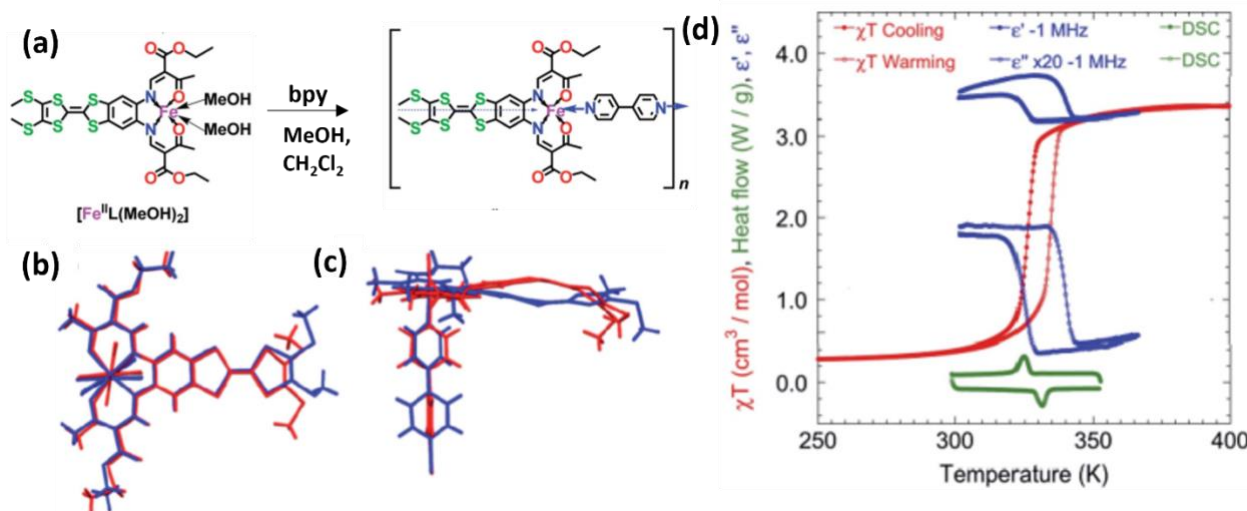


**Fig. 41.** (a) Synthesis of the metal complex **64**. Top (b) and side (c) views of the superposition of the basic molecular structures at 350 K (red) and 123 K (blue). (d)  $\chi T$  versus T plot with 10000 Oe DC field (red) at a rate of 2 K min<sup>-1</sup>. Real and imaginary (20) dielectricity is shown by blue points at a rate of 20 K min<sup>-1</sup> and DSC is represented by green line at a rate of 15 K min<sup>-1</sup> around the HS–LS transition. Adapted with permission from Ref. [111].

Liu and co-workers coupled a negatively charged paramagnetic unit and a positively charged SCO unit by using  $[\text{Fe}^{\text{III}}(\text{Tp})(\text{CN})_3]^-$  ( $\text{Tp}$  = hydrotris(pyrazolyl)borate) as a building block. Along with this Fe(II) and 4,4'-azopyridine (**L42**) was also used to form a layer structure. This provided  $\{\text{Fe}^{\text{III}}_2\text{Fe}^{\text{II}}\}$  double-zigzag chains (Fig. 42a-c) which are bridged by cyanide ligand and further linked by 4,4'-azopyridine ligands along the axial direction of the Fe(II) centers,  $\{[(\text{Tp})\text{Fe}^{\text{III}}(\text{CN})_3]_2\text{Fe}^{\text{II}}(\text{L42}) \cdot 4\text{H}_2\text{O}\}$  (**65**). The magnetic study reveals that the SCO occurred around 170 K without any hysteresis, and at low temperatures, the  $\chi T$  value increases, which is due to ferromagnetic interaction between  $\text{Fe}^{\text{III}}_{\text{LS}}$  ions and the residual  $\text{N}\equiv\text{C}-\text{Fe}^{\text{II}}_{\text{HS}}-\text{C}\equiv\text{N}$  species (Fig. 42f). LIESST effect was also observed for this complex, and it is also very sensitive to the applied external pressure. The transition temperature is found to shift to a higher temperature with applying more pressure, which happened due to the increase of the energy gap between  $t_{2g}$  and  $e_g$  levels upon applying pressure (Fig. 42f). Dielectric measurements revealed a 25 K wide thermal hysteresis and the real part of the dielectric constant changes from 3.4 to 5.3 at 0.5 kHz (Fig. 42d). Such changes in dielectric constant is rather unusual and generally  $\Delta\epsilon$  (HS-LS) varies from -0.07 to +0.3 and is attributed to the local structural changes. In this particular case, the bond angles and distances around the Fe(II) center change drastically from LS to HS, and also one of the negatively charged  $[\text{Fe}^{\text{III}}(\text{Tp})(\text{CN})_3]^-$  unit shows rotation during the process of SCO while the other one is locked by hydrogen bonding (Fig. 42e). All these changes lead to a large change in the polarization of the molecule leading to high change in the dielectric constant value. The local dielectric dipole

moment calculations show that the dipole moment increases from 10.49 D in LT phase to 14.46 D in the HT phase [112].

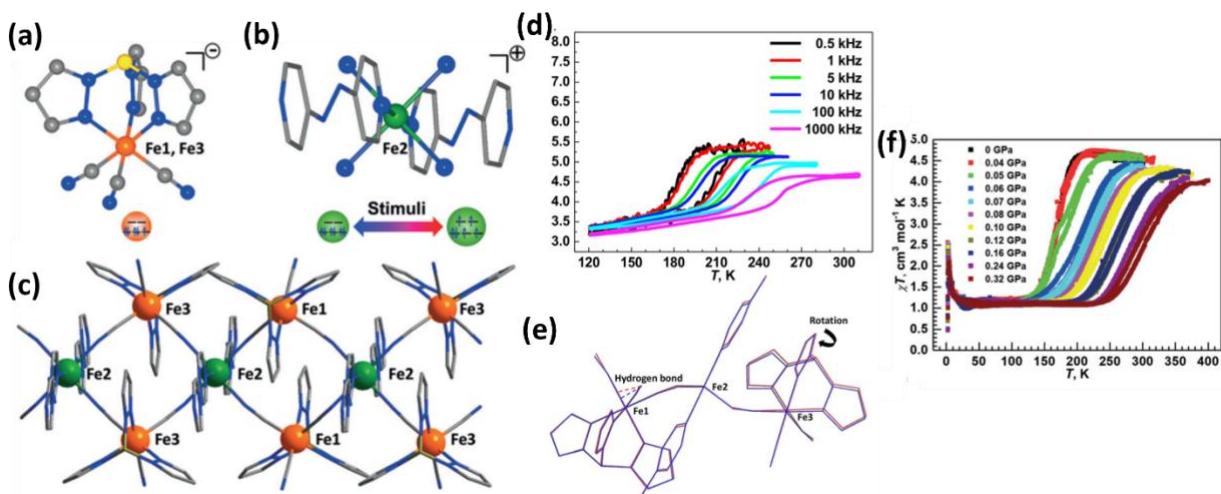


**Fig. 42.** (a) Crystal structure of the anionic  $[(\text{Tp})\text{Fe}^{\text{III}}(\text{CN})_3]^-$  building block. (b) Structure of cationic Fe(II) SCO unit. (c) Double zigzag chain arrangement in **65** along crystallographic a-axis. All hydrogen atoms and water molecules are removed for clarity. Color code: Fe<sup>II</sup>, green; Fe<sup>III</sup>, orange; C, gray; B, gold; N, blue. (d) Real part of dielectric constants versus T plot. (e) Structural variation of the asymmetric  $\text{Fe}^{\text{III}}_2\text{Fe}^{\text{II}}$  unit at 250 K (red) and 10 K (blue). N···O hydrogen bonds between terminal cyanide nitrogen atoms and uncoordinated water is represented by dashed lines. (f) Temperature dependence of magnetic susceptibility under different applied pressures. Adapted with permission from Ref. [112].

A similar observation was found in another 2D SCO framework,  $[\text{Fe}^{\text{II}}(\text{L43})][(\text{pzTp})\text{Fe}^{\text{III}}-(\text{CN})_3]_2$  (**66**) (**L43** = 1,2-bis(4-pyridyl)ethyne and pzTp = tetrakis(pyrazolyl)borate), where the local structural changes are propagated to the whole crystal lattice by rigid bridging ligand **L43** (Fig. 43a). In this case, the anionic  $[(\text{pzTp})\text{Fe}^{\text{III}}-(\text{CN})_3]^-$  units have the polar pyrazolyl units, which can rotate in the crystal lattice, and this rotational movement of the polar group can create a dipolar moment variation for the system in HS and LS state. It was observed that there is a structural deformation of the  $[(\text{pzTp})\text{Fe}^{\text{III}}-(\text{CN})_3]^-$  unit upon spin transition. When the bridging ligand **L43**

was set as a reference then the apical pyrazolyl ring exhibited positional disorders in the two rotational positions.  $63.7^\circ$  is the dihedral angle between the positionally disordered pyrazolyl ring at 110 K in the LS state, while it is  $75.5^\circ$  at 180 K in the HS state (Fig. 43b). Thus, it can be seen in the dielectric measurement profile that it shows a weak hysteretic transition similar to the temperature where a spin transition occurs (Fig. 43c) [54].

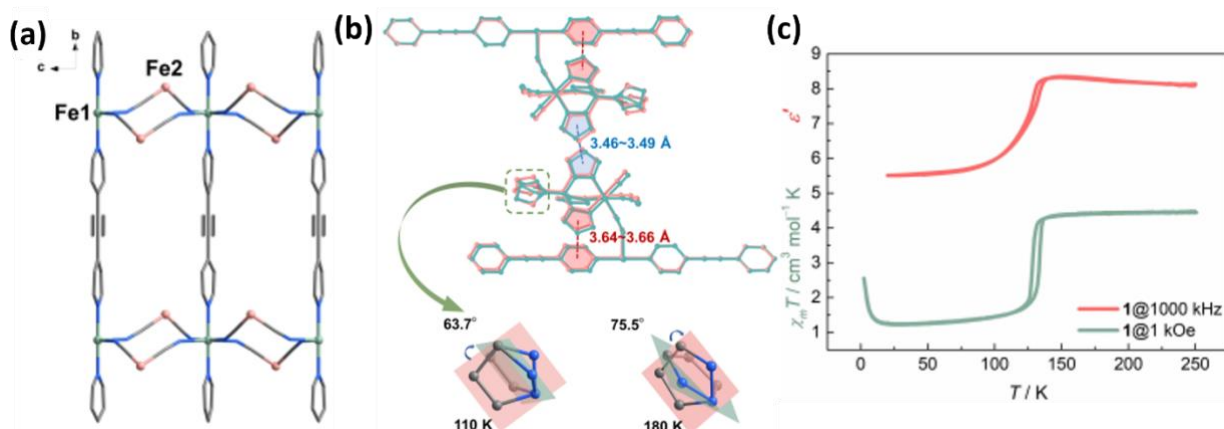


**Fig. 43.** (a) Simplified two-dimensional layer structure of **66** omitting hydrogen atoms, terminal free cyanide, pzTp for clarity. (b) Structural overlap diagram of **66** at 180 K (red) and 110 K (green). The blue and red dotted lines represent interchain and intrachain  $\pi\cdots\pi$  interactions respectively. (c) Variable temperature dielectric constants (red line) at 1000 kHz and  $\chi T$  vs  $T$  plot (green line) under the 10000 Oe dc field for **66**. Adapted with permission from Ref. [54].

In a framework structure of  $\{\text{Fe}(\text{L44})[\text{Pt}(\text{CN})_4]\}\cdot 0.5\text{anth}$  (anth = anthracene) (**67**), thermal and light-induced switching in the magnetic and dielectric properties were observed. The framework structure was constructed with  $[\text{Pt}(\text{CN})_4]^-$  anion and Fe(II) with 2,5-bis-(4-pyridyl)thiophene (**L44**) as bridging ligand (Fig. 44a). The compound exhibits a four-step spin-transition having transitions at 189 K, 178 K, 136 K and 112 K. When the dielectric measurement was performed as a function of temperature, a similar trend was observed with dielectric properties as well, transitions were observed at 201, 165, 132, and 115 K (Fig. 44b). This shows the synergy between the SCO and

dielectric behavior. Then a light-induced dielectric study was performed, and at 10 K there was a sudden drop in the dielectric constant ( $\epsilon'$ ) from 16.37 to 16.02 when irradiated with 505 nm light. Again, when the sample is irradiated with 808 nm light, the dielectric constant increases from 16.02 to 16.58 within 5 minutes and then stays constant upon further irradiation (Fig. 44c). This switching in the dielectric property upon irradiation of various light is reversible and doesn't change with applying different power of lights [60].

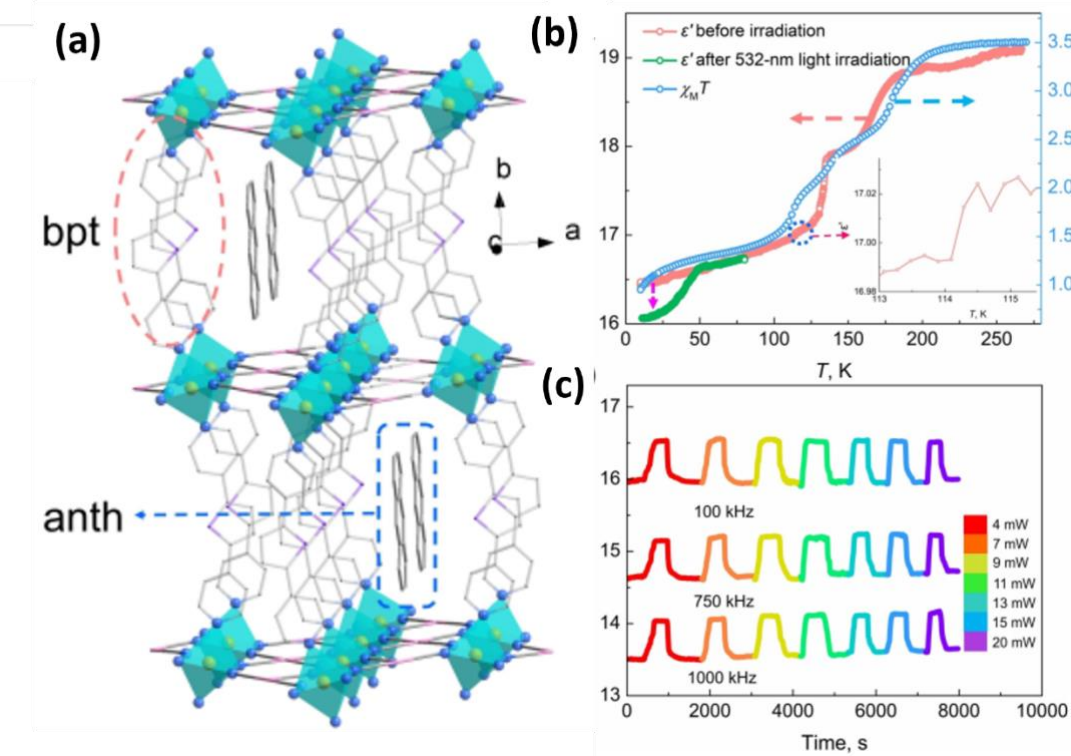


**Fig. 44.** (a) Simplified structure of Hofmann-type framework at 300 K omitting all hydrogen atoms, positionally disordered ligand moieties for clarity. Fe, orange; Pt, rose; S, purple; N, blue; C, grey. (b) Temperature dependent  $\chi T$  plot (blue line) and for **67** (blue line); temperature dependence of dielectric constant  $\epsilon'$  for **67** before (rose line, 100 kHz) and after 532-nm light irradiation (green line, 100 kHz). (c) Time dependence of dielectric constants (100, 750 and 1000 kHz) under different light powers at 10 K. Adapted with permission from Ref. [60].

Another 2D Hofmann type compound  $\{[\text{Fe}(\text{L45})_2][\text{M}(\text{CN}_4)]\}$  was reported by Meng, Liu and co-workers, where they utilized  $[\text{M}(\text{CN}_4)]^{2-}$  building blocks  $\{\text{M} = \text{Pt (68)} \text{ and Pd (69)}\}$  and **L45** = 3,4-bis(4-pyridyl)thiophene along with Fe(II) unit. Here Fe(II) ion sits on an elongated octahedral coordination environment and is coordinated with four pyridyl nitrogen from the **L45** ligand in the equatorial position and two cyanide bridges are attached with Fe(II) from the axial position. It forms a 2D network of extended structure (Fig. 45a) and also exhibits strong cooperativity as it exhibits thermal hysteresis in the magnetic profile. Complexes **68** and **69** reveal a 19 K (Fig. 45b) and 20 K wide thermal hysteresis loop, respectively. Both the complexes showed the LIESST effect when irradiated with 505 nm light and showed the reverse LIESST effect when irradiated with 808 nm light at 10 K. The dielectric measurement also revealed a hysteretic transition having a 20 K wide hysteresis (Fig. 45c) [113]. The hysteretic behavior of both magnetic and dielectric properties shows that there is synergy between these two properties.

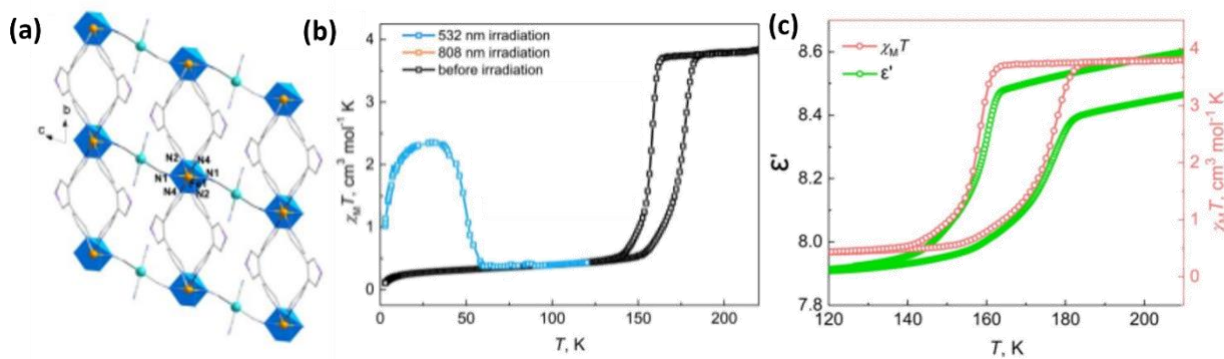


**Fig. 45.** (a) Crystal structure view of **68** along crystallographic a-axis, for clarity hydrogen atoms are omitted. Color code: Fe: light orange; Pt: aqua; S: purple; C: grey; N: blue. (b)  $\chi T$  vs  $T$  plot of **68** before and after irradiation with 532 nm light with an applied dc field of 10000 Oe. (c) Temperature-dependent  $\chi T$  vs.  $T$  plots (rose line); variation of dielectric constant  $\epsilon'$  with temperature for **68** (green line, 100 kHz). Adapted with permission from Ref. [113].

In a Hofmann-type coordination network, luminescent ligand 1,1-diphenyl-2,2-di(4-pyridylbiphenyl)ethylene (**L46**) was used to obtain the  $\{\text{Fe}(\text{L46})_2[\text{Ag}(\text{CN})_2]_2\} \cdot 2\text{EtOH}$  (**70**) (Fig. 46a). Here the Fe(II) metal centre is bound to four cyanide nitrogen atoms coming from four  $[\text{Ag}(\text{CN})_2]$  equatorially and two **L46** ligands are coordinating with the Fe(II) in the axial position. The overall structure is composed of a 2D layer of  $[\text{Fe}_4\{\text{Ag}(\text{CN})_2\}_4]$ , which are further connected via **L46** ligands. Also, due to the head-to-tail stack of **L46** ligands and short contacts among them, they form a three-dimensional (3D) framework. The magnetic profile reveals a gradual SCO with  $T_{1/2} = 231$  K (Fig. 46b). It also showed a decrease in the fluorescence intensity with an increase in the temperature, indicating the coexistence of fluorescence and SCO without having any synergy between them. In the dielectric profile, a change in the dielectric constant is found without any thermal hysteresis loop (Fig. 46c) [114].

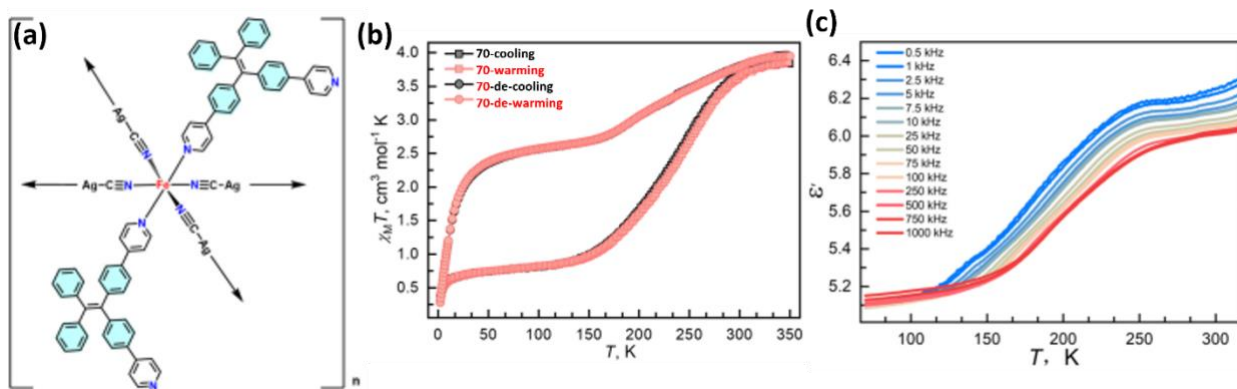


**Fig. 46.** (a) Schematic presentation of self-assembly process of ligand **L46** and complex **70**. (b)  $\chi T$  vs T plot of **70** and **70-de** with applied dc field of 1000 Oe in the cooling and warming modes. (c) Variation of  $\epsilon'$  signals with temperature with different frequencies for the powder-pressed pellet sample of **70**. Adapted with permission from Ref. [114].

### **3. CONCLUSION AND PERSPECTIVE**

Multifunctional materials exhibiting synergistic effects between different physical properties have gained enormous interest in modern research due to their vast potential for device application under practical conditions. The interplay between luminescence and spin crossover is important, as this can help to develop multifunctional materials that interact with light and heat and can be controlled synergically, which allows them to be beneficial for tuning both SCO and Luminescence properties. The usefulness of such systems depends on the extent of synergy between the two properties. The main governing factors are the spectral overlap between the SCO and emission band arising from the luminophore and the conformation and intermolecular interactions between the luminophores. This review presents a concise, up-to-date overview of the multifunctional materials mostly comprising Fe(II) metal center, showing synergistic SCO and luminescence properties covering entire 0D, 1D up to 3D structures with mononuclear to polynuclear systems. However, synergistic SCO and luminescence is even more challenging and thus significantly not explored much. Because even if the quantum efficiency of the luminophores is comparable to that of the acceptors, this synergy depends strongly on the arrangement of the whole molecular network involving intra- and inter-molecular interactions among the metal centers, luminophores and surrounding solvent molecules. Fluorescence emission in these SCO-active complexes can be triggered majorly by two mechanisms: (i) overlap of the fluorophore's emission band and the absorption band of the SCO-active complex, which causes the reabsorption of photons by the HS or LS SCO complexes, and may be the distance between the fluorophore and the SCO center is short resulting that the excited-state energy from fluorophore can be directly transported to the SCO center; (ii) effect of surroundings of the complexes including variations in polarity, vibrational frequency, stiffness can also be used for tuning the fluorescence emission in

these complexes. In general, luminophores are grafted onto the ligand backbone to have effective spectral overlap with the SCO center, or the luminophores can show aggregation-induced emission (AIE), which is useful for practical applications. This approach has been implied to develop advanced systems that can work as luminescence thermometry for detecting SCO in such molecular systems. Also, researchers are now-a-days looking for new bifunctional SCO-fluorescent complexes where the fluorescence emission originates from lanthanide metal centers or transition metal–organic motifs, which is rare and may exhibit unexpected SCO-fluorescence synergy and energy transfer mechanisms. However, such phenomena are unpredictable, and still, more work is needed to rationalize this synergistic behavior to attain effective multifunctional materials that can be used in optoelectronic and magneto-optical devices. In terms of multifunctional molecules, we have also represented examples of various SCO molecules exhibiting dielectric properties. In many cases, it has been found that magnetic switching and dielectric switching happen in similar temperature ranges, which is a prerequisite for fabricating various sensors or molecular devices. In these cases, the change in magnetic state can be gauged via the dielectric response. From literature, it has been found that 1D-3D molecules show much better changes in the dielectric property as compared to discrete 0D molecules, as in the polymeric structure, the changes are more prominent and thus lead to a large change in the relative permittivity of the material. Now, the research is gearing up to design molecules with all three SCO, luminescence, and dielectric properties to provide magnetic optoelectronic materials that can be utilized for various molecular device applications and also there are several aspects which need detailed investigations such as (i) improvement of quantum yield efficiency and life time, (ii) more control of the synergic behavior through molecular control (structure-function properties), (iii) detail mechanistic study to predict the accurate SCO (transition) temperature from PL or dielectric

measurement, while recent results only show a broad range, (iv) use of other transition metals [Co(II), Mn(III), Cr(II) *etc.*] as well as Fe(III) apart from Fe(II) metal center, (v) finally, shifting of SCO temperature to near room temperature along with synergic control which are essential particularly for device applications.

## AUTHOR INFORMATION

### Corresponding Author

\*Email: [subratat@iisc.ac.in](mailto:subratat@iisc.ac.in), [mondal@iisc.ac.in](mailto:mondal@iisc.ac.in)

### ORCID

Bijoy Dey: 0000-0003-4185-4240

Debopam Sarkar: 0000-0003-2149-2019

Sounak Ghosh: 0000-0002-8697-7183

Sakshi Mehta: 0000-0002-1232-4489

Krishna Kaushik: 0000-0002-2272-0311

Subrata Ghosh: 0000-0003-4539-4413

Abhishake Mondal: 0000-0002-5061-2326

### Notes

The authors declare no competing financial interest.

## ACKNOWLEDGEMENT

This research work is supported by the Indian Institute of Science (IISc), Bangalore, India. We are thankful to IISc & Ministry of Education (MoE), Science and Engineering Research Board, Govt. of India, Project ID: CRG/2023/003081, for financial assistance. BD thanks IISc-IoE; DS thanks MoE-PMRF; Sounak Ghosh, SM, KK thank IISc for their fellowships. Subrata Ghosh thanks to the Council of Scientific and Industrial Research (CSIR), Govt. of India.

## REFERENCES

- [1] F. Bigdeli, C.T. Lollar, A. Morsali, H.-C. Zhou, Switching in Metal–Organic Frameworks, *Angew. Chem. Int. Ed.* 59 (2020) 4652-4669.
- [2] K. Yang, W. Paul, S.-H. Phark, P. Willke, Y. Bae, T. Choi, T. Esat, A. Ardavan, A.J. Heinrich, C.P. Lutz, Coherent spin manipulation of individual atoms on a surface, *Science* 366 (2019) 509-512.
- [3] Y.-S. Meng, T. Liu, Manipulating Spin Transition To Achieve Switchable Multifunctions, *Acc. Chem. Res.* 52 (2019) 1369-1379.
- [4] K. Hymas, A. Soncini, Molecular spintronics using single-molecule magnets under irradiation, *Phys. Rev. B* 99 (2019) 245404.
- [5] A. Gaita-Ariño, F. Luis, S. Hill, E. Coronado, Molecular spins for quantum computation, *Nat. Chem.* 11 (2019) 301-309.
- [6] S. Hayami, S.M. Holmes, M.A. Halcrow, Spin-state switches in molecular materials chemistry, *J. Mater. Chem. C* 3 (2015) 7775-7778.
- [7] G. Aromí, D. Aguilà, P. Gamez, F. Luis, O. Roubeau, Design of magnetic coordination complexes for quantum computing, *Chem. Soc. Rev.* 41 (2012) 537-546.
- [8] T. Kitazawa, Synthesis and Applications of New Spin Crossover Compounds, *Crystals* 9 (2019) 382-385.
- [9] M. A. Halcrow, Spin-Crossover Materials, J. Wiley and Sons. (2013) 147-169.
- [10] P. Gütlich, A. Hauser, H. Spiering, Thermal and Optical Switching of Iron(II) Complexes, *Angew. Chem. Int. Ed.* 33 (1994) 2024-2054.
- [11] F. Houard, Q. Evrard, G. Calvez, Y. Suffren, C. Daiguebonne, O. Guillou, F. Gendron, B. Le Guennic, T. Guizouarn, V. Dorcet, M. Mannini, K. Bernot, Chiral Supramolecular Nanotubes of Single-Chain Magnets, *Angew. Chem. Int. Ed.* 59 (2020) 780-784.
- [12] C. Coulon, H. Miyasaka, R. Clérac, Single-Molecule Magnets and Related Phenomena, Springer Berlin Heidelberg (2006) 163-206.
- [13] P. Lutz, D. Aguilà, A. Mondal, D. Pinkowicz, R. Marx, P. Neugebauer, B. Fåk, J. Ollivier, R. Clérac, J. van Slageren, Elementary excitations in single-chain magnets, *Phys. Rev. B* 96 (2017) 094415.
- [14] J. Wang, Q.-W. Li, S.-G. Wu, Y.-C. Chen, R.-C. Wan, G.-Z. Huang, Y. Liu, J.-L. Liu, D. Reta, M.J. Giansiracusa, Z.-X. Wang, N.F. Chilton, M.-L. Tong, Opening Magnetic Hysteresis by Axial Ferromagnetic Coupling: From Mono-Decker to Double-Decker Metallacrown, *Angew. Chem. Int. Ed.* 60 (2021) 5299-5306.
- [15] C. Rajnák, R. Boča, Reciprocating thermal behavior in the family of single ion magnets, *Coord. Chem. Rev.* 436 (2021) 213808.

- [16] R. Boča, C. Rajnák, Unexpected behavior of single ion magnets, *Coord. Chem. Rev.* 430 (2021) 213657.
- [17] C.A.P. Goodwin, F. Ortú, D. Reta, N.F. Chilton, D.P. Mills, Molecular magnetic hysteresis at 60 kelvin in dysprosocenium, *Nature* 548 (2017) 439-442.
- [18] R. Sessoli, H.L. Tsai, A.R. Schake, S. Wang, J.B. Vincent, K. Folting, D. Gatteschi, G. Christou, D.N. Hendrickson, High-spin molecules:  $[\text{Mn}_{12}\text{O}_{12}(\text{O}_2\text{CR})_{16}(\text{H}_2\text{O})_4]$ , *J. Am. Chem. Soc.* 115 (1993) 1804-1816.
- [19] R. Sessoli, D. Gatteschi, A. Caneschi, M.A. Novak, Magnetic bistability in a metal-ion cluster, *Nature* 365 (1993) 141-143.
- [20] A. Mondal, Y. Li, M. Seuleiman, M. Julve, L. Toupet, M. Buron-Le Cointe, R. Lescouëzec, On/Off Photoswitching in a Cyanide-Bridged  $\{\text{Fe}_2\text{Co}_2\}$  Magnetic Molecular Square, *J. Am. Chem. Soc.* 135 (2013) 1653-1656.
- [21] S. Kamilya, S. Ghosh, S. Mehta, A. Mondal, Effect of Ligand Modulation on Metal-to-Metal Electron Transfer in a Series of  $[\text{Fe}_2\text{Co}_2]$  Molecular Square Complexes, *J. Phys. Chem. A* 125 (2021) 4775-4783.
- [22] S. Kamilya, S. Ghosh, Y. Li, P. Dechambenoit, M. Rouzières, R. Lescouëzec, S. Mehta, A. Mondal, Two-Step Thermoinduced Metal-to-Metal Electron Transfer and ON/OFF Photoswitching in a Molecular  $[\text{Fe}_2\text{Co}_2]$  Square Complex, *Inorg. Chem.* 59 (2020) 11879-11888.
- [23] P. Gütlich, A.B. Gaspar, Y. Garcia, Spin state switching in iron coordination compounds, *Beilstein J. Org. Chem.* 9 (2013) 342-391.
- [24] C. Brady, J.J. McGarvey, J.K. McCusker, H. Toftlund, D.N. Hendrickson, Spin Crossover in Transition Metal Compounds III, Springer Berlin Heidelberg (2004) 1-22.
- [25] S. Ghosh, S. Ghosh, S. Kamilya, S. Mandal, S. Mehta, A. Mondal, Impact of Counteranion on Reversible Spin-State Switching in a Series of Cobalt(II) Complexes Containing a Redox-Active Ethylenedioxythiophene-Based Terpyridine Ligand, *Inorg. Chem.* 61 (2022) 17080-17088.
- [26] B. Dey, V. Chandrasekhar,  $\text{Fe}^{\text{II}}$  spin crossover complexes containing  $\text{N}_4\text{O}_2$  donor ligands *Dalton Trans.* 51 (2022) 13995-14021.
- [27] B. Dey, J. Cirera, S. Mehta, L.P. Ferreira, R. Arumugam, A. Mondal, P.N. Martinho, V. Chandrasekhar, Steric Effects on Spin States in a Series of Fe(III) Complexes *Cryst. Growth Des.* 23 (2023) 6668-6678.
- [28] K. Kaushik, S. Mehta, M. Das, S. Ghosh, S. Kamilya, A. Mondal, Stimuli-responsive magnetic materials: impact of spin and electronic modulation, *Chem. Commun.* 59 (2023) 13107-13124.
- [29] H. S. Scott, R.W. Staniland, P.E. Kruger, Spin crossover in homoleptic Fe(II) imidazolylimine complexes, *Coord. Chem. Rev.* 362 (2018) 24-43.

- [30] R. W. Hogue, S. Singh, S. Brooker, Spin crossover in discrete polynuclear iron(ii) complexes, *Chem. Soc. Rev.* 47 (2018) 7303-7338.
- [31] H.L.C. Feltham, A.S. Barltrop, S. Brooker, Spin crossover in iron(II) complexes of 3,4,5-tri-substituted-1,2,4-triazole (Rdpt), 3,5-di-substituted-1,2,4-triazolate (dpt<sup>-</sup>), and related ligands, *Coord. Chem. Rev.* 344 (2017) 26-53.
- [32] L.J. Kershaw Cook, R. Mohammed, G. Sherborne, T.D. Roberts, S. Alvarez, M.A. Halcrow, Spin state behavior of iron(II)/dipyrazolylpyridine complexes. New insights from crystallographic and solution measurements, *Coord. Chem. Rev.* 289-290 (2015) 2-12.
- [33] G.A. Craig, O. Roubeau, G. Aromí, Spin state switching in 2,6-bis(pyrazol-3-yl)pyridine (3-bpp) based Fe(II) complexes, *Coord. Chem. Rev.* 269 (2014) 13-31.
- [34] J. Olguín, Unusual metal centres/coordination spheres in spin crossover compounds, *Coord. Chem. Rev.* 407 (2020) 213148.
- [35] O. Drath, C. Boskovic, Switchable cobalt coordination polymers: Spin crossover and valence tautomerism, *Coord. Chem. Rev.* 375 (2018) 256-266.
- [36] R.G. Miller, S. Narayanaswamy, J.L. Tallon, S. Brooker, Spin crossover with thermal hysteresis in cobalt(ii) complexes and the importance of scan rate, *New J Chem.* 38 (2014) 1932-1941.
- [37] S. Hayami, Y. Komatsu, T. Shimizu, H. Kamihata, Y.H. Lee, Spin-crossover in cobalt(II) compounds containing terpyridine and its derivatives, *Coord. Chem. Rev.* 255 (2011) 1981-1990.
- [38] I. Krivokapic, M. Zerara, M.L. Daku, A. Vargas, C. Enachescu, C. Ambrus, P. Tregenna-Piggott, N. Amstutz, E. Krausz, A. Hauser, Spin-crossover in cobalt(II) imine complexes, *Coord. Chem. Rev.* 251 (2007) 364-378.
- [39] S. Ghosh, S. Selvamani, S. Mehta, A. Mondal, Reversible thermo-induced spin crossover in a mononuclear *cis*-dicyanamido-cobalt(ii) complex containing a macrocyclic tetradentate ligand, *Dalton Trans.* 49 (2020) 9208-9212.
- [40] S. Ghosh, S. Selvamani, S. Kamilya, S. Mehta, A. Mondal, Tuning of spin crossover properties in a series of mononuclear cobalt(ii) complexes based on a macrocyclic tetradentate ligand and pseudohalide coligands, *Dalton Trans.* 51 (2022) 9642-9652.
- [41] S. Ghosh, S. Kamilya, M. Rouzières, R. Herchel, S. Mehta, A. Mondal, Reversible Spin-State Switching and Tuning of Nuclearity and Dimensionality via Nonlinear Pseudohalides in Cobalt(II) Complexes, *Inorg. Chem.* 59 (2020) 17638-17649.
- [42] S. Ghosh, S. Bagchi, S. Kamilya, A. Mondal, Effect of ligand substituents and tuning the spin-state switching in manganese(iii) complexes, *Dalton Trans.* 50 (2021) 4634-4642.
- [43] S. Ghosh, S. Bagchi, M. Das, S. Kamilya, A. Mondal, Stepwise spin-state switching in a manganese(iii) complex, *Dalton Trans.* 49 (2020) 14776-14780.

- [44] S. Kamilya, B. Dey, K. Kaushik, S. Shukla, S. Mehta, A. Mondal, Realm of Spin State Switching Materials: Toward Realization of Molecular and Nanoscale Devices, *Chem. Mater.* 36 (2024) 4889-4915.
- [45] K. S. Kumar, M. Ruben, Sublimable Spin-Crossover Complexes: From Spin-State Switching to Molecular Devices, *Angew. Chem. Int. Ed.* 60 (2021) 7502-7521.
- [46] K. Kaushik, S. Ghosh, S. Kamilya, M. Rouzières, S. Mehta, A. Mondal, Reversible Photo- and Thermo-Induced Spin-State Switching in a Heterometallic {5d-3d} W<sub>2</sub>Fe<sub>2</sub> Molecular Square Complex, *Inorg. Chem.* 60 (2021) 7545-7552.
- [47] J. F. Létard, Photomagnetism of iron(ii) spin crossover complexes—the T(LIESST) approach, *J. Mater. Chem.* 16 (2006) 2550-2559.
- [48] M. Nakaya, R. Ohtani, L.F. Lindoy, S. Hayami, Light-induced excited spin state trapping in iron(iii) complexes, *Inorg. Chem. Front.* 8 (2021) 484-498.
- [49] K. Senthil Kumar, M. Ruben, Emerging trends in spin crossover (SCO) based functional materials and devices, *Coord. Chem. Rev.* 346 (2017) 176-205.
- [50] E. Coronado, Molecular magnetism: from chemical design to spin control in molecules, materials and devices, *Nat. Rev. Mat.* 5 (2020) 87-104.
- [51] O. I. Kucheriv, V.V. Oliynyk, V.V. Zagorodnii, V.L. Launets, I.y.A. Gural'skiy, Spin-Crossover Materials towards Microwave Radiation Switches, *Sci. Rep.* 6 (2016) 38334.
- [52] A. Bousseksou, G. Molnár, P. Demont, J. Menegotto, Observation of a thermal hysteresis loop in the dielectric constant of spin crossover complexes: towards molecular memory devices, *J. Mater. Chem.* 13 (2003) 2069-2071.
- [53] H.J. Shepherd, C.M. Quintero, G. Molnár, L. Salmon, A. Bousseksou, Luminescent Spin-Crossover Materials, in: *Spin-Crossover Materials*, 2013, pp. 347-373.
- [54] W. Wen, Q. Liu, S.-H. Zhang, N.-T. Yao, H. Oshio, Y.-S. Meng, T. Liu, Spin-Crossover Tuned Rotation of Pyrazolyl Rings in a 2D Iron(II) Complex towards Synergetic Magnetic and Dielectric Transitions, *Angew. Chem. Int. Ed.* 61 (2022) e202208886.
- [55] R. Aswathy, K. Mohanan, Microwave Assisted Synthesis, Characterisation and Fluorescence Studies of some Transition Metal Complexes with a Luminol Derivative, *J. Fluoresc.* 27 (2017) 1171-1181.
- [56] O. A. Qamar, F. Jamil, M. Hussain, M. Mustafa, R.U. Rehman, A. Inayat, M.S. Habib, M. Sajid, A review on Fe-based spin crossover complexes with synergetic conductive and fluorescent properties, *Chem. Pap.* 77 (2023) 7331-7359.
- [57] Z.-Y. Li, J.-W. Dai, K.J. Gagnon, H.-L. Cai, T. Yamamoto, Y. Einaga, H.-H. Zhao, S. Kanegawa, O. Sato, K.R. Dunbar, R.-G. Xiong, A neutral Fe(III) compound exhibiting a two-step spin transition and dielectric anomalies, *Dalton Trans.* 42 (2013) 14685-14688.

- [58] J. Ru, F. Yu, P.-P. Shi, C.-Q. Jiao, C.-H. Li, R.-G. Xiong, T. Liu, M. Kurmoo, J.-L. Zuo, Three Properties in One Coordination Complex: Chirality, Spin Crossover, and Dielectric Switching, *Eur. J. Inorg. Chem.* 2017 (2017) 3144-3149.
- [59] M. Nakano, G.-e. Matsubayashi, T. Matsuo, Dielectric behavior of manganese(III) spin-crossover complex [Mn(taa)], *Phys. Rev. B*, 66 (2002) 212412.
- [60] N.-T. Yao, L. Zhao, H.-Y. Sun, C. Yi, Y.-H. Guan, Y.-M. Li, H. Oshio, Y.-S. Meng, T. Liu, Simultaneous Photo-Induced Magnetic and Dielectric Switching in an Iron(II)-Based Spin-Crossover Hofmann-Type Metal-Organic Framework, *Angew. Chem. Int. Ed.* 61 (2022) e202208208.
- [61] Y. Jiao, J. Zhu, Y. Guo, W. He, Z. Guo, Synergetic effect between spin crossover and luminescence in the  $[\text{Fe}(\text{bpp})_2][\text{BF}_4]_2$  ( $\text{bpp} = 2,6\text{-bis(pyrazol-1-yl)pyridine}$ ) complex, *J. Mater. Chem. C*, 5 (2017) 5214-5222.
- [62] J. M. Holland, J. A. McAllister, Z. Lu, C. A. Kilner, M. Thornton-Pett, M. A. Halcrow, An unusual abrupt thermal spin-state transition in  $[\text{FeL}_2][\text{BF}_4]_2$  [ $\text{L} = 2,6\text{-di(pyrazol-1-yl)pyridine}$ ], *Chem. Commun.* (2001) 577-578.
- [63] J.-L. Wang, Q. Liu, Y.-S. Meng, X. Liu, H. Zheng, Q. Shi, C.-Y. Duan, T. Liu, Fluorescence modulation via photoinduced spin crossover switched energy transfer from fluorophores to  $\text{Fe}^{\text{II}}$  ions, *Chem. Sci.* 9 (2018) 2892-2897.
- [64] J. Yuan, S.-Q. Wu, M.-J. Liu, O. Sato, H.-Z. Kou, Rhodamine 6G-Labeled Pyridyl Aroylhydrazone Fe(II) Complex Exhibiting Synergetic Spin Crossover and Fluorescence, *J. Am. Chem. Soc.* 140 (2018) 9426-9433.
- [65] B. Benaicha, K. Van Do, A. Yangui, N. Pittala, A. Lusson, M. Sy, G. Bouchez, H. Fourati, C. J. Gómez-García, S. Triki, K. Boukhedadden, Interplay between spin-crossover and luminescence in a multifunctional single crystal iron(ii) complex: towards a new generation of molecular sensors, *Chem. Sci.* 10 (2019) 6791-6798.
- [66] B.-X. Luo, Y. Pan, Y.-S. Meng, Q. Liu, J. Yin, T. Liu, Y.-Y. Zhu, Construction of Magneto-Fluorescent Bifunctional Spin-Crossover Fe(II) Complex from Pyrene-Decorated Pybox Ligand, *Eur. J. Inorg. Chem.* 2021 (2021) 3992-3999.
- [67] C. Yi, Y.-S. Meng, L. Zhao, N.-T. Yao, Q. Liu, W. Wen, R.-X. Li, Y.-Y. Zhu, H. Oshio, T. Liu, A Smart Molecule Showing Spin Crossover Responsive Aggregation-Induced Emission, *CCS Chem.* 5 (2023) 915-924.
- [68] Y. Li, M.K. Javed, S.-Q. Wu, A. Sulaiman, Y.-Y. Wu, Z.-Y. Li, O. Sato, X.-H. Bu, Aggregation-induced emission meets magnetic bistability: Synergy between spin crossover and fluorescence in iron(II) complexes, *Chin. Chem. Lett.* 34 (2023) 107492.
- [69] C. Yi, S.-H. Zhang, L. Zhao, N.-T. Yao, G.-H. Zhao, Y.-S. Meng, T. Liu, Constructing spin crossover-fluorescence bifunctional iron(ii) complexes based on tetraphenyl ethylene-decorated AI<sup>E</sup>gens, *Dalton Trans.* 52 (2023) 5169-5175.

- [70] G.-H. Zhao, S.-H. Zhang, C. Yi, T. Liu, Y.-S. Meng, Construction of spin crossover-fluorescence bifunctional iron(ii) complexes with modified bis(pyrazole)pyridine ligands, *New J. Chem.* 47 (2023) 10967-10972.
- [71] R. Rabelo, L. Toma, N. Moliner, M. Julve, F. Lloret, M. Inclán, E. García-España, J. Pasán, R. Ruiz-García, J. Cano, pH-Switching of the luminescent, redox, and magnetic properties in a spin crossover cobalt(ii) molecular nanomagnet, *Chem. Sci.* 14 (2023) 8850-8859.
- [72] S. Sundaresan, J.-G. Becker, J. Eppelsheimer, A.E. Sedykh, L.M. Carrella, K. Müller-Buschbaum, E. Rentschler, Synergetic spin singlet–quintet switching and luminescence in mononuclear Fe(ii) 1,3,4-oxadiazole tetradeятate chelates with NCBH<sub>3</sub> co-ligand *Dalton Trans.* 52 (2023) 13181-13189.
- [73] J. Feng, X. Wang, L. Wang, J. Kfouri, J. Oláh, S. Zhang, L. Zou, Y. Guo, S. Xue, Naphthalimide-Tagged Iron(II) Spin Crossover Complex with Synergy of Ratiometric Fluorescence for Thermosensing *Inorg. Chem.* 63 (2024) 108-116.
- [74] Y. Garcia, F. Robert, A.D. Naik, G. Zhou, B. Tinant, K. Robeyns, S. Michotte, L. Piraux, Spin Transition Charted in a Fluorophore-Tagged Thermochromic Dinuclear Iron(II) Complex *J. Am. Chem. Soc.* 133 (2011) 15850-15853.
- [75] C.-F. Wang, M.-J. Sun, Q.-J. Guo, Z.-X. Cao, L.-S. Zheng, J. Tao, Multiple correlations between spin crossover and fluorescence in a dinuclear compound, *Chem. Commun.* 52 (2016) 14322-14325.
- [76] M. Estrader, J. Salinas Uber, L.A. Barrios, J. Garcia, P. Lloyd-Williams, O. Roubeau, S.J. Teat, G. Aromí, A Magneto-optical Molecular Device: Interplay of Spin Crossover, Luminescence, Photomagnetism, and Photochromism, *Angew. Chem. Int. Ed.* 56 (2017) 15622-15627.
- [77] T. Lathion, A. Fürstenberg, C. Besnard, A. Hauser, A. Bousseksou, C. Piguet, Monitoring Fe(II) Spin-State Equilibria via Eu(III) Luminescence in Molecular Complexes: Dream or Reality? *Inorg. Chem.* 59 (2020) 1091-1103.
- [78] N. Deorukhkar, C. Egger, L. Guénée, C. Besnard, C. Piguet, Detecting Fe(II) Spin-Crossover by Modulation of Appended Eu(III) Luminescence in a Single Molecule, *J. Am. Chem. Soc.* 146 (2024) 308-318.
- [79] B. Schäfer, T. Bauer, I. Faus, J.A. Wolny, F. Dahms, O. Fuhr, S. Lebedkin, H.-C. Wille, K. Schlage, K. Chevalier, F. Rupp, R. Diller, V. Schünemann, M.M. Kappes, M. Ruben, A luminescent Pt<sub>2</sub>Fe spin crossover complex, *Dalton Trans.* 46 (2017) 2289-2302.
- [80] C. Lochenie, K. Schötz, F. Panzer, H. Kurz, B. Maier, F. Puchtler, S. Agarwal, A. Köhler, B. Weber, Spin-Crossover Iron(II) Coordination Polymer with Fluorescent Properties: Correlation between Emission Properties and Spin State, *J. Am. Chem. Soc.* 140 (2018) 700-709.
- [81] J.-Y. Ge, Z. Chen, L. Zhang, X. Liang, J. Su, M. Kurmoo, J.-L. Zuo, A Two-Dimensional Iron(II) Coordination Polymer with Synergetic Spin-Crossover and Luminescent Properties, *Angew. Chem. Int. Ed.* 58 (2019) 8789-8793.

- [82] S. Ghosh, S. Kamilya, T. Pramanik, M. Rouzières, R. Herchel, S. Mehta, A. Mondal, ON/OFF Photoswitching and Thermoinduced Spin Crossover with Cooperative Luminescence in a 2D Iron(II) Coordination Polymer, *Inorg. Chem.* 59 (2020) 13009-13013.
- [83] S. Ghosh, S. Kamilya, T. Pramanik, A. Mohanty, M. Rouzières, R. Herchel, S. Mehta, A. Mondal, Thermo- and photoinduced spin state switching in an iron(ii) 2D coordination network associated with large light-induced thermal hysteresis and tuning of dimensionality via ligand modulation, *Dalton Trans.* 50 (2021) 7725-7735.
- [84] Y.-R. Qiu, L. Cui, J.-Y. Ge, M. Kurmoo, G. Ma, J. Su, Iron(II) Spin Crossover Coordination Polymers Derived From a Redox Active Equatorial Tetrathiafulvalene Schiff-Base Ligand, *Front. Chem.* 9 (2021).
- [85] C.-F. Wang, J.C. Wu, Q. Li, Synchronously tuning the spin-crossover and fluorescence properties of a two-dimensional Fe(ii) coordination polymer by solvent guests, *Inorg. Chem. Front.* 9 (2022) 3251-3258.
- [86] J. Wang, M. Kong, X.-J. Song, Y. Jing, Y. Zhao, Y. Song, Synergetic Spin-Crossover and Luminescent Properties in a Multifunctional 2D Iron(II) Coordination Polymer, *Inorg. Chem.* 61 (2022) 20923-20930.
- [87] T. Delgado, M. Meneses-Sánchez, L. Piñeiro-López, C. Bartual-Murgui, M.C. Muñoz, J.A. Real, Thermo- and photo-modulation of exciplex fluorescence in a 3D spin crossover Hofmann-type coordination polymer, *Chem. Sci.* 9 (2018) 8446-8452.
- [88] M. Meneses-Sánchez, L. Piñeiro-López, T. Delgado, C. Bartual-Murgui, M.C. Muñoz, P. Chakraborty, J.A. Real, Extrinsic vs. intrinsic luminescence and their interplay with spin crossover in 3D Hofmann-type coordination polymers, *J. Mater. Chem. C* 8 (2020) 1623-1633.
- [89] X.-R. Wu, Z.-K. Liu, M. Zeng, M.-X. Chen, J. Tao, S.-Q. Wu, H.-Z. Kou, Fluorescence emission modulation in cyanido-bridged Fe(II) spin crossover coordination polymers, *Sci. China Chem.* 65 (2022) 1569-1576.
- [90] F.-F. Yan, W.-J. Jiang, N.-T. Yao, P.-D. Mao, L. Zhao, H.-Y. Sun, Y.-S. Meng, T. Liu, Manipulating fluorescence by photo-switched spin-state conversions in an iron(ii)-based SCO-MOF, *Chem. Sci.* 14 (2023) 6936-6942.
- [91] M. Engeser, L. Fabbrizzi, M. Licchelli, D. Sacchi, A fluorescent molecular thermometer based on the nickel(II) high-spin/low-spin interconversion, *Chem. Commun.* (1999) 1191-1192.
- [92] M. Matsuda, H. Tajima, Thin Film of a Spin Crossover Complex  $[\text{Fe}(\text{dpp})_2](\text{BF}_4)_2$ , *Chem. Lett.* 36 (2007) 700-701.
- [93] M. Matsuda, H. Isozaki, H. Tajima, Electroluminescence Quenching Caused by a Spin-crossover, *Transit. Chem. Lett.* 37 (2008) 374-375.
- [94] M. Matsuda, H. Isozaki, H. Tajima, Reproducible on-off switching of the light emission from the electroluminescent device containing a spin crossover complex, *Thin Solid Films* 517 (2008) 1465-1467.

- [95] L. Salmon, G. Molnár, D. Zitouni, C. Quintero, C. Bergaud, J.-C. Micheau, A. Bousseksou, A novel approach for fluorescent thermometry and thermal imaging purposes using spin crossover nanoparticles, *J. Mater. Chem.* 20 (2010) 5499-5503.
- [96] S. Titos-Padilla, J.M. Herrera, X.-W. Chen, J.J. Delgado, E. Colacio, Bifunctional Hybrid SiO<sub>2</sub> Nanoparticles Showing Synergy between Core Spin Crossover and Shell Luminescence Properties, *Angew. Chem. Int. Ed.* 50 (2011) 3290-3293.
- [97] C. M. Quintero, I.y.A. Gural'skiy, L. Salmon, G. Molnár, C. Bergaud, A. Bousseksou, Soft lithographic patterning of spin crossover complexes. Part 1: fluorescent detection of the spin transition in single nano-objects, *J. Mater. Chem.* 22 (2012) 3745-3751.
- [98] J. M. Herrera, S. Titos-Padilla, S.J.A. Pope, I. Berlanga, F. Zamora, J.J. Delgado, K.V. Kamenev, X. Wang, A. Prescimone, E.K. Brechin, E. Colacio, Studies on bifunctional Fe(ii)-triazole spin crossover nanoparticles: time-dependent luminescence, surface grafting and the effect of a silica shell and hydrostatic pressure on the magnetic properties, *J. Mater. Chem. C* 3 (2015) 7819-7829.
- [99] I. Suleimanov, O. Kraieva, J. Sánchez Costa, I.O. Fritsky, G. Molnár, L. Salmon, A. Bousseksou, Electronic communication between fluorescent pyrene excimers and spin crossover complexes in nanocomposite particles, *J. Mater. Chem. C* 3 (2015) 5026-5032.
- [100] I. Suleimanov, O. Kraieva, G. Molnár, L. Salmon, A. Bousseksou, Enhanced luminescence stability with a Tb–spin crossover nanocomposite for spin state monitoring, *Chem. Commun.* 51 (2015) 15098-15101.
- [101] O. Kraieva, I. Suleimanov, G. Molnár, L. Salmon, A. Bousseksou, in: *Magnetochemistry*, 2016.
- [102] I. Suleimanov, G. Molnár, L. Salmon, A. Bousseksou, Near-Infrared Luminescence Switching in a Spin-Crossover Polymer Nanocomposite, *Eur. J. Inorg. Chem.* 2017 (2017) 3446-3451.
- [103] A.-C. Bas, X. Thompson, L. Salmon, C. Thibault, G. Molnár, O. Palamarcicu, L. Routaboul, A. Bousseksou, in: *Magnetochemistry*, 2019.
- [104] I.F. Díaz-Ortega, E.L. Fernández-Barbosa, S. Titos-Padilla, S.J.A. Pope, J.-R. Jiménez, E. Colacio, J.M. Herrera, Monitoring spin-crossover phenomena via Re(i) luminescence in hybrid Fe(ii) silica coated nanoparticles, *Dalton Trans.* 50 (2021) 16176-16184.
- [105] Y. Li, M.K. Javed, S.-Q. Wu, A. Sulaiman, Y.-Y. Wu, Z.-Y. Li, O. Sato, X.-H. Bu, Aggregation-induced emission meets magnetic bistability: Synergy between spin crossover and fluorescence in iron(II) complexes, *Chinese Chem. Lett.* 34 (2023) 107492.
- [106] S. Bonhommeau, T. Guillon, L.M. Lawson Daku, P. Demont, J. Sanchez Costa, J.-F. Létard, G. Molnár, A. Bousseksou, Photoswitching of the Dielectric Constant of the Spin-Crossover Complex [Fe(L)(CN)<sub>2</sub>]·H<sub>2</sub>O, *Angew. Chem. Int. Ed.* 45 (2006) 1625-1629.

- [107] T. Guillon, S. Bonhommeau, J.S. Costa, A. Zwick, J.-F. Létard, P. Demont, G. Molnár, A. Bousseksou, On the dielectric properties of the spin crossover complex  $[\text{Fe}(\text{bpp})_2][\text{BF}_4]_2$ , pss (a) 203 (2006) 2974-2980.
- [108] C. Lefter, I.y.A. Gural'skiy, H. Peng, G. Molnár, L. Salmon, A. Rotaru, A. Bousseksou, P. Demont, Dielectric and charge transport properties of the spin crossover complex  $[\text{Fe}(\text{Htz})_2(\text{trz})](\text{BF}_4)$ , pss RRL 8 (2014) 191-193.
- [109] J.-L. Wang, Q. Liu, Y.-S. Meng, H. Zheng, H.-L. Zhu, Q. Shi, T. Liu, Synergic on/off Photoswitching Spin State and Magnetic Coupling between Spin Crossover Centers, Inorg. Chem. 56 (2017) 10674-10680.
- [110] C. Train, T. Nuida, R. Gheorghe, M. Gruselle, S.-i. Ohkoshi, Large Magnetization-Induced Second Harmonic Generation in an Enantiopure Chiral Magnet, J. Am. Chem. Soc. 131 (2009) 16838-16843.
- [111] Y.-R. Qiu, L. Cui, P.-Y. Cai, F. Yu, M. Kurmoo, C.F. Leong, D.M. D'Alessandro, J.-L. Zuo, Enhanced dielectricity coupled to spin-crossover in a one-dimensional polymer iron(ii) incorporating tetrathiafulvalene, Chem. Sci. 11 (2020) 6229-6235.
- [112] H. Zheng, Y.-S. Meng, G.-L. Zhou, C.-Y. Duan, O. Sato, S. Hayami, Y. Luo, T. Liu, Simultaneous Modulation of Magnetic and Dielectric Transition via Spin-Crossover-Tuned Spin Arrangement and Charge Distribution, Angew. Chem. Int. Ed. 57 (2018) 8468-8472.
- [113] N.-T. Yao, M.-J. Shang, H.-H. Lu, Q. Liu, W. Wen, S.-H. Zhang, L. Zhao, H. Oshio, Y.-S. Meng, T. Liu, Hysteretic magnetism–dielectricity switching in 2D Hofmann type spin-crossover compounds, Inorg. Chem. Front. (2024).
- [114] F.-F. Yan, D. Liu, R. Cai, L. Zhao, P.-D. Mao, H.-Y. Sun, Y.-S. Meng, T. Liu, Simultaneous magneto-dielectric transitions in a fluorescent Hofmann-type coordination polymer, Dalton Trans. 52 (2023) 18206-18213.